Multispectral Time Series Analyses with Landsat and Sentinel-2 to Assess Permafrost Disturbances in North Siberia

---

Alexandra Runge

Univ.-Diss.

zur Erlangung des akademischen Grades
"doctor rerum naturalium"
(Dr. rer. nat.)
in der Wissenschaftsdisziplin "Fernerkundung"

eingereicht in Form einer kumulativen Arbeit an der
Mathematisch-Naturwissenschaftlichen Fakultät
Institut für Geowissenschaften
der Universität Potsdam
und
angefertigt am
Alfred Wegener Institut Helmholtz-Zentrum
für Polar- und Meeresforschung

Potsdam, März 2021

Multispectral Time Series Analyses with Landsat and Sentinel-2 to Assess Permafrost Disturbances in North Siberia

---

Alexandra Runge

Univ.-Diss.

zur Erlangung des akademischen Grades
"doctor rerum naturalium"
(Dr. rer. nat.)
in der Wissenschaftsdisziplin "Fernerkundung"

eingereicht in Form einer kumulativen Arbeit an der
Mathematisch-Naturwissenschaftlichen Fakultät
Institut für Geowissenschaften
der Universität Potsdam

angefertigt am
Alfred Wegener Institut Helmholtz-Zentrum
für Polar- und Meeresforschung

Ort und Tag der Disputation: Potsdam, 16.08.2021

Hauptbetreuer*in: Prof. Guido Grosse
Betreuer*innen: Prof. Ulrike Herzschuh, Dr. Birgit Heim
Gutachter*innen: Prof. Patrick Hostert, Dr. Annett Bartsch

Published online on the
Publication Server of the University of Potsdam:
https://doi.org/10.25932/publishup-52206
https://nbn-resolving.org/urn:nbn:de:kobv:517-opus4-522062

Abstract

Permafrost is warming globally, which leads to widespread permafrost thaw and impacts the surrounding landscapes, ecosystems and infrastructure. Especially ice-rich permafrost is vulnerable to rapid and abrupt thaw, resulting from the melting of excess ground ice. Local remote sensing studies have detected increasing rates of abrupt permafrost disturbances, such as thermokarst lake change and drainage, coastal erosion and RTS in the last two decades. All of which indicate an acceleration of permafrost degradation.

In particular retrogressive thaw slumps (RTS) are abrupt disturbances that expand by up to several meters each year and impact local and regional topographic gradients, hydrological pathways, sediment and nutrient mobilisation into aquatic systems, and increased permafrost carbon mobilisation. The feedback between abrupt permafrost thaw and the carbon cycle is a crucial component of the Earth system and a relevant driver in global climate models. However, an assessment of RTS at high temporal resolution to determine the dynamic thaw processes and identify the main thaw drivers as well as a continental-scale assessment across diverse permafrost regions are still lacking.

In northern high latitudes optical remote sensing is restricted by environmental factors and frequent cloud coverage. This decreases image availability and thus constrains the application of automated algorithms for time series disturbance detection for large-scale abrupt permafrost disturbances at high temporal resolution. Since models and observations suggest that abrupt permafrost disturbances will intensify, we require disturbance products at continental-scale, which allow for meaningful integration into Earth system models.

The main aim of this dissertation therefore, is to enhance our knowledge on the spatial extent and temporal dynamics of abrupt permafrost disturbances in a large-scale assessment. To address this, three research objectives were posed:

1. Assess the comparability and compatibility of Landsat-8 and Sentinel-2 data for a combined use in multi-spectral analysis in northern high latitudes.

2. Adapt an image mosaicking method for Landsat and Sentinel-2 data to create combined mosaics of high quality as input for high temporal disturbance assessments in northern high latitudes.

3. Automatically map retrogressive thaw slumps on the landscape-scale and assess their high temporal thaw dynamics.

We assessed the comparability of Landsat-8 and Sentinel-2 imagery by spectral comparison of corresponding bands. Based on overlapping same-day acquisitions of Landsat-8 and Sentinel-

2 we derived spectral bandpass adjustment coefficients for North Siberia to adjust Sentinel-2 reflectance values to resemble Landsat-8 and harmonise the two data sets. Furthermore, we adapted a workflow to combine Landsat and Sentinel-2 images to create homogeneous and gap-free annual mosaics. We determined the number of images and cloud-free pixels, the spatial coverage and the quality of the mosaic with spectral comparisons to demonstrate the relevance of the Landsat+Sentinel-2 mosaics. Lastly, we adapted the automatic disturbance detection algorithm LandTrendr for large-scale RTS identification and mapping at high temporal resolution. For this, we modified the temporal segmentation algorithm for annual gradual and abrupt disturbance detection to incorporate the annual Landsat+Sentinel-2 mosaics. We further parametrised the temporal segmentation and spectral filtering for optimised RTS detection, conducted further spatial masking and filtering, and implemented a binary object classification algorithm with machine-learning to derive RTS from the LandTrendr disturbance output. We applied the algorithm to North Siberia, covering an area of 8.1 x 10^6 km^2.

The spectral band comparison between same-day Landsat-8 and Sentinel-2 acquisitions already showed an overall good fit between both satellite products. However, applying the acquired spectral bandpass coefficients for adjustment of Sentinel-2 reflectance values, resulted in a near-perfect alignment between the same-day images. It can therefore be concluded that the spectral band adjustment succeeds in adjusting Sentinel-2 spectral values to those of Landsat-8 in North Siberia.

The number of available cloud-free images increased steadily between 1999 and 2019, especially intensified after 2016 with the addition of Sentinel-2 images. This signifies a highly improved input database for the mosaicking workflow. In a comparison of annual mosaics, the Landsat+Sentinel-2 mosaics always fully covered the study areas, while Landsat-only mosaics contained data-gaps for the same years. The spectral comparison of input images and Landsat+Sentinel-2 mosaic showed a high correlation between the input images and the mosaic bands, testifying mosaicking results of high quality. Our results show that especially the mosaic coverage for northern, coastal areas was substantially improved with the Landsat+Sentinel-2 mosaics. By combining data from both Landsat and Sentinel-2 sensors we reliably created input mosaics at high spatial resolution for comprehensive time series analyses.

This research presents the first automatically derived assessment of RTS distribution and temporal dynamics at continental-scale. In total, we identified 50,895 RTS, primarily located in ice-rich permafrost regions, as well as a steady increase in RTS-affected areas between 2001 and 2019 across North Siberia. From 2016 onward the RTS area increased more abruptly, indicating heightened thaw slump dynamics in this period. Overall, the RTS-affected area increased by 331 % within the observation period. Contrary to this, five focus sites show spatio-temporal variability in their annual RTS dynamics, alternating between periods of increased and decreased RTS development. This suggests a close relationship to varying thaw drivers. The majority of identified RTS was active from 2000 onward and only a small proportion initiated during the assessment period. This highlights that the increase in RTS-affected area was mainly caused by enlarging existing RTS and not by newly initiated RTS.

Overall, this research showed the advantages of combining Landsat and Sentinel-2 data in northern high latitudes and the improvements in spatial and temporal coverage of combined

annual mosaics. The mosaics build the database for automated disturbance detection to reliably map RTS and other abrupt permafrost disturbances at continental-scale. The assessment at high temporal resolution further testifies the increasing impact of abrupt permafrost disturbances and likewise emphasises the spatio-temporal variability of thaw dynamics across landscapes. Obtaining such consistent disturbance products is necessary to parametrise regional and global climate change models, for enabling an improved representation of the permafrost thaw feedback.

Zusammenfassung

Permafrostböden erwärmen sich global, was zu weit verbreitetem Auftauen des Permafrosts führt und die angrenzenden Landschaften, Ökosysteme und Infrastruktur beeinflusst. Insbesondere eisreicher Permafrostboden ist anfällig für schnelles und abruptes Auftauen durch Schmelzen von überschüssigem Grundeis. Lokale Fernerkundungsstudien haben für die letzten zwei Jahrzehnte zunehmende Raten abrupter Permafroststörungen festgestellt, wie z. B. Veränderungen und Auslaufen von Thermokarstseen, Küstenerosion und Taurutschungen in eisreichem Permafrost. Dies weist auf eine beschleunigte Permafrostdegradation hin.

Vor allem Taurutschungen (retrogressive thaw slumps) sind sehr abrupte Störungen, die sich jedes Jahr um bis zu mehreren Metern vergrößern. Damit beeinflussen sie lokale und regionale Topographien, hydrologische Gradienten, den Sediment und Nährstofftransport zu Gewässern und verursachen eine erhöhte Freisetzung von organischem Bodenkohlenstoff. Der Rückkopplungsprozess zwischen abruptem Auftauen des Permafrostbodens und dem Kohlenstoffkreislauf, insbesondere seiner zeitlichen Skala, ist ein entscheidender Bestandteil des Erdsystems und für globale Klimamodelle relevant. Es fehlen jedoch noch Untersuchungen mit hoher zeitlicher Auflösung zur Bestimmung der dynamischen Auftauprozesse und zur Identifizierung der wichtigsten Treiber des Permafrosttauens, sowie großräumige Untersuchungen, die heterogene Permafrostregionen umfassen.

In nördlichen hohen Breitengraden ist die optische Fernerkundung durch häufige und anhaltende Wolkenbedeckung beeinflusst, was wiederum die Bildverfügbarkeit stark verringert. Dieses schränkt die Anwendung von automatisierten Algorithmen zur Erkennung von abrupten Permafroststörungen in Zeitreihen mit hoher zeitlicher Auflösung ein. Da Modelle und Beobachtungen darauf hindeuten, dass sich abrupte Permafroststörungen verstärken, benötigen wir Produkte, die die Störungen großräumig darstellen, damit sie zur Parametrisierung der Erdsystemmodelle beitragen können.

Das Hauptziel ist daher, unser Verständnis über die räumliche Ausdehnung und zeitliche Dynamik abrupter Permafroststörungen in einer großräumigen Studie zu erweitern. Um dieses zu erreichen, wurden drei Forschungsziele aufgestellt:

1. Die Bewertung der Vergleichbarkeit und Kompatibilität von Landsat und Sentinel-2 Daten für eine gemeinsame Verwendung in Multispektralanalysen in nördlichen hohen Breitengraden.

2. Die Anpassung einer Bildmosaik-Methode für Landsat und Sentinel-2 Daten, um qualitativ gute gemeinsame Mosaike zu erstellen, welche Datengrundlage für die Analyse von dynamischen Störungen in nördlichen hohen Breitengraden sind.

3. Die automatisierte, großräumige Kartierung von Taurutschungen und die Analyse ihrer zeitlich hochaufgelösten Taudynamiken.

Wir haben die Vergleichbarkeit von Landsat-8 und Sentinel-2 Bildern durch einen spektralen Vergleich der einzelnen Bänder bewertet. Basierend auf taggleichen Bildaufnahmen von Landsat-8 und Sentinel-2 haben wir spektrale Band-Anpassungskoeffizienten für Nordsibirien abgeleitet, um die Sentinel-2-Reflektanzwerte so anzupassen, dass sie Landsat-8 entsprechen und die beiden Datensätze miteinander harmonisiert sind. Darüber hinaus, haben wir einen Mosaikprozess angepasst, um Landsat und Sentinel-2 Bilder in jährlichen Mosaiken zu kombinieren und so homogene und flächendeckende Mosaike zu erstellen. Um die Bedeutsamkeit von Landsat + Sentinel-2 Mosaiken zu demonstrieren, haben wir die Anzahl der Bilder und wolkenfreien Pixel, die räumliche Mosaikabdeckung und die Mosaikqualität durch einen spektralen Vergleich ermittelt. Zuletzt haben wir LandTrendr, ein Algorithmus zur automatisierten Störungserkennung, für die großräumige Identifizierung und Kartierung von Taurutschungen mit hoher zeitlicher Auflösung angepasst. Wir haben den zeitlichen Segmentierungsalgorithmus für die Erkennung von graduellen und abrupten Störungen modifiziert, um die jährlichen Landsat + Sentinel-2-Mosaike zu inkludieren. Des Weiteren haben wir die optimalen Parameter zur zeitlichen Segmentierung und zum spektralen Filtern für Taurutschungen bestimmt, sowie weitere räumliche Maskierungen und Filter angewendet und eine binäre machine-learning Klassifizierung durchgeführt. Wir haben den Algorithmus auf Nordsibirien (8,1 x 10^6 km^2) angewendet.

Der Vergleich der spektralen Bänder von taggleichen Landsat-8 und Sentinel-2 Bildaufnahmen zeigte bereits eine gute Übereinstimmung zwischen beiden Sensorprodukten. Die Anpassung von Sentinel-2 mit den spektralen Band-Anpassungskoeffizienten führte dann zu einer annähernd perfekten Ausrichtung zwischen den Fernerkundungsbildern. Dies verdeutlicht, dass die spektralen Band-Anpassungskoeffizienten die Relektanzwerte von Sentinel-2 in Nordsibirien sehr gut an Landsat-8 anpassen.

Die Anzahl der verfügbaren wolkenfreien Bilder stieg von 1999 bis 2019 stetig an. Ab 2016, als Sentinel-2-Bilder verfügbar wurden, erhöhte sich die Anzahl stark, was auf eine verbesserte Datengrundlage für den Mosaikprozess schließen lässt. Bei einem Vergleich der jährlichen Mosaike deckten die Landsat + Sentinel-2-Mosaike die Untersuchungsgebiete immer räumlich vollständig ab, während die Landsat-Mosaike in denselben Jahren Datenlücken enthielten. Der spektrale Vergleich der Eingabebilder und der Landsat + Sentinel-2-Mosaike zeigte eine hohe Korrelation zwischen den Eingabebildern und Mosaikergebnissen, was auf eine hohe Qualität der Landsat+Sentinel-2 Mosaike hinweist. Unsere Ergebnisse zeigen, dass insbesondere die räumliche Abdeckung für nördliche Küstengebiete mit den Landsat + Sentinel-2-Mosaiken erheblich verbessert wurde. Durch die Kombination von Landsat- und Sentinel-2-Daten konnten zuverlässig Mosaike mit hoher räumlicher Auflösung für Zeitreihenanalysen erstellt werden.

Diese Untersuchung präsentiert die erste automatisierte großräumige Kartierung von Taurutschungen mit hoher zeitlicher Auflösung. Wir identifizierten 50.895 Taurutschungen, hauptsächlich in eisreichen Permafrostregionen, und eine stetige Zunahme der von Taurutschungen betroffenen Fläche von 2001 bis 2019 in Nordsibirien. Ab 2016 nahm die betroffene Fläche auffallend zu, was auf eine erhöhte Taudynamik der Taurutschungen am Ende der Zeitreihe hindeutet. Insgesamt stieg die von Taurutschungen betroffene Fläche im Beobachtungszeitraum

um 331 % an. Im Gegensatz dazu, zeigen 5 Fokusregionen räumlich-zeitliche Variabilität in ihren jährlichen Taudynamiken, welche zwischen Perioden erhöhter und erniedrigter Taudynamiken wechseln. Dies deutet auf eine enge Korrelation zu unterschiedlichen Tautreibern hin. Die Mehrheit der identifizierten Taurutschungen war ab dem Jahr 2000 aktiv und nur ein kleinerer Anteil wurde während des Beobachtungszeitraums initiiert. Dies verdeutlicht, dass die Zunahme der von Taurutschungen betroffenen Fläche hauptsächlich durch die Vergrößerung bestehender Taurutschungen und nicht durch neue Taurutschungen verursacht wurde.

Insgesamt zeigte diese Untersuchung die Vorteile der gemeinsamen Nutzung von Landsat und Sentinel-2 Daten in nördlichen hohen Breitengraden. Die Bildverfügbarkeit steigt drastisch an und die spektrale Anpassung erreicht eine gute Harmonisierung zwischen den beiden Sensorprodukten, welches die Analyse von Landschafts- und Ökosystemveränderungen mit dichten Zeitreihen ermöglicht. Dies ist die Grundlage für die Anwendung eines automatisierten Detektierungsalgorithmuses für abrupte Permafroststörungen, wie Taurtuschungen, auf großräumiger Ebene. Die Untersuchung mit hoher zeitlicher Auflösung belegt die zunehmenden Auswirkungen abrupter Permafroststörungen und betont ebenfalls die räumlich-zeitliche Variabilität dieser. Das Erstellen von konsistenten Datenprodukten zu Störungen ist wichtig, um regionale und globale Kimawandel-Modelle zu parametrisieren und die Rückkopplung zwischen Klimaerwärmung Permafrosttauen besser darzustellen.

Für meine Familie.

Table of Contents

List of Figures

List of Tables

Abbreviations

AOI	Study site center point
AOIarea	Study site 25 × 25 km area
BatA	Batagay adjusted
BP	Before Present
BQA	Quality Assessment Bitmask
ES	Eastern Siberia
ESA	European Space Agency
esA	Eastern Siberia adjusted
ETM+	Enhanced Thematic Mapper Plus onboard Landsat 7
GEE	Google Earth Engine
GT	Ground truth data
Gt	Gigaton
ha	Hectare
HLS	Harmonized Landsat Sentinel-2 Product
ISI	International Scientific Indexing
L8	Landsat-8
LaSRC	Landsat 8 Surface Reflectance Code
LT	LandTrendr
LT-GEE	LandTrendr on Google Earth Engine
LT-LS2	LandTrendr Landsat + Sentinel-2
MAAT	Mean Annual Air Temperature
MATP	Mean Annual Total Precipitation
MSI	Multispectral Instrument onboard Sentinel 2
NDVI	Normalized Difference Vegetation Index
NE Siberia	Northeast Siberia
OLI	Operational Land Imager onboard Landsat 8
RTS	Retrogressive Thaw Slump
S2	Sentinel-2
SAR	Synthetic Aperture Radar
SR	Surface Reflectance
SNAP	Sentinel Application Platform
TOA	Top-Of-Atmosphere
TM	Thematic Mapper onboard Landsat 4 and Landsat 5
USGS	United States Geological Survey
YakA	Yakutsk Adjusted

1 Introduction

1.1 Scientific background and motivation

The climate system is changing at an unparalleled pace over the last decades to millennia (IPCC 2014). Foremost, the Earth is warming, both on land and ocean, the precipitation regimes are intensifying, and sea levels are rising. By now, the human impact on the climate system is unequivocal, with current anthropogenic greenhouse gas emissions at an unprecedented high. In return, climate change widely impacts the human and natural system (IPCC 2014). Observations of the last two decades show that in the Arctic, the area roughly north of 60 °N latitude, the surface air temperature has been warming at more than double the global average (Meredith et al. 2019; AMAP 2017). Furthermore, modelled projections for changes in surface temperature and precipitation show that the Arctic will experience the strongest warming and precipitation changes by the end of the century, mainly driven by mass loss of ice sheets and glaciers and decreasing sea ice extent and spring snow cover in the cryosphere (IPCC 2014). These observations and modelling results show that the temperature variability and warming trends in the Arctic are larger than the global trends, a phenomenon called Arctic amplification (Serreze and Barry 2011). This highlights the significant role of the Arctic in global climate warming, especially as the Arctic is at the interface of atmosphere, hydrosphere, geosphere, biosphere and, very importantly, cryosphere, linked by strong coupled feedback systems in the energy, water and carbon cycle (AMAP 2017; Lenton 2012). The importance of the cryosphere for the Arctic extends further to the role of permafrost. Permafrost is another component of the cryosphere that experiences warming (Biskaborn et al. 2019) but compared to sea ice, glaciers and ice sheets long time series data comprehensively assessing the effect of climate warming on the state and extent of permafrost is still missing. Yet, the state of the permafrost is a crucial factor in the future as huge quantities of organic carbon are stored in frozen soils, which will contribute to the carbon cycle after thaw, impacting the wider climate (Lenton et al. 2019). Despite this knowledge, the magnitude and timing of the feedback between permafrost and climate change still remains uncertain (Schuur et al. 2015).

1.1.1 Permafrost and climate change

Permafrost is warming globally and experiencing widespread permafrost thaw (Biskaborn et al. 2019; Vasiliev et al. 2020; Farquharson et al. 2019). Defined as ground that remains at or below a temperature of 0 °C for at least two consecutive years, permafrost is composed of soil, rock, organic material and varying quantities of ice (Van Everdingen et al. 1998). Permafrost is a dominant feature in the unglaciated terrestrial Arctic, currently affecting about 22 % of the land surface in the northern hemisphere (Obu et al. 2019). Further, permafrost is found as subsea permafrost in Arctic shelf regions (Overduin et al. 2019), in unglaciated areas of Antarctica (Guglielmin and Vieira 2014), and in high mountainous regions outside the northern high latitudes (Kääb et al. 2007; Obu et al. 2019). Permafrost formed during the Quaternary glacial periods in non-glaciated areas, where extremely cold winter temperatures and low snow cover depth prevailed, causing a long-term negative annual energy balance of the ground surface (Hubberten et al. 2004). As permafrost is defined by the thermal state of the ground, it is very sensitive to changes in the energy balance and dominant thermal regime.

The thermal state of permafrost is directly impacted by global climate warming. Rising air temperatures and changing precipitation regimes increase the ground temperature, which leads to widespread permafrost thaw and eventually near-surface permafrost loss (Serreze and Barry 2011; Chadburn et al. 2017; Biskaborn et al. 2019). Changes in the state and distribution of permafrost have wide implications for local to regional landscapes (Jorgenson and Grosse 2016), impacting ecosystems (Schuur and Mack 2018; Pastick et al. 2019), hydrological systems (Francis et al. 2009; Liljedahl et al. 2016), soil carbon accumulation and decomposition (Hicks Pries et al. 2015), greenhouse gas emissions (Walter Anthony et al. 2018), and infrastructure stability (Hjort et al. 2018). A major concern regarding the feedback between global climate change and permafrost thaw is its potential contribution to the global carbon cycle, as approximately 1300 Gt, with an uncertainty range of 1100 to 1500 Gt, of organic carbon is stored in the northern circumpolar permafrost regions, which is almost twice as much carbon as currently in the atmosphere (Hugelius et al. 2014; Strauss et al. 2017a; Schuur et al. 2015). Extensive permafrost thaw induces the mobilisation of soil organic carbon and the release of greenhouse gases, mainly carbon dioxide and methane, impacting the global carbon cycle and thus, creating a positive feedback between climate change and permafrost thaw (Grosse et al. 2011a; Schuur et al. 2015; Walter Anthony et al. 2018). Therefore, it is of high relevance to understand and estimate the magnitude, speed and distribution of permafrost thaw and incorporate this in climate models. Currently, only simplified relations between air temperature increase and gradual permafrost thaw are included but more complex thaw processes are missing by lack of data (Schuur and Abbott 2011), although observations and local models show that abrupt permafrost thaw releases substantial amounts of carbon on short time scales (Walter Anthony et al. 2018; Turetsky et al. 2019; Turetsky et al. 2020).

1.1.2 Permafrost thaw and disturbances

The feedback between global climate warming and permafrost thaw is highly influenced by environmental and ecosystem properties, such as topography, surface water, groundwater, soil

properties, vegetation, and snow distribution (Jorgenson et al. 2010), by local to regional spatial and temporal variability of climate conditions, as well as by varying anthropogenic pressures (Kokelj and Jorgenson 2013). Thus, the changes in permafrost and permafrost thaw features are diverse and heterogeneous. Widely observed thaw processes are active layer deepening (Park, Kim, and Kimball 2016), which describes the ground layer that experiences annual thawing and freezing (Van Everdingen et al. 1998), thermokarst (Kokelj and Jorgenson 2013; Olefeldt et al. 2016), which is the thawing of ice-rich permafrost or melting of massive ground ice leading to extensive permafrost ground subsidence (Van Everdingen et al. 1998) and thermal erosion (Are 1988), as erosion of permafrost ground by a combination of thermal and mechanical processes such as hydraulic transport of ground material (Van Everdingen et al. 1998). These processes trigger thaw features such as surface subsidence (Antonova et al. 2018), degrading ice wedge polygons (Liljedahl et al. 2016), thermo-erosional gullies and vallies (Günther et al. 2013), thermokarst lakes and dynamics (Grosse, Jones, and Arp 2013), active layer detachment slides (Lewkowicz 2007), coastal erosion (Irrgang et al. 2018; Jones et al. 2018) and retrogressive thaw slumps (Burn and Lewkowicz 1990). These landscape changes and climate-induced permafrost disturbances degrade the permafrost and play a particularly important role in the release of carbon dioxide and methane due to thaw.

Permafrost disturbances can be differentiated by their spatial extent, their temporal development, complexity of the process and the overall impact on the soil organic carbon pool (Grosse et al. 2011a). Mainly focusing on the spatial extent and the temporal dimension, it can be distinguished between press and pulse permafrost disturbances. Press disturbances primarily evolve gradually and slowly from decades to centuries affecting large-scales, such as active layer deepening (top-down thaw), aridification, paludification, and changes in vegetation composition. These press disturbances, but not all, mostly affect the near-surface soil organic carbon pools by seasonal freeze-thaw processes. Contrary to this, pulse disturbances mainly occur locally as fast and abrupt, short-term events. Wildfires, thermokarst lake drainage, flooding and rapid soil erosion are pulse disturbances, developing within a few days to decades. Thermokarst processes and rapid soil erosion are examples of pulse disturbances that affect the deeper soil organic carbon pools due to extensive thaw, which would otherwise be unaffected by seasonal gradual disturbances (Grosse et al. 2011a). Because of this, particularly abrupt thaw disturbances induce the release of a substantial amount of carbon, mainly by collapsing ground, and fast and deep erosion as in active layer detachment slides, retrogressive thaw slumps and thermo-erosional gullies and vallies (Turetsky et al. 2020). While abrupt thaw is predicted to occur on less than 20% of the permafrost land area by 2300 (Turetsky et al. 2020), these thaw-prone ice-rich areas are particularly carbon-rich (Olefeldt et al. 2016). Thus, abrupt thaw could affect half the sequestered permafrost carbon by 2300 due to its capability to affect also deep soil layers according to models (Turetsky et al. 2019; Turetsky et al. 2020). The differences of press and pulse disturbances emphasises the variability of permafrost disturbances in time and space, and in their potential effect on the soil organic carbon pool. Despite this, not even all current Earth System Models include gradual large-scale permafrost thaw as representation of permafrost processes and lack abrupt thaw completely. To implement gradual and abrupt thaw processes caused by disturbances in such global-scale

models, an understanding of the abundance, distribution and especially temporal dynamics of abrupt permafrost thaw disturbances is necessary. This requires the development of consistent observation products with spatially and temporally continuous data on at least large regional scales, which are relevant for Earth System Models (Schneider von Deimling et al. 2012; Nitze et al. 2018; Turetsky et al. 2019).

1.1.3 Abrupt permafrost disturbances

The most prominent abrupt permafrost disturbances are thermokarst lake dynamics, retrogressive thaw slumps, and wildfires as they substantially alter landscapes and ecosystems on local to landscape-scales by impacting hydrology, vegetation and soil structure, albedo properties and carbon sequestration and release (Grosse et al. 2011a). While we have a general understanding of the impact these disturbances have on their surrounding landscape and their impact on permafrost, substantial knowledge gaps remain related to their spatial and temporal dynamics (Nitze et al. 2018). Turetsky et al. 2019 suggest slope erosion as a priority research area, as these indicate the thawing of ice-rich permafrost on particular high temporal scales and occur mostly in very carbon-rich region. Hence, they are a critical permafrost disturbance component with strong impacts on the carbon cycle. Retrogressive thaw slumping is the process of slope failure resulting from thawing of ice-rich permafrost occurring on bluffs and hill slopes. This ice-rich permafrost is found either in Yedoma regions (Strauss et al. 2017a) or formerly glaciated areas still preserving buried glacial ice (Kokelj et al. 2017). Retrogressive thaw slumps (RTS) are considered 'the most dramatic manifestations of permafrost thaw' (Kokelj and Jorgenson 2013). The initiation can result from a variety of triggers including fluvial processes, thermoerosion or mass wasting after precipitation or extreme thaw (Kokelj and Jorgenson 2013). Once initiated, RTS expand successively into the landscape by retrogressive growth, as permafrost thaw continues in the following thaw seasons, exposing more ice-rich permafrost along a steep headwall, forming a slump floor and building a debris flow from the thawed sediment and meltwater (Van Everdingen et al. 1998). RTS vary in size from under 0.15 ha to mega thaw slumps in the range of 52 ha (Ramage et al. 2017; Kokelj et al. 2015a; Lacelle et al. 2015), to more than 80 ha, such as Batagay in central Yakutia (Günther et al. 2015). RTS growth rates, often expressed in headwall retreat rates, range from meters to tens of meters per year, which indicates their highly dynamic development (Kokelj and Jorgenson 2013). Additionally to this, RTS can be polycyclic and alternate between periods of active degradation and periods of stabilised dormancy (French and Williams 2007), with spatially varying re-initiation of only parts of a stabilised RTS (Balser, Jones, and Gens 2014; Kokelj et al. 2009).

Current RTS studies and assessments are mostly remote sensing-based or a combination of remote sensing and field-based observation data (Lantuit and Pollard 2005; Kokelj et al. 2015b; Séjourné et al. 2015). Remote sensing approaches can be differentiated according to their spatial scale and temporal resolution of assessment data. Mostly, RTS dynamics were estimated from single or few aerial photographs from finite points in time and sparse field visits for a cluster of slumps at a local scale (Lantz and Kokelj 2008; Lantuit and Pollard 2005;

Lantuit and Pollard 2008; Balser, Jones, and Gens 2014; Segal et al. 2016; Ardelean et al. 2020; Luo et al. 2019; Séjourné et al. 2015; Mu et al. 2020). Based on manually digitised RTS extents in images from different years, these studies derived accelerating slump activities from increasing slump numbers, headwall retreat rates or slump areas. While the overall RTS trend is explicit, the results are difficult to compare as the time periods covered vary and mostly depend on image availability and variable selection of observation periods, which might either not represent the thaw dynamics adequately or result in challenges to compare studies across sites. Elaborating on this, disturbance trends from multi-decadal Landsat image stacks indicate the distribution and abundance of active RTS for regional sites in Canada, Alaska, and Siberia (Brooker et al. 2014; Nitze et al. 2018; Kokelj et al. 2015a; Lacelle et al. 2015). These studies applied for the first time an automatic mapping approach for RTS, showing their regional distribution and underlining that local disturbances occurring in regional clusters have a significant impact on the landscape-scale. While these studies use the whole image archive for a period of time as input and assess regional-scales, their results are temporal trends and do not depict dynamic changes explicitly. Similarly, a first deep learning algorithm derived RTS for a local site in Tibet with high spatial accuracy but so far this approach is still limited in its temporal resolution and upscaling capability to large-scale assessments (Huang et al. 2020). First assessments at high temporal resolution were conducted by Ward Jones et al. (2019) and by Lewkowicz and Way (2019) with nearly annual input data for study sites in the Canadian High Arctic. Both studies found accelerating slumping dynamics in their respective observation periods. The high temporal resolution input data present changes in annual or biennial slumping activities, which emphasises the variability of RTS dynamics from year-to-year. While this gives insight into the highly dynamic nature of RTS, the results are based on manual digitisation and visual interpretation of yearly images and therefore only cover small-scale assessments. Although the increase of RTS dynamics is explicit, the main climatic drivers identified for intensification of thaw slumping differ and are not reliably determined yet. Slumping activity has been associated with increasing air temperatures (Ward Jones, Pollard, and Jones 2019; Lewkowicz and Way 2019; Luo et al. 2019), strong precipitation events (Kokelj et al. 2015a; Luo et al. 2019; Segal et al. 2016), as well as thawing degree days (Ward Jones, Pollard, and Jones 2019) and reduced spring snow cover (Balser, Jones, and Gens 2014). As indicated by Ward Jones, Pollard, and Jones 2019 and Lewkowicz and Way 2019, RTS dynamics are highly variable on an annual to biennial scale and therefore a clear correlation between slumping dynamics and climatic drivers can only be drawn from high temporal assessments, which are currently lacking regional to large assessment scales. Similarly, the local assessment scales may not be representative across the wider permafrost region and therefore restrict projections of RTS dynamics to the landscape scale.

The variety of previous studies advanced our knowledge of RTS greatly and show prospects of further studies. On the one hand high temporal resolution assessments improve our understanding on the RTS dynamics and on the other hand automatic mapping methods allow for large-scale assessments. Combining both approaches will present the possibility to derive spatially and temporally continuous data and assess RTS at high temporal resolution, as necessary for inclusion in Earth system models. This is in agreement with Turetsky et al. (2020

suggesting that high temporal assessments are required to fully understand rapid permafrost disturbances and their temporal variability and being able to determine the main climatic drivers. Further, large-scale evaluations are necessary, which consider RTS distributions and are representative for heterogeneous permafrost regions. Only with consistent regional to landscape-scale assessments of the highly dynamic RTS processes our understanding of the feedback between global climate warming and abrupt permafrost thaw can be enhanced and these processes be included in Earth System Models for more accurate projections of future changes.

1.1.4 Remote sensing

Satellite remote sensing is a discipline that addresses Earth's environmental and physical characteristics from space and offers distinctive advantages for assessing and monitoring spatial and temporal processes both at local and landscape-scale (Militino, Ugarte, and Pérez-Goya 2018). Satellite-based Earth observations now span the last seven decades. At the beginning only with sporadic acquisitions, depending on the missions, but in particular since 2000 with enhanced spatially and temporally continuous acquisition coverage (Barnes and Salomonson 1992; Irons, Dwyer, and Barsi 2012). The remote sensing satellite and sensor characteristics differ profoundly from one another but can be grouped in active and passive sensors and differentiated by spatial, temporal, and spectral resolution as well as their acquisition lifetime. Both the public and private sector recognise progressively the value and demand of remote sensing data and hence, develop divers sensor and mission concepts (Tatem, Goetz, and Hay 2008). Technological advancements in the last decade led to an increased remote sensing algorithm development and application scope. The reliable, continuous and repeated acquisition of satellite images contributes to high quality image archives with an unprecedented amount of available data offering a multitude of analysis opportunities. Especially open access policies of image archives, enhanced data availability and possible application scopes greatly (Woodcock et al. 2008; Zhu et al. 2019). While data availability improved, also advances were made in data storage, cloud computing and product distribution systems to enable big Earth observation data management and analysis (Sudmanns et al. 2020). Newly accessible cloud-computing and storage platforms such as Google Earth Engine, Sentinel Hub and Open Data Cube at no or little costs, provide the resources for large and big data processing to a much bigger user group, fostering the development of new technologies and algorithms greatly (Gomes, Queiroz, and Ferreira 2020; Sudmanns et al. 2020).

Especially the field of remote sensing time series enhanced greatly in the last decades. In contrast to basic change detection, temporally dense time series illustrates not only the stationary pre- and post-change status but the dynamic development of land surface changes. If additionally data is available at large or even global scale, the analysis can address spatio-temporal variability and help identifying drivers and causes (Kuenzer, Dech, and Wagner 2015). Time series assessments have emphasised for example the loss in forest, the expansion of urban and agricultural areas into natural space, as well as the decline in sea ice cover. Furthermore, time series analysis allows to determine the temporal rate of change and

differentiation between long-term dynamics or short-term disruptions of the environment, which makes it a highly valuable and powerful tool for landscape change detection (Kuenzer, Dech, and Wagner 2015).

1.1.5 Remote sensing of permafrost disturbances

Remote sensing allows spatially continuous observations across extensive geographic areas which is especially beneficial for the widely inaccessible and climatically harsh Arctic regions, including vast permafrost regions. Such observations provide spatial context for the few field studies conducted there due to the highly challenging access to these regions. These areas would remain largely unstudied without satellite remote sensing (Westermann et al. 2015a). Permafrost cannot be monitored directly from remote sensing as it is defined by subsurface physical properties. Instead, characteristic permafrost features and landscape changes can be detected, monitored and used as indicators for the state of permafrost and permafrost degradation processes (Westermann et al. 2015a). Detectable landscape characteristics or changes which can be associated with permafrost dynamics for monitoring include changes in surface temperature, vegetation cover and structure, surface water, topography, soil erosion and disturbances such as from fire and human activities (Jorgenson and Grosse 2016).

Landforms shaped by thermokarst and thermo-erosion processes indicate the loss of ground ice due to ice melt and are some of the best indicators of active local permafrost thaw also observable with remote sensing (Jorgenson and Grosse 2016). RTS can be identified from multi-spectral remote sensing images as the change in land cover from vegetation to soil, scar zone and debris flow can be differentiated spectrally from its surrounding and temporally in change detection brooker2014mapping. Besides, the deep soil erosion after ice-rich permafrost thaw leads to a change in ground volume and can therefore be determined from repeat elevation measurements (Kääb 2008). As outlined in section 1.1.3 the remote sensing methods applied so far for RTS assessment primarily rely on manual digitisation or visual interpretation, which provides spatially high detail but is labour and time intensive and restricts the assessment to small-scale study sites. Further, the mostly low temporal resolution used in such methods prevents detection of high annual variability of RTS dynamics. Various recent image processing methods assessing land surface disturbances with temporally dense Earth observation data now rely on automatic disturbance detection algorithms for regional to global scale applications from image time series data, capturing temporal dynamics (Zhu 2017). The increased free availability of image archives and the enhancement in data storage and processing capabilities in the last decade, fostered algorithm development and enabled for the first time global-scale assessments of land surface changes at high temporal resolution (Woodcock et al. 2008; Wulder et al. 2019).

Especially the Landsat archive has been exploited for the scientific applications of image time series as it contains the longest, continuous and freely-available image collection. Landsat is particularly versatile as it contains multi-spectral bands with acquisitions at high spatial resolution of 30m, which allows for comprehensive spectral change detection with high

spatial details, making the images, the various band combinations, and a range of secondary multi-spectral band indices useful for a plethora of application fields (more details on Landsat in section 1.4) (Wulder et al. 2012; Zhu et al. 2019). For example, a global forest loss and gain product (Hansen et al. 2013) as well as a global water change product (Pekel et al. 2016) were developed from Landsat data, both determining long-term trends and annual changes for these observation features for multiple decades. Ecosystem changes and landscape dynamics have also been identified from spatio-temporal Landsat data for Arctic regions. The sensitivity of Arctic ecosystems to external drivers is described by (Pastick et al. 2019) as Arctic greening from vegetation growth associated to air temperature increase, as well as browning trends from increasing evaporative trends in Alaska. Comparable spatio-temporal landscape trends were also determined in the biggest Arctic delta in Russia (Nitze and Grosse 2016). For boreal forests in Canada similar ecosystem greening and browning trends were derived from multi-spectral time series data. However, the main change driver was determined to be disturbance-recovery dynamics and not climate-induced change, as suggested by previous low resolution (e.g. AVHRR) assessments (Sulla-Menashe, Woodcock, and Friedl 2018). These and other Landsat-based assessments underline the landscape heterogeneity of permafrost regions and the variability of Arctic ecosystems to change.

A range of change detection and disturbance analysis algorithms are now widely used and include the Landsat-based detection of Trends in Disturbance and Recovery (LandTrendr) (Kennedy, Yang, and Cohen 2010), the Continuous Change Detection and Classification model (CCDC) (Zhu and Woodcock 2014), the Break detection For Additive Season and Trend (BFAST monitor) (Verbesselt, Zeileis, and Herold 2012), and the vegetation change tracker (VCT) (Huang et al. 2010). These algorithms all rely the on spatially and temporally comprehensive Landsat image archive and detect disturbances from time series analysis but differ in assessment focus and temporal input data frequency. Hence, the change detection varies in temporal resolution, the change indices used, the capacity to detect gradual or abrupt change, and whether they allow past disturbance detection or near real-time monitoring (Zhu 2017). Therefore, these algorithms are not equally suitable for transfer to other application areas but display a variety of already existing disturbance detection possibilities.

The basis of reliable disturbance detection analysis is a consistent and dense image database which fulfills the required temporal and spatial coverage for an application in permafrost regions. However, passive remote sensing has some severe limitations in northern high latitudes due to environmental factors, such as frequent snow, ice and cloud cover, low solar illumination geometry and a short growing season length, reducing the amount of available and usable Earth observation data drastically (Ju and Roy 2008). This diminishes the applicability of most developed algorithms for long-term time series change detection in the Arctic, as they require high frequency data input. While Landsat images are acquired every 16 days, with an increased acquisition frequency in the northern high latitudes from their overlapping polar-orbit swaths, the likelihood of obtaining qualitatively good images in the Arctic summer period is highly reduced due to frequent cloud coverage. The number of usable images strongly varies year-by-year depending on weather conditions, which decreases the spatial and temporal

coverage from Landsat data.

A way to increase the image database for time series analysis in northern high latitudes is to not only rely on images from one sensing system but to include data from multiple optical sensor. This increases the number of usable images and will enhance the database greatly, allowing the implementation of existing disturbance detection algorithms and enabling the identification of permafrost disturbances from high temporal time series analysis. In 2015, the ESA Sentinel-2 mission, as part of the European Commission and ESA Copernicus program, started and acquires optical images with two sensors (more details on Sentinel-2 in section 1.4). The Sentinel-2 and Landsats' sensors have very similar acquisition specifications and therefore their combined use for terrestrial monitoring has been anticipated already before the Sentinel-2 launch and inspired discussions on possible enhanced assessment opportunities (Wulder et al. 2015; Drusch et al. 2012). A crucial benefit is the enhanced data availability from simultaneously-operating Landsat and Sentinel-2 sensors. This especially strengthens the database for Arctic regions due to converging polar-orbits in close proximity to one another, resulting in frequent overlaps of acquisition orbits in the northern high latitudes. This leads to image acquisitions every 1-3 days together from both systems (Li and Roy 2017). This high acquisition frequency increases the likelihood of obtaining cloud-free, good quality optical images tremendously. Hence, the overall disadvantage of optical remote sensing in high latitudes can be compensated by the combined use of images from multiple sensors, establishing a database of temporally dense observations to assess northern high latitude permafrost disturbances with optical remote sensing data. Thus, a high temporal and spatial coverage of permafrost regions is possible by a combined data pool and disturbance detection from time series analysis that captures high temporal dynamics is feasible.

1.2 Aims and objectives

The main objective of this research is to enhance our knowledge on the spatial extent and temporal dynamics of abrupt permafrost disturbances on the regional to landscape-scale with remote sensing. To address this, we primarily concentrate on improving and creating a reliable and adequate remote sensing database that enables high temporal time series analysis. Furthermore, we adapt and modify disturbance analysis algorithms to be transferable to northern high latitudes and the be applicable to permafrost disturbance assessment. Lastly, we focus on the spatial and temporal assessment of abrupt permafrost disturbances (Figure 1.1).

The following three sub-objectives provide the basis for the work of the thesis:

1. To assess the comparability and compatibility of Landsat and Sentinel-2 data for a combined use in multi-spectral analysis in northern high latitudes.

2. To adapt an image mosaicking method for Landsat and Sentinel-2 data to create qualitative good combined mosaics as input for high temporal disturbance assessments in northern high latitudes.

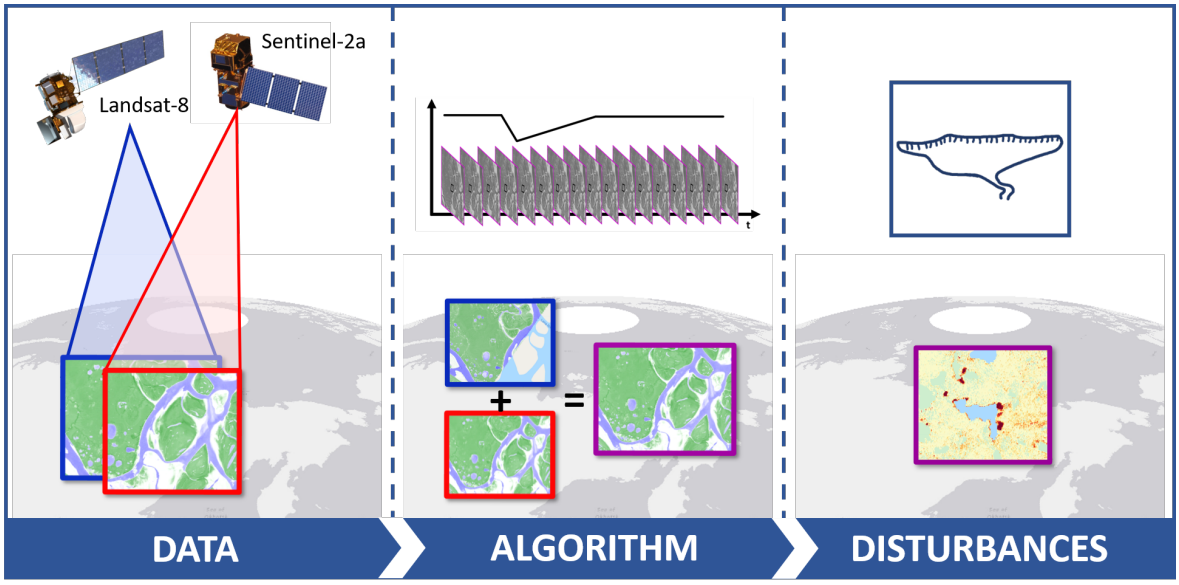

Figure 1.1: The research of this thesis follows a linear path of establishing a robust multi-spectral image database and adapting a time series algorithm for high temporal abrupt permafrost disturbance assessment in North Siberia.

3. To automatically map retrogressive thaw slumps on the landscape-scale and assess their high temporal thaw dynamics.

1.3 Study area

The terrestrial northern high latitudes in North Siberia are the study area of this dissertation, encompassing an area of approximately 8,109,000 km^2, roughly spanning from Taymyr Peninsula in the West (80° E) to the coast of Chukotka in the East (170° W), and from 77° N to 55° N. This area comprises a range of geologic, geomorphologic, climatic and vegetational conditions and a variety of landscapes and land cover types in the Siberian permafrost region. North Siberia experienced very cold and dry continental climate conditions during the Last Glacial Maximum at around 21 ka BP. During this past glacial period the North Siberian mainland reached maximum cold-climate conditions with overall low snow cover conditions while remaining ice-free, which fostered the formation of deep permafrost, as thick as 1,500m, across the region (Hubberten et al. 2004). The combination of extreme continental climate and low topographic gradients favoured the accumulation of ice-rich permafrost deposits, called Yedoma, which can be found extensively across East Siberia (Strauss et al. 2017a). Warming during the Holocene then led to thermokarst-dominated developments transforming whole landscapes by widespread thermokarst lake formation, growth and drainage (Grosse et al. 2007). Despite these changes during the Holocene warming, vast areas of North Siberia continue to be underlain by permafrost. Ranging from continuous permafrost in the north to discontinuous and sporadic permafrost in the South (Figure 1.2).

The study area lies within the arctic and boreal climate zones and spreads from maritime, coastal areas to continental inland areas, covering a variety of broad climate regions. Mean annual air temperatures from specific sites within this region range from -41.7°C (Batagay)

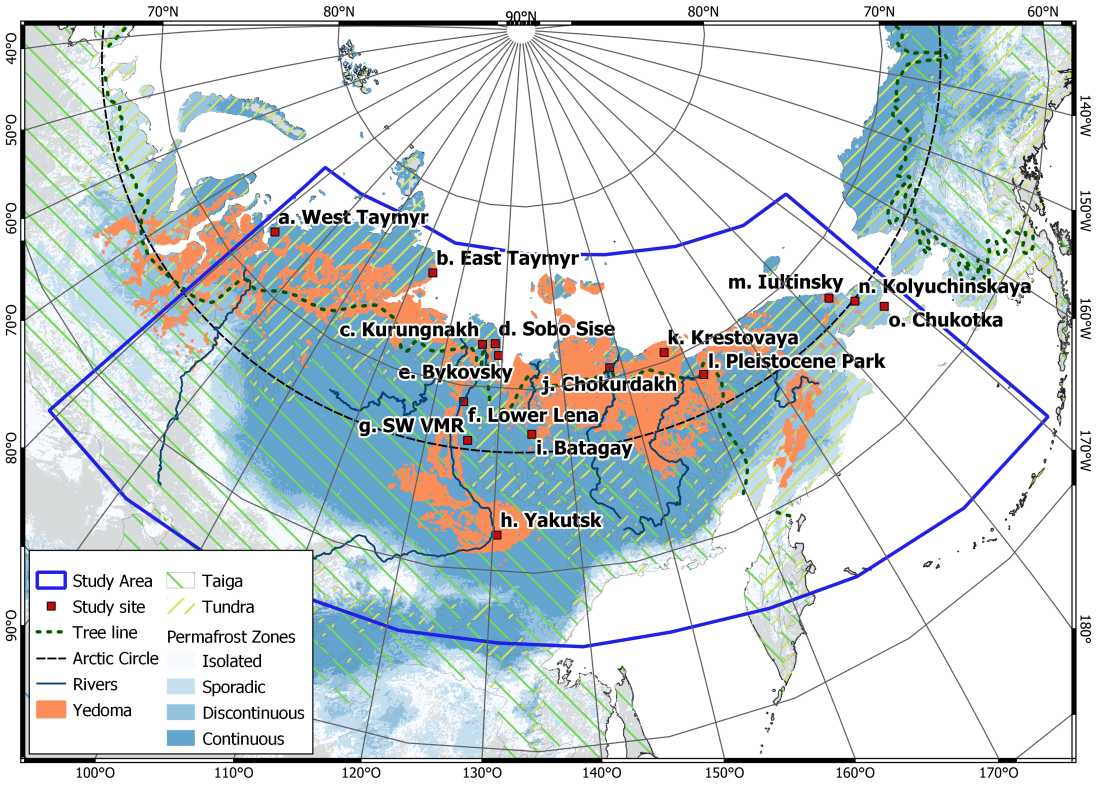

Figure 1.2: The study area North Siberia, with individual study sites from the research chapters. From West to East: a. West Taymyr, b. East Taymyr, c. Kurungnakh, d. Sobo Sise, e. Bykovsky, f. Lower Lena, g. Southwest Verkhoyansk Mountain Range, h. Yakutsk, i. Batagay, j. Chokurdakh, k. Krestovaya, l. Pleistocene Park, m. Iultinsky, n. Kolyuchinskaya, and o. Chukotka.Permafrost zones according to Obu et al. (2019), Yedoma extent according to Strauss et al. (2016), ecosystems according to Olsen et al. (2001) and rivers according to Natural Earth Data (2008)

to -19.9°C (Chukotka) in January and 3.8°C (East Taymyr) to 19.4°C (Yakutsk) in July (Copernicus Climate Change Service 2017). Mean annual total precipitation varies between 0.052m (Chukotka) and 0.020m (Krestovaya). Similarly the study area comprises both taiga and tundra ecoregions, signifying a diverse range of land and vegetation covers, including wet and dry sedge-, moss- and grass-dominated tundra and boreal forest with evergreen spruce, deciduous larch and hardwood birch (Olson et al. 2001; Schneider, Grosse, and Wagner 2009). The study area is largely influenced by big river systems, such as the Lena, Kolyma, Yenisei, Yana, Olenyok, Indigirka and Anadyr, which all have permafrost-dominated watersheds, as well as several mountain ranges such as the Central Siberian Plateau, Byrranga, Verkhoyansk, Cherskiy, Kolyma, and Koryak mountains. The mountain ranges are defined by extensive glaciation during the LGM and a significant proportion of steep bedrock contains permafrost, which is described by the thermal state of the ground just like low-land permafrost. However, mountain permafrost is predominantly characterised by barren ground, block fields and debris slopes and considered to be relatively ice and organic-poor compared to low-land permafrost (Etzelmüller et al. 2020). While mountain permafrost is an emerging research field and also of relevance to North Siberia, it is excluded from this study as we focus on low-land permafrost disturbances.

1.4 General data and methods

This chapter briefly introduces the main data sets and processing software used in this dissertation, while the detailed descriptions of data and methods are provided in the scientific papers.

1.4.1 Landsat and Sentinel-2

The longest passive, optical satellite record is provided by the Landsat program. Since 1972, the Landsat satellite sensors have acquired consistently high spatial resolution images along their polar-orbits with a nominal 16-day temporal frequency, providing continuous coverage of the global landmasses in the visible, near-infrared, shortwave-infrared and thermal-infrared wavelength spectrum (Wulder et al. 2019). A key component of the Landsat program is continuity and overlap of their missions and sensors and an elaborated set of quality assuring atmospheric correction (Roy et al. 2016b; Schmidt et al. 2013), radiometric calibration (Roy et al. 2016a; Chander, Markham, and Helder 2009; Mishra et al. 2014) and cloud masking (Zhu, Wang, and Woodcock 2015) algorithms. These sensor characteristics make the Landsat program very valuable, enabling a wide scope of different applications. The use of Landsat images increased drastically when the full archive was opened and access made freely available in 2008 (Woodcock et al. 2008). New possibilities of large-scale (up to global-scale) as well as long continuous time series arose and fostered the development of new scientific analysis algorithms and methods, taking advantage of a Petabyte-scale imagery data volume never before available (Zhu et al. 2019). Following this, an extensive portfolio of Landsat-based time series change detection algorithms was developed, which cover a wide range of application fields, such as land cover change (Zhu and Woodcock 2014), forest change and disturbance (Kennedy, Yang, and Cohen 2010; Huang et al. 2010; Hansen et al. 2013), and vegetation disturbance (Verbesselt, Zeileis, and Herold 2012).

In 2015 the European Space Agency (ESA) launched the first Sentinel-2 satellite, Sentinel-2A, as part of the Copernicus program and in 2017 the second, Sentinel-2B. The Sentinel-2 satellites are sun-synchronous polar-orbiting with a temporal acquisition frequency of 10 days at the equator individually and together with an acquisition frequency of every 5 days, as the two satellites are phased at 180° to each other. Their sensor specifications are similar to the Landsat series and contain spectral bands covering the visible, near-infrared to short-infrared wavelength spectrum ranges, with spatial resolutions of 10, 20 and 60m (Drusch et al. 2012; ESA 2015). In particular, the increased combined temporal acquisition frequency from the two platforms makes the use of Sentinel-2 data highly compelling for high temporal resolution time series analyses at enhanced medium spatial resolution. Sentinel-2 benefits from the atmospheric correction and cloud masking algorithms developed for Landsat, as these algorithms are now being transferred and adapted for Sentinel-2 (Zhu, Wang, and Woodcock 2015; Hollstein et al. 2016; Main-Knorn et al. 2015; Louis et al. 2016).

1.4.2 Google Earth Engine

Google Earth Engine (GEE) is a cloud-based processing platform for geospatial analysis, free of charge to the user. GEE comprises a multi-petabyte analysis-ready data catalogue and is empowered by Google's extensive online computational capabilities, which creates a very unique and convenient framework for geospatial applications. Since the data products are analysis-ready and stored on Google servers, the users are not restricted by their own storage limitations, data transfer limitations, and computing capabilities and therefore are free in their study design. This easily allows for planetary-scale assessments, enabling whole new assessment approaches that were unavailable before (Gorelick et al. 2017). The data catalogue includes the image archives of freely available sensors such as MODIS, Landsat and Sentinel-2, updating the image repositories with new data acquisitions continuously. Furthermore, thematic data products, such as land cover maps and reanalysis climate data are available as well, providing the opportunity to conduct full scientific data processing and analysis in GEE. In addition to the data catalogue, GEE also comprises an extensive dictionary of predefined functions and algorithms, including standard remote sensing calculations like the normalized difference vegetation index (NDVI), as well as more sophisticated algorithms for unsupervised and supervised image classifications, image segmentation and temporal segmentation. Furthermore, their Javascript and Python application programming interfaces allow for customized processing workflows and applications, which is further enhanced by GEE's compatibility to for example TensorFlow (Google Developers 2021).

1.5 Thesis structure

This thesis contains five chapters, starting with an introduction on the scientific background, state-of-the-art, and introducing the research objectives in chapter 1. Following this, three scientific main chapters in the form of manuscripts are included (Chapter 2, 3, and 4). Finally an overall synthesis and discussion (chapter 5) concludes the thesis. Chapters 2 and 3 are original publications that have been published in peer-reviewed and International Scientific Indexing (ISI) listed scientific journals. Chapter 4 has been accepted for review in a peer-reviewed and ISI listed scientific journal. The details of the published work are stated in section 1.6. The study in chapter 2, 'Comparing Spectral Characteristics of Landsat-8 and Sentinel-2 Same-Day Data for Arctic-Boreal Regions', assesses the comparability and compatibility of two optical remote sensing image products, from Landsat-8 and Sentinel-2, in the Arctic-Boreal Regions of Siberia for a combined use. Chapter 3, 'Mosaicking Landsat and Sentinel-2 Data to Enhance LandTrendr Time Series Analysis in Northern High Latitude Permafrost Regions', further elaborates on this and assesses the possibility to create image mosaics from both Landsat and Sentinel-2 images for an improved spatial and temporal coverage in time series analysis in northern high latitudes. Chapter 4 'Remote Sensing Annual Dynamics of Rapid Permafrost Thaw Disturbances with LandTrendr', presents the adaptation and parametrisation of LandTrendr to rapid permafrost disturbances and the assessment of high temporal resolution thaw dynamics of retrogressive thaw slumps. In chapter 5, the results and implications of the individual research chapters, on the basis of the thesis objectives, are synthesised and generally discussed. The three main research chapters represent stand-alone independent

research. There is some overlapping general information between the manuscripts as the study areas overlap and the data and methods build upon each other.

1.6 Overview of publications and authors' contribution

1.6.1 Chapter 2 - *Comparing Spectral Characteristics of Landsat-8 and Sentinel-2 Same-Day Data for Arctic-Boreal Regions*

Authors: Alexandra Runge and Guido Grosse
Remote Sensing, 2019, 11(14), doi: 10.3390/rs11141730

This paper presents a comparison of spectral characteristics of Landsat-8 and Sentinel-2 data for Arctic-Boreal regions in Siberia and shows the general compatibility of both sensor data in high latitudes. A set of coefficients for spectral bandpass adjustments were derived to modify the two image products to one another. This underlines the use of Landsat-8 and Sentinel-2 in combined time series analysis to increase data availability in northern high latitudes.

Alexandra Runge conceptualized the study design, processed, analyzed, and visualized the data, and wrote the original manuscript. Guido Grosse contributed to the study concept and the writing and editing of the manuscript and was responsible for funding acquisition and project administration. Field work data was not included in this study, but the participation of Alexandra Runge in the Lena Delta expedition to Samoylov station in 2018 helped create understanding for the Tundra ecosystem.

1.6.2 Chapter 3 - *Mosaicking Landsat and Sentinel-2 Data to Enhance LandTrendr Time Series Analysis in Northern High Latitude Permafrost Regions*

Authors: Alexandra Runge and Guido Grosse
Remote Sensing, 2020, 12(15), doi: 10.3390/rs12152471

This paper presents a method to combine Landsat and Sentinel-2 data in annual mosaics, to increase and obtain reliable spatial and temporal data coverage for time series analysis in northern high latitudes. For twelve sites across North Siberia, this paper demonstrates the increase in data availability and improvement of spatial coverage with Landsat+Sentinel-2 mosaics in permafrost regions.

Alexandra Runge conceptualized the study design, processed, analyzed, and visualized the data, and wrote the original manuscript. Guido Grosse contributed to the study concept and the writing and editing of the manuscript and was responsible for the resources, funding acquisition, and project administration.

1.6.3 Chapter 4 - *Remote Sensing Annual Dynamics of Rapid Permafrost Thaw Disturbances with LandTrendr*

Authors: Alexandra Runge, Ingmar Nitze and Guido Grosse

Remote Sensing of Environment, in review

This paper presents the adaptation of LandTrendr, an algorithm to detect disturbances from time series at high temporal resolution, to rapid permafrost disturbances. The method includes the combined use of Landsat and Sentinel-2 images and the full parametrisation workflow of LandTrendr to map and reliably depict the annual dynamics of retrogressive thaw slumps in North Siberia. This paper demonstrates a steady increase in retrogressive thaw slump affected area from 1999-2020 in North Siberia but also emphasises spatio-temporal variability of the thaw slump dynamics across five focus sites.

Alexandra Runge conceptualized the study design, processed, analyzed, and visualized the data, and wrote the original manuscript. Ingmar Nitze conducted a machine learning classification as part of the method. Guido Grosse contributed to the study concept and the writing and editing of the manuscript and was responsible for the resources, funding acquisition, and project administration.

2

Comparing Spectral Characteristics of Landsat-8 and Sentinel-2 Same-Day Data for Arctic-Boreal Regions

Alexandra Runge [1,2] and Guido Grosse [1,2]

[1] Alfred Wegener Institute for Polar and Marine Research, Telegrafenberg A 45, 14473 Potsdam, Germany
[2] University of Potsdam, Institute of Geosciences, Karl-Liebknecht-Str. 24-25, 14476 Potsdam-Golm, Germany

Published: 22 July 2019 in *Remote Sensing*, 11(14), doi: 10.3390/rs11141730

2.1 Abstract

The Arctic-Boreal regions experience strong changes of air temperature and precipitation regimes, which affect the thermal state of the permafrost. This results in widespread permafrost-thaw disturbances, some unfolding slowly and over long periods, others occurring rapidly and abruptly. Despite optical remote sensing offering a variety of techniques to assess and monitor landscape changes, a persistent cloud cover decreases the amount of usable images considerably. However, combining data from multiple platforms promises to increase the number of images drastically. We therefore assess the comparability of Landsat-8 and Sentinel-2 imagery and the possibility to use both Landsat and Sentinel-2 images together in time series analyses, achieving a temporally-dense data coverage in Arctic-Boreal regions. We determined overlapping same-day acquisitions of Landsat-8 and Sentinel-2 images for three representative study sites in Eastern Siberia. We then compared the Landsat-8 and Sentinel-2 pixel-pairs, downscaled to 60 m, of corresponding bands and derived the ordinary least squares regression for every band combination. The acquired coefficients were used

for spectral bandpass adjustment between the two sensors. The spectral band comparisons showed an overall good fit between Landsat-8 and Sentinel-2 images already. The ordinary least squares regression analyses underline the generally good spectral fit with intercept values between 0.0031 and 0.056 and slope values between 0.531 and 0.877. A spectral comparison after spectral bandpass adjustment of Sentinel-2 values to Landsat-8 shows a nearly perfect alignment between the same-day images. The spectral band adjustment succeeds in adjusting Sentinel-2 spectral values to Landsat-8 very well in Eastern Siberian Arctic-Boreal landscapes. After spectral adjustment, Landsat and Sentinel-2 data can be used to create temporally-dense time series and be applied to assess permafrost landscape changes in Eastern Siberia. Remaining differences between the sensors can be attributed to several factors including heterogeneous terrain, poor cloud and cloud shadow masking, and mixed pixels.

2.2 Introduction

The Arctic-Boreal domain is currently undergoing extensive environmental changes. Mean annual air temperatures increased by up to 1.5–2 °C over the 1960–2009 period (Serreze and Barry 2011), and precipitation increased, with climate models showing further precipitation increases with additional warming (Kaplan and New 2006). Both the increase in air temperatures and precipitation also affect the thermal state of permafrost, which is defined as ground that remains at or below a temperature of 0 °C for at least two consecutive years and is very widespread in this region (Brown et al. 1997). Considering that about a quarter of the Northern Hemisphere is underlain by permafrost, which is 65% of the land north of 60 degrees (Zhang et al. 2008), these changes are of great importance to northern high latitude ecosystems (Schuur and Mack 2018). Continued warming of permafrost across the pan-Arctic region (Biskaborn et al. 2019) ultimately will result in widespread permafrost thaw and eventually cause near-surface permafrost loss on local to regional scales (Chadburn et al. 2017). Thawing permafrost has direct implications for hydrological systems (Francis et al. 2009), ecosystems (Schuur and Mack 2018), soil carbon decomposition and accumulation (Hicks Pries et al. 2015), greenhouse gas emissions (Walter Anthony et al. 2018), and infrastructure stability in permafrost areas (Hjort et al. 2018). A multitude of landscape-scale changes, such as active layer deepening, thermokarst and talik formation, soil erosion, and changes in vegetation composition and surface hydrology can be linked to permafrost thaw (Grosse et al. 2016; Jorgenson et al. 2013; Romanovsky, Smith, and Christiansen 2010; Woo et al. 2008).

While permafrost itself cannot be observed directly with remote sensing, detectable surface disturbance can be linked to permafrost degradation. They can be distinguished between press and pulse disturbances, which are gradual and abrupt disturbance regimes respectively and alter the ecosystem and environment substantially (Collins et al. 2007). Press disturbances are driven by impacts and change factors unfolding over decades to centuries and occur gradually and continuously. Press disturbances include processes such as permafrost top-down thaw, as well as vegetation structure and composition changes. They usually occur on extensive

regional scales. In contrast to that, pulse disturbances unfold within very short time periods from a few days to years. They are usually extreme in nature and affect the system rapidly as one-time or episodic short-term events, but arise locally in distinct areas. Pulse disturbances include soil erosion, thermokarst lake expansion, lake drainage, and wildfires. Press and pulse disturbances interact with one another as well; for example, press disturbances can trigger pulse disturbances. Exemplary is permafrost top-down thaw initiating rapid thermokarst development or soil erosion (Grosse et al. 2011a; Jorgenson and Grosse 2016). To understand the complex feedbacks of permafrost degradation processes and resulting landscape and ecosystem dynamics in space and time, it is critical to track and quantify these not only at the field site scale, but at high spatial resolution across decadal time scales and extensive regions.

Remote sensing provides excellent tools to understand and quantify many of these dynamics linked to surface expressions and land cover changes associated with permafrost degradation across large regions (Stow et al. 2004; Bartsch et al. 2016; Jorgenson and Grosse 2016). For example, Nitze et al. (2018) mapped widespread permafrost disturbances based on trend analysis using linear regression on Landsat multispectral index time series, highlighting the abundance and distribution of disturbances such as thermokarst lake changes, wildfires, and thaw slumps. Similarly, Pastick et al. (2019) analyzed the diversity of landscape and ecosystem dynamics for Alaska using Landsat-based time series analysis in combination with spectral metrics, climatic data, and topographical and soil information. Using statistical models, they predicted and understood the drivers of change and differentiated between gradual and abrupt disturbances. Apart from understanding the spatial coverage, magnitude, patterns, and dimension of disturbances, the temporal dynamics of disturbances such as initiation timing, duration and persistence, recovery time, and recurrence frequency are highly important parameters for monitoring and projecting Arctic-Boreal ecosystem and landscape trajectories in a changing climate. Space-borne remote sensing with a high temporal and spatial resolution allows detailed monitoring of both gradual and abrupt changes, such as press and pulse disturbances, but requires more detailed insights into the timing and magnitudes of spectral changes of observation targets.

Algorithms developed for monitoring forest disturbances, such as LandTrendr, manage to identify both abrupt and gradual changes with temporally-dense Landsat time series (Kennedy, Yang, and Cohen 2010). Likewise, Sulla-Menashe et al. (2018) used Normalized Difference Vegetation Index (NDVI) Landsat time series for characterizing vegetation greening and browning patterns in Canadian boreal forests and identified the major driver of the signal to be vegetation recovery following disturbance. Implementing such algorithms developed for boreal ecosystems for extensive monitoring and assessing of disturbance types and dynamics, such as differentiating between press and pulse disturbances, across Arctic-Boreal permafrost regions will improve understanding of climate change and anthropogenic impacts in high latitudes on multiple temporal scales. Most of the schemes so far rely on the extensive Landsat record, which features the longest continuous data archive of optical Earth surface imagery, covering more than 45 years. However, the low temporal resolution of Landsat images and some environmental factors, such as a short growing season length, a challenging solar geometry,

frequent snow and ice cover, and especially persistent cloud cover, negatively affect the availability of images for detailed studies (USGS 2015; Hope and Stow 1996). Therefore, often, only a rather low number of adequate Landsat images are available for time series analyses in high latitudes. In many regions, these are not sufficient for creating temporally dense time series, which are needed for extracting detailed trends of disturbances and especially their short-term dynamics.

An approach to increase the data base in high latitudes is to combine Landsat time series, which relies on a single platform only, with images from additional optical sensors. A combined data base allows creating temporally much denser time series for the Arctic-Boreal domain, thereby increasing opportunities for monitoring permafrost region disturbances and ecosystem changes. The European Space Agency (ESA) Copernicus Sentinel-2 mission started in 2015 and consists of two satellites (S-2A, S-2B), which have a combined revisit time of five days (Drusch et al. 2012). Landsat-8 and Sentinel-2's sensors are both multispectral optical systems, have Sun-synchronous polar orbits, and obtain data with a comparable resolution. Both sensors record multispectral data with bands that cover similar wavelength ranges (Table 2.1). Sentinel-2 sensors' similar characteristics to Landsat and shortened revisit time are now leveraging the combined multispectral observation power of three platforms observing the Earth's surface at 10–30 m resolution, significantly increasing the chance for capturing cloud-free observations at high latitudes. Li and Roy (2017) quantified the combined revisit time of Landsat 8, Sentinel-2A, and Sentinel-2B, showing that the global average revisit interval was 2.9 days. With the increased poleward orbit overlap and the enhanced spatial overlap between acquisition swaths, the high latitudes (>70° N) feature the highest number of acquired images within a year (>400 images) and the shortest revisit interval (<1 day) (Li and Roy 2017). This dramatic increase in image numbers and shortened revisit time for a combined Landsat-8 and Sentinel-2 time series could facilitate tracking permafrost region disturbances in much higher detail.

Table 2.1: Corresponding Landsat-8 and Sentinel-2 bands and characteristics.

	Landsat-8			**Sentinel-2**		
	Band	**Wavelength (µm)**	**Resolution (m)**	**Band**	**Wavelength (µm)**	**Resolution (m)**
Coastal Aerosol	1	0.45–0.451	30	1	0.430–0.450	60
Blue	2	0.452–0.51	30	2	0.448–0.546	10
Green	3	0.533–0.590	30	3	0.538–0.583	10
Red	4	0.636–0.673	30	4	0.646–0.684	10
NIR	5	0.851–0.879	30	8A	0.848–0.881	20
NIR2				8	0.763–0.908	10
SWIR1	6	1.566–1.651	30	11	1.542–1.685	20
SWIR2	7	2.107–2.294	30	12	2.081–2.323	20
Cirrus	9	1.363–1.384	30	10	1.336–1.441	60

In terms of time series analyses, we do not just require cloud-free images, but rather depend on clear pixels for every location in one study area. A high number of clear pixels available in one observation period (summer months) indicates a good overall data coverage. Figure 2.1

shows the average number of clear pixels in the Lena Delta (see Section 3.3.1) for the summer months of every year. It becomes obvious that the average number of clear pixels for every location in the Lena Delta increases dramatically, when adding Sentinel-2 to the analysis. This underlines that relying not only on one sensor platform, but on multiple ones enhances the database drastically.

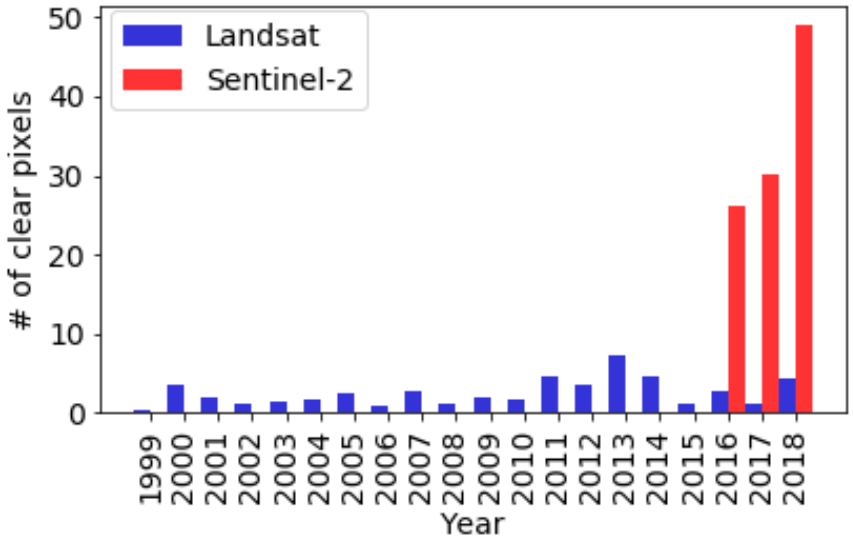

Figure 2.1: Average number of clear pixels for the study site Lena Delta for the summer periods covering 1999–2018 (blue bars: Landsat; red bars: Sentinel-2).

For a combined time series, it is necessary to align the image products of the different sensors geometrically and radiometrically, ensuring that the same point on the ground is captured with similar spectral reflectance properties in both products. This issue was already addressed for the Landsat sensor series, defining adjustment schemes for slight differences in reflectance measurements, ensuring data continuity and that the Landsat image products from the different sensors (Landsat-5 TM, Landsat-7 ETM+, and Landsat-8 OLI) can be used in a combined time series analysis (Flood 2014; Mishra et al. 2014; Teillet et al. 2001; Teillet, Markham, and Irish 2006). To extend the data continuity incentive beyond the Landsat sensors and also to be able to include Sentinel-2, previous studies compared Landsat-8 with Sentinel-2 data and defined bandpass adjustments between corresponding Landsat-8 and Sentinel-2 bands for a better fit. Despite similar wavelength ranges covered by the corresponding bands, the spectral response functions per sensor differ, and this impact has to be assessed before a combined time series is applied (Zhang et al. 2018). Previous comparison studies varied in application region, scale, input datasets, ranging from simulated to acquired image products, and covered temporally close to same-day acquisitions (Mandanici and Bitelli 2016; Vuolo et al. 2016; Gorroño et al. 2017; Zhang et al. 2018; Li et al. 2017). Regardless of these differences, the comparison approaches are always alike, examining corresponding Landsat-8 and Sentinel-2 bands, comparing pixel-pairs, and deriving regression equations for bandpass alignments. Claverie et al. (2018) conducted a comparison between Landsat-8 and Sentinel-2 data for 91 test sites worldwide and created a globally-applicable Harmonized Landsat and Sentinel-2 surface reflectance dataset (HLS). While a few sample sites are situated in Alaska, Canada,

and Northern Scandinavia, sites from the Siberian high latitudes are not included. Flood (2017) was first to compare same-day Landsat-8 with Sentinel-2 acquisition pixel-pairs of corresponding bands for Australia and defined band-wise adjustment equations. Furthermore, Flood (2017) applied the global HLS bandpass correction to the same dataset, but concluded that the HLS adjustment did not sufficiently adjust the Sentinel-2 data to Landsat-8 data. As a consequence, their region-specific derived bandpass adjustments showed a better fit than the HLS adjustment. An overall result of the previous studies was that Landsat-8 and Sentinel-2 data were comparable, but for a combined analysis, the datasets have to be adjusted to avoid detecting change because of a bias between sensors and not because of changes on the ground, which is particularly important for studying trends. Despite the effort of creating a globally-applicable harmonized product (Claverie et al. 2018), local to regional studies showed that locally-derived bandpass adjustments are superior to the HLS product (Flood 2017; Mandanici and Bitelli 2016). Therefore, it is recommendable to create region-specific adjustments between Landsat-8 and Sentinel-2 for regional assessments and applications.

So far, to the best of our knowledge, no comparison of Landsat-8 and Sentinel-2 data or an assessment of a potential combined use in time series analyses for the Siberian Arctic-Boreal region has been done. The overall objective of this paper is to compare the spectral characteristics of Landsat-8 and Sentinel-2 data across different types of landscapes and ecosystems in the study domain and assess their compatibility in Arctic-Boreal permafrost regions for the potential use in combined time series. To address this objective, we focus on three sub-objectives: (1) comparison of the spectral characteristics of corresponding bands from Landsat-8 and Sentinel-2 data of same-day acquisitions for three individual study sites in Eastern Siberia that broadly differ in ecosystem and land cover characteristics; (2) defining spectral band adjustments between Landsat-8 and Sentinel-2 data for each of the three study sites; and (3) determining a set of spectral band adjustments that is applicable to Eastern Siberia generally and comparing them to the application of the global Harmonized Landsat Sentinel-2 product.

2.3 Materials and Methods

2.3.1 Study Sites

For this assessment, we included three study sites that are representative for the range of land cover conditions in Eastern Siberia: the arctic central Lena Delta (73° N, 126° E), the mountainous Batagay region in the Yana Highlands (67° N, 134° E), and the boreal Maya-Yakutsk region in central Yakutia (62° N, 129° E). The three sites are located along an approximate north-south transect and exemplify the different climatic, geologic, geomorphologic, and vegetational conditions of the quite heterogeneous Eastern Siberian permafrost landscapes, bridging from arctic to boreal regions and covering both tundra and taiga biomes (Figure 2.2).

The Lena Delta has a maritime-influenced polar tundra climate and is located in Northern Siberia at the Laptev Sea coast, within the continuous permafrost zone. It is the biggest

Arctic delta with about 29,000 km^2. The land cover in the delta is dominated by Arctic tundra that varies in vegetation composition between three major geomorphological terraces (Schneider, Grosse, and Wagner 2009). We here focused on the central part of the delta where the Arctic research station Samoylov is located (Boike et al. 2013). Samoylov Island is one of the 1500 delta islands and part of the first river terrace. The first terrace formed during the Holocene and is characterized by low-center ice-wedge polygonal tundra, polygonal ponds, large thermokarst lakes, and active flood plains (Boike et al. 2013). Wet and moist tundra dominates this area with a vegetation cover of sedge, grass, moss, and dwarf shrub wetlands (Schneider, Grosse, and Wagner 2009). The study area extends further to the adjacent Kurungnakh Island, which is part of the third terrace, an old late Pleistocene accumulation plain dissected by delta channel formation and thermokarst processes and characterized by polygonal microrelief and thermokarst ponds and lakes (Morgenstern et al. 2011; Strauss et al. 2017a). The second terrace of the Lena Delta consisting of late Pleistocene fluvial deposits is restricted to the northwestern part of the Lena Delta and is therefore not represented in the study area. From 1999–2011, the mean annual air temperature of the central Lena Delta was −12.5 °C with a mean temperature range from 10.1 °C–−33.1 °C in July and February, respectively. In the same period summer, precipitation ranged from 52 mm (2001) to 199 mm (2003) (Boike et al. 2013).

The Batagay study area represents a highly continental region with strong seasonal air temperature ranges and an overall low mean annual precipitation (Ashastina et al. 2017; Lydolph, Temple, and Temple 1985). Batagay is located at the Yana River and in between the Verhoyansk and Chersky Ranges in the Yansk Uplands, a region that features the cold pole of the Northern Hemisphere and is underlain by continuous permafrost with shallow active layer depths from 0.2–1.2 m (Ivanova 2003). The mean air temperature in July is 15.5 °C and in January −44.7 °C, while the mean annual precipitation is only 181 mm (Ivanova 2003; Lydolph, Temple, and Temple 1985). The land cover in this study area is dominated by light coniferous forests with larch (*Larix gmelinii*), Siberian dwarf pine (*Pinus pumila*), and a dense shrub layer. A thick layer of lichens and mosses covers the mostly wet ground (Ashastina et al. 2017). Other portions of the study area consist of barren bedrock surfaces. Ashastina et al. (2017) described the bedrock geology as a mix of dark grey siltstone and mudstone that contain layers of sand and clay deposits based on maps and Kunitsky et al. (2013). The Batagay megaslump, the largest known retrogressive thaw slump with a total area of >70 ha and headwall retreat rates of up to 30 m per year in 2016 (Günther et al. 2016), is located within this study area at about 67° N, 134° E (Opel et al. 2018). This large thaw landform indicates the presence of vulnerable ice-rich permafrost as a thick cover deposit in some parts of this region.

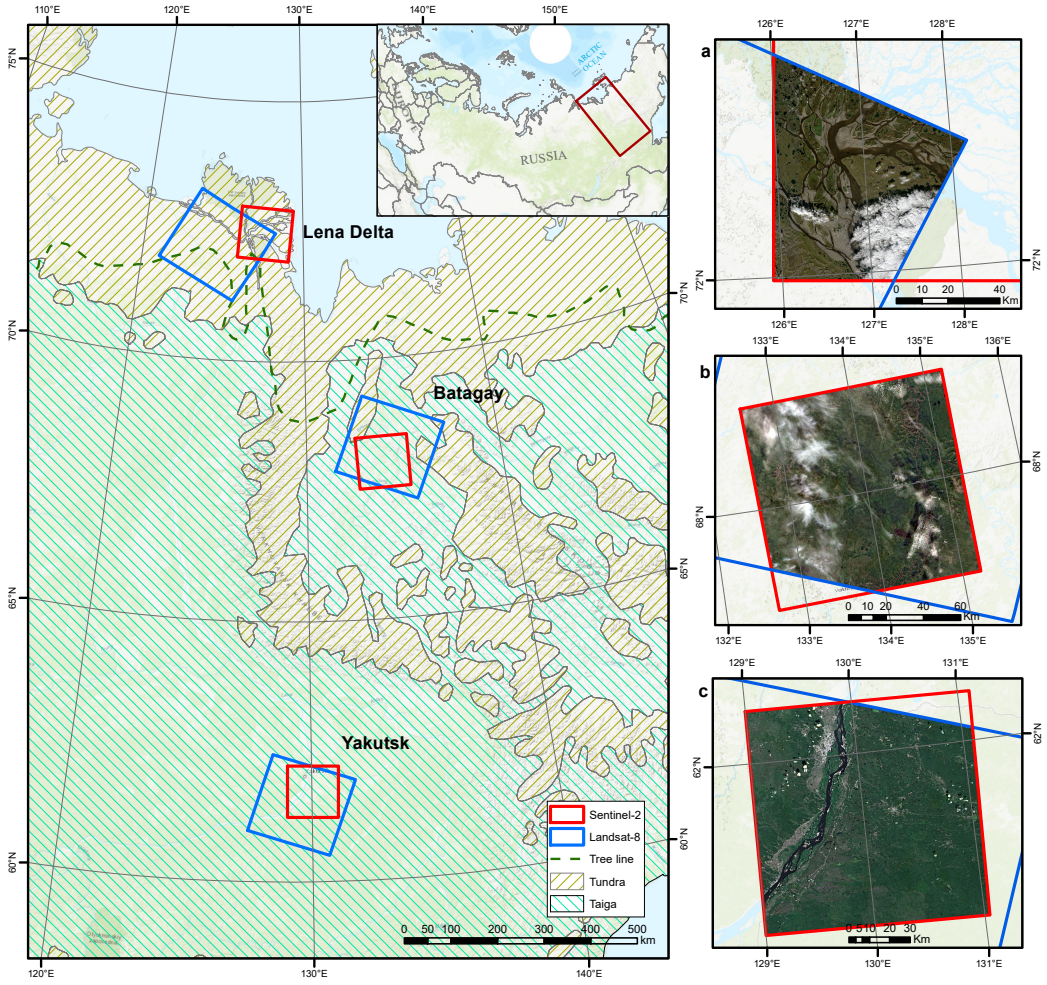

Figure 2.2: The three Arctic-to-Boreal study sites, Lena Delta, Batagay region, and Yakutsk region, are located along an approximate north-south transect in Eastern Siberia. The blue frames show the Landsat-8 image footprint, and the red frames show the Sentinel-2 image footprint of the same-day acquisitions used in this study. Sentinel-2 RGB composites of the overlapping area for the Lena Delta (**a**), Batagay region (**b**), and Yakutsk region (**c**).

The Yakutsk study area in central Yakutia has an extremely continental climate with a mean annual air temperature of −10.2 °C, mean January temperatures of −42.6 °C, July temperatures of 18.7 °C, and an annual precipitation of about 234 mm (Fedorov et al. 2014). The region is dominated by boreal summer green needle forests, mainly by *Larix* (Fedorov et al. 2017). Ice-rich late Pleistocene permafrost, as well as vegetated dune fields are widespread on the Lena river terraces. Silty clays, sandy silts, and silty sands dominate the Quaternary sediments. Thermokarst lakes and basins dominated by meadow vegetation (alases) are abundant (Fedorov et al. 2014; Ulrich et al. 2017). Intensive thermokarst development in the area can reach surface subsidence rates of 5–10 cm per year, and thermokarst lakes more than doubled their area during the 1992–2012 period (Fedorov et al. 2014). The region is also regularly affected by forest fires (Boike et al. 2016), resulting in a heterogeneous land cover with different disturbance and succession stages of the vegetation.

2.3.2 Data

In our study, we focused on imagery from Landsat-8 and Sentinel-2. The USGS Landsat-8 satellite was launched in 2013 and is equipped with the Operational Land Imager (OLI) sensor, which is a multi-spectral imager. The satellite has a 16-day repeat cycle, orbiting Sun-synchronously at 705 km altitude. The sensor field of view is 15 degrees, which results in a 185-km swath width. The satellite is also equipped with a co-registered Thermal Infrared Sensor (TIRS) that contains two thermal spectral bands with a ground spatial resolution of 100 m. The nine spectral bands of the OLI sensor have a spatial resolution of 30 m. The Landsat-8 OLI continues the Landsat mission that originally started in 1972 (USGS 2015). The ESA Copernicus Sentinel-2A and 2B satellites were launched in 2015 and 2017, respectively, and have the Multi-Spectral Instrument (MSI) aboard, which is also a multi-spectral imager, orbiting at a 786-km altitude Sun-synchronously. The increased orbit altitude together with a field of view of 20.6 degrees results in a swath width of about 290 km. Both Sentinel-2 satellites have a repeat cycle of 10 days, but as they operate out of phase, they have a joint revisit time of five days. The 13 spectral bands of the MSI have different spatial resolutions, 10 m, 20 m, and 60 m (Table 2.1) (Drusch et al. 2012; ESA 2015).

We accessed and processed both Landsat-8 and Sentinel-2 imagery predominantly on the Google Earth Engine (GEE) platform. GEE is a cloud-based platform that incorporates analysis-ready data catalogs allowing the user to access and analyze data easily. GEE hosts the entire multi-petabyte Landsat archive, as well as data from Sentinel-2 (Gorelick et al. 2017). The images are ingested and cut into tiles for efficient collection handling in GEE, but remain stored with their original projection, resolution, and bit depth. For this study, we used the "USGS Landsat 8 Surface Reflectance Tier 1" image collection. The images in this collection are atmospherically corrected to surface reflectance based on the Landsat 8 Surface Reflectance Code (LaSRC) and already contain a mask for clouds, shadows, waters, and snow, derived from the CFMASK algorithm (USGS 2018; Foga et al. 2017). For Sentinel-2, we accessed the image products in two ways. First, we selected the "Sentinel-2 MSI: Multi-Spectral Instrument, Level-1C" image collection in GEE, containing Top-Of-Atmosphere (TOA) reflectance images, the only full Sentinel-2 collection provided in GEE at the time. The datasets contain the QA60 band that includes cloud mask information as pre-processed by ESA (ESA 2015). We used the GEE Sentinel-2 collection for preparing the filtering and masking step (Step A) as described in Section 2.3.3.1 and Figure 4.2. Based on the GEE filtering results, we downloaded the Sentinel-2 Level-1C images from the ESA Copernicus Open Access Hub to process them to surface reflectance data with ESAs' Sen2Cor atmospheric correction processor that corrects Sentinel-2 Level-1C orthophoto products to Level-2A surface reflectance products (see Section 2.3.3.3) (Louis et al. 2016; Müller-Wilm, Devignot, and Pessiot 2016). After processing, we ingested the atmospherically-corrected Sentinel-2 Level-2A images into GEE to continue with Step C of the workflow (Figure 4.2).

2.3.3 Data Processing

The data processing workflow consisted of three steps (Figure 4.2). In Step A, we filtered and cloud-masked the imagery. In Step B, we processed Sentinel-2 surface reflectance images with the Sentinel Application Platform. In Step C, we masked the Landsat-8 and Sentinel-2 images to prepare the pixel-by-pixel data input for the spectral comparison and adjustment.

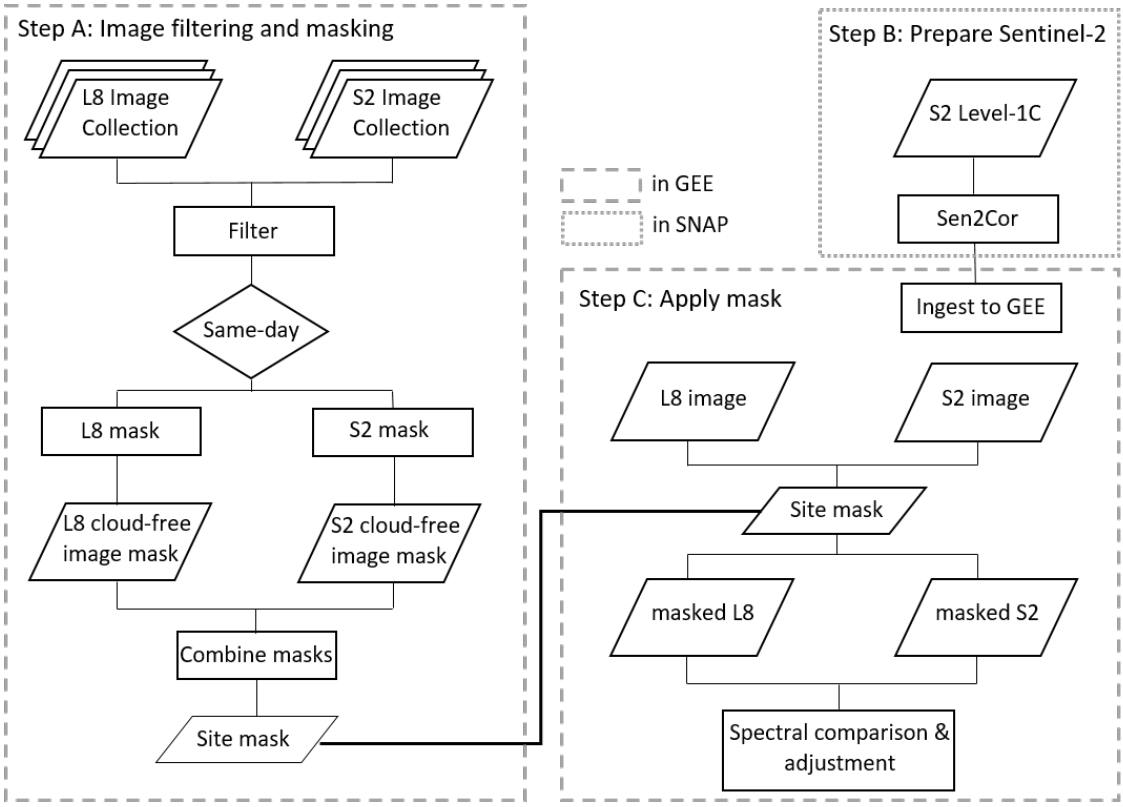

Figure 2.3: Data processing workflow used for the spectral band comparison and adjustment. Landsat-8 is abbreviated to L8 and Sentinel-2 to S2.

2.3.3.1 Filtering Image Collections

For each study area (Lena Delta, Batagay, and Yakutsk), we filtered the Landsat-8 and Sentinel-2 GEE image collections based on location, date range, and maximum cloud coverage. We filtered the collections for the Arctic summer months (1 July–31 August 2016) and a maximum cloud cover of 80% per image. We then identified same-day acquisitions of overlapping Landsat-8 and Sentinel-2 images for each study site (Figure 2.2, Table 2.2, and Table 2.7 with the GEE image names). For each study site, we identified one Landsat-8 and one Sentinel-2 image that overlapped substantially and had as little cloud cover as possible. We assumed that there was no change on the ground target between the Landsat-8 and Sentinel-2 identified same-day observations since both satellites are Sun-synchronous with mid-morning overpass times, the same-day acquisitions being taken only minutes apart. Likewise, atmospheric conditions were also expected to not have changed significantly between the acquisitions. Additionally, the solar zenith and solar azimuth angles were very similar and only diverged slightly (Table 2.2). Therefore, any differences found between the Landsat-8 and Sentinel-2 same-day acquisitions were considered differences in sensor responses exclusively.

Table 2.2: Data filtering and selection result for same-day Landsat-8 and Sentinel-2 image pairs for the three study sites.

	Location	Date 2016	Sensor	Cloud cover %	Acquisition time (UTC)	Solar azimuth angle	Solar zenith angle	No. of clear pixels
Lena	72.37 N	23 August	L8	24	03:40:06	178.97	60.89	156,315
Delta	126.50 E		S2	18.5	03:47:34	184.34	61.18	
Batagay	67.77 N	1 August	L8	38.6	02:39:23	170.97	50:57	346,053
	134.58 E		S2	49.8	03:05:46	179.39	50.10	
Yakutsk	61.77 N	9 July	L8	1.3	02:35:06	161.32	40.17	1,944,414
	130.50 E		S2	0.1	03:00:11	171.07	39.65	

2.3.3.2 Creating L8, S2, and Site Masks

Our method was solely based on a clear pixel comparison. In this case, we defined clear pixels not to contain clouds, cloud shadows, water, or snow, and hence, their surface reflectance values were uncontaminated by these environmental properties. The masking of clouds, cloud shadows, and snow was done in GEE. For Landsat-8, we used the provided "pixel_qa" band that contains cloud, shadow, snow, and water masks derived with the CFMask algorithm (Foga et al. 2017). Based on the CFMask information in the "pixel_qa" band, we selected clear pixels only and created a "clear pixel" mask for each Landsat-8 image of the three study sites (L8 mask). For Sentinel-2, we applied a simple cloud score algorithm that uses band thresholds as cloud filtering steps (ESA 2015). We also included a cloud shadow shift algorithm taking into account the average cloud height and projecting the estimated cloud shadow based on the cloud position, a GEE code fragment introduced by Donchyts (Donchyts 2017). With this method, we also created a mask for each Sentinel-2 image that selects only clear pixels of that image, creating a "clear pixel" mask (S2 mask).

To identify clear pixels in both datasets, we joined the two masks. First, we reprojected both L8 and S2 clear pixel masks (L8 masks and S2 masks) to the same projection, taking the Landsat-8 image projection as the default projection (WGS 84/ UTM zone 51 N, 52 N, or 53 N for the different study sites). Additionally, we resampled the S2 masks to 30-m spatial resolution to fit to the Landsat-8 resolution. GEE offers a resampling algorithm for images called "reproject". This algorithm requires two input parameters and then performs nearest neighbor resampling. Firstly, one needs to specify the projection to be used and secondly the desired scale or better spatial resolution in meters of the output image. Then, the L8 mask and S2 mask (30 m) for each image pair per study site were combined. The result was a single mask that contained only overlapping clear pixels from the Landsat-8 and Sentinel-2 same-day acquisitions for every study site ("site mask").

2.3.3.3 Preparing Sentinel-2 Surface Reflectance Images in SNAP

We downloaded the same-day Sentinel-2 Level-1C images from ESA's distribution platform Copernicus Open Access Hub. The images were processed in SNAP to Sentinel-2 Level-2A surface reflectance images with the Sen2Cor tool. Sen2Cor can be run from the Sentinel

Application Platform (SNAP) desktop toolbox. We used SNAP Version 6.0.5 including the Sentinel-2 Toolbox (S2TBX) Version 6.0.2 with Sen2Cor Version 255. The input for the Sen2Cor tool is the Sentinel-2 Level-1C image and processing parameters. We defined the processing resolution to 10 m, the aerosol input for the Lena Delta as "Maritime" and for Batagay and Yakutsk as "Rural", and the type of atmosphere as "mid-latitude summer", and the remaining parameters were kept as default. The results were Sentinel-2 Level-2A image products, corrected to surface reflectance. After exporting the images as Geotiffs from SNAP, we ingested them into GEE.

2.3.3.4 Applying Site Masks

The final processing step included the surface reflectance image products. For the L8, we again relied on the image collection "USGS Landsat 8 Surface Reflectance Tier 1" available in GEE. For S2, we used the SNAP-processed Sentinel-2 Level 2A images newly ingested into GEE. To avoid errors due to georeferencing differences, we reprojected the same-day surface reflectance images to the same projection, as described in Section 2.3.3.2, and resampled the images uniformly to 60-m spatial resolution with an averaging algorithm. The resampling ensured that the Landsat-8 and Sentinel-2 pixel-pairs covered the same ground target (Korhonen, Packalen, Rautiainen, et al. 2017), in addition to their already good relative co-registration of <6.6 m (Storey, Choate, and Lee 2014). Even residual geolocation errors of Landsat-8, which can lead to geographic misalignments between Landsat-8 and Sentinel-2 of up to 38 m, were then reduced (Storey et al. 2016). The overall mask per study site ("site mask") was also resampled to 60 m and then applied to the Landsat-8 and Sentinel-2 surface reflectance (60 m) images. The resulting masked images were now clipped to the site masks' extent and only contained the corresponding Landsat-8 and Sentinel-2 cloud-free pixels of the same-day acquisitions per study site. The obtained Landsat-8 and Sentinel-2 surface reflectance pixel-pair dataset from the same-day acquisitions was then used as the input for the spectral band comparison and adjustment.

Both the cloud and especially cloud shadow masking were not very reliable, neither for the Landsat-8, nor for the Sentinel-2 images (Foga et al. 2017; Zhu, Wang, and Woodcock 2015). This particularly affected the Batagay and Yakutsk sites. Therefore, we additionally had to identify manually cloud- and cloud shadow-free overlapping image regions of the same-day image pairs and select only these areas for the data output to ensure an appropriately clear dataset. We exported these pixel-pair datasets from GEE as csv-files to continue with the analyses in Jupyter Notebook (Python).

2.3.4 Spectral Band Comparison and Adjustment

We compared the Sentinel-2 pixel surface reflectance values of the individual bands to the corresponding pixel surface reflectance values of the matching Landsat-8 bands (Table 2.1) and used scatter plots to display the relationship of the pixel-pairs of corresponding bands. A 1-to-1 line in every plot represents the potential perfect agreement between the two bands and allows a

first visual assessment of misalignment between the two sensors. The divergence of the variables from the 1-to-1 line displays the error between the two corresponding bands. We further calculated the Pearson correlation coefficient (r) as a measure of linear correlation between the corresponding band pairs per study site. A correlation coefficient of 1.0 shows perfect correlation between two variables and a coefficient of 0.0 that there is no linear relationship (Cowan 1998). Additionally, we derived the Root Mean Squared Error (RMSE), which is a measure of the absolute difference between the value pairs. The lower the RMSE, the smaller the difference of the x and y value, hence a closer relationship (Cowan 1998). Most importantly, we derived the ordinary least squares regression for every band comparison. The resulting prediction fit model can be generally described as in Equation (2.1).

$$L8 = slope * S2 + intercept \tag{2.1}$$

where S2 stands for the surface reflectance values of the Sentinel-2 MSI bands, L8 for the surface reflectance values of the Landsat-8 OLI bands, and slope and intercept the coefficients derived in the ordinary least squares regression. A slope of 1 and an intercept of 0 would indicate a perfect fit between L8 and S2.

We applied the explicit slope and intercept values per band of the derived ordinary least squares regression model to the Sentinel-2 MSI reflectance values. Hence, we calculated adjusted Sentinel-2 reflectance values that resembled the Landsat-8 values and reduced potential errors between Landsat-8 and Sentinel-2 reflectance values per band. This analysis and adjustment was conducted for every corresponding Sentinel-2 and Landsat-8 band pair and every study site individually.

In addition to the local assessment of the individual study sites, we aimed for a more regional approach. We combined all pixel pairs of the three study sites, Lena Delta, Batagay, and Yakutsk, as they represent the heterogeneity of Eastern Siberia (ES), and conducted the spectral band comparison for ES as a whole as well. We applied the resulting ES ordinary least squares regression model to all three study sites to assess the potential differences between locally- and regionally-derived adjustment coefficients and discussed whether a spectral comparison and adjustment were possible on the regional scale. Likewise, we also applied the globally-derived ordinary least squares regression coefficients from the Harmonized Landsat Sentinel-2 product (HLS) (Claverie et al. 2018) to all three study sites individually to assess the potential use of the globally applicable product versus the locally-derived adjustment. The HLS adjustment coefficients were taken from (Claverie et al. 2018).

As vegetation indices are extensively used for qualitative and quantitative vegetation cover analyses from spectral measurements, we extended the adjustment assessment to the Normalized Difference Vegetation Index (NDVI). We derived the NDVI, which is commonly used as an indicator of green vegetation cover, for both the Landsat-8 and Sentinel-2 data products. The NDVI is calculated by using two spectral bands, as shown in Equation (2.2)

$$NDVI = \frac{NIR - Red}{NIR + Red} \tag{2.2}$$

where NIR stands for the Near-Infrared wavelength band values and Red for the red wavelength band values of the individual sensor (Bannari et al. 1995). The NDVI can range between -1 and 1, where an NDVI close to 1 indicates high green vegetation cover and a value close to 0 no vegetation, possibly urban areas, and negative NDVI values mainly result from water, clouds or snow. For the Landsat-8 NDVI calculation, we used B5 for NIR and B4 for red, and for the Sentinel-2 NDVI calculation, we used B8A for NIR and B4 for red (Table 2.1). We calculated the NDVI for the measured surface reflectance Landsat-8 and Sentinel-2 values and also for the spectrally-adjusted Sentinel-2 reflectance values to assess what effect the spectral differences of Landsat-8 and Sentinel-2 might have on vegetation indices.

2.4 Results

2.4.1 Spectral Band Comparison

The spectral band comparisons were conducted for all pixels of the overlapping areas from the same-day Sentinel-2 and Landsat-8 acquisitions for every corresponding band combination and for all study sites. Table 2.3 summarizes the analysis for each study area and provides the intercept and slope of the resulting ordinary least squares regression, Pearson's correlation coefficients, and associated root mean squared errors. Exemplarily, Figure 2.4 shows the scatter plots of band combinations and adjusted Sentinel-2 data for the Lena Delta. Figure 2.4 depicts the expected offset between corresponding bands and scatter around the one-to-one line. In general, the scatter plots affirm that the Landsat-8 and Sentinel-2 bands have a strong overall correlation. This is also represented by high r coefficients and promising ordinary least squares regression coefficients as low intercept and high slope values (Table 2.3). The comparison scatter plots of Batagay, Yakutsk, and Eastern Siberia are provided in the Appendix (Figures 2.6–2.8).

The band comparisons of the visible wavelength bands, B2/B2, B3/B3, and B4/B4 for Batagay (Figure 2.6), showed noticeably lower correlation coefficients, 0.624, 0.726, and 0.818, respectively. The slope coefficients from the ordinary least squares regression were lower for these band combinations in Batagay as well, compared to the other two study sites and the regional ES assessment (Table 2.3).

We compared both possible NIR band combinations, B8A/B5 and B8/B5, to inspect if one Sentinel-2 NIR band, B8A or B8, was more similar and fits spectrally better to the Landsat-8 NIR band (B5) in combined studies in Eastern Siberia. The results showed no striking trend favoring one band combination. The B8A/B5 comparison overall had slightly higher correlation coefficients than the B8/B5 comparison. Likewise, the RMSE was also smaller for B8A/B5, indicating a closer fit between Sentinel-2 B8A and Landsat-8 B5 reflectance values. The ordinary least squares regression analyses showed contrasting trends, however. The B8A/B5 band comparisons resulted in intercepts that were slightly lower and therefore indicated a marginally better fit. In contrast, the B8/B5 comparison yielded higher slopes,

which suggested a regression fit of the two variables.

Table 2.3: Comparison of surface reflectance values from the Sentinel-2 and Landsat-8 corresponding bands, for same-day acquisitions. Displaying the results of the ordinary least squares regression, Pearson correlation, and root mean squared error for every study site.

Bands		Study	Ordinary Least Squares Regression		Pearson's Correlation	Root Mean Square
S2 Band	**L8 Band**	**Site**	**Intercept**	**Slope**	**Coefficient (r)**	**Error (RMSE)**
2	2	Lena Delta	0.017	0.66	0.927	0.012
		Batagay	0.0107	0.531	0.624	0.008
		Yakutsk	0.0052	0.689	0.92	0.007
		ES	0.0053	0.711	0.89	0.0073
3	3	Lena Delta	0.0186	0.767	0.962	0.0096
		Batagay	0.0240	0.599	0.726	0.008
		Yakutsk	0.0129	0.752	0.945	0.006
		ES	0.0125	0.777	0.937	0.0065
4	4	Lena Delta	0.0182	0.784	0.97	0.0104
		Batagay	0.018	0.721	0.818	0.011
		Yakutsk	0.012	0.8	0.964	0.009
		ES	0.0125	0.815	0.97	0.0095
8A	5	Lena Delta	0.0302	0.835	0.95	0.021
		Batagay	0.056	0.749	0.902	0.019
		Yakutsk	0.044	0.806	0.945	0.018
		ES	0.044	0.804	0.941	0.019
8	5	Lena Delta	0.030	0.869	0.943	0.0187
		Batagay	0.058	0.771	0.900	0.020
		Yakutsk	0.049	0.82	0.942	0.0201
		ES	0.049	0.82	0.94	0.020
11	6	Lena Delta	0.021	0.826	0.951	0.0241
		Batagay	0.0194	0.836	0.933	0.015
		Yakutsk	0.0095	0.894	0.967	0.014
		ES	0.012	0.877	0.97	0.015
12	7	Lena Delta	0.007	0.852	0.962	0.019
		Batagay	0.0077	0.834	0.938	0.0111
		Yakutsk	0.0031	0.874	0.974	0.012
		ES	0.004	0.87	0.974	0.013

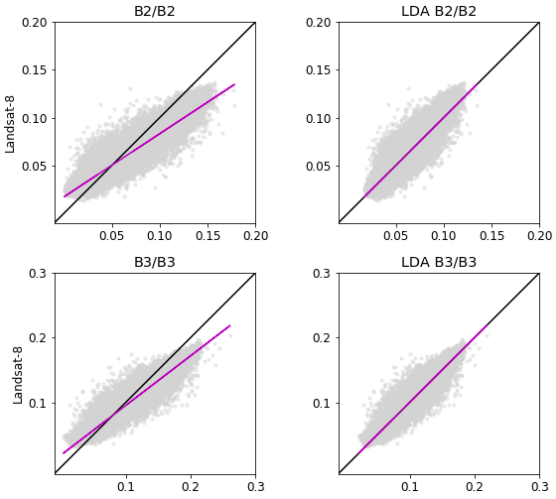

Figure 2.4: Cont.

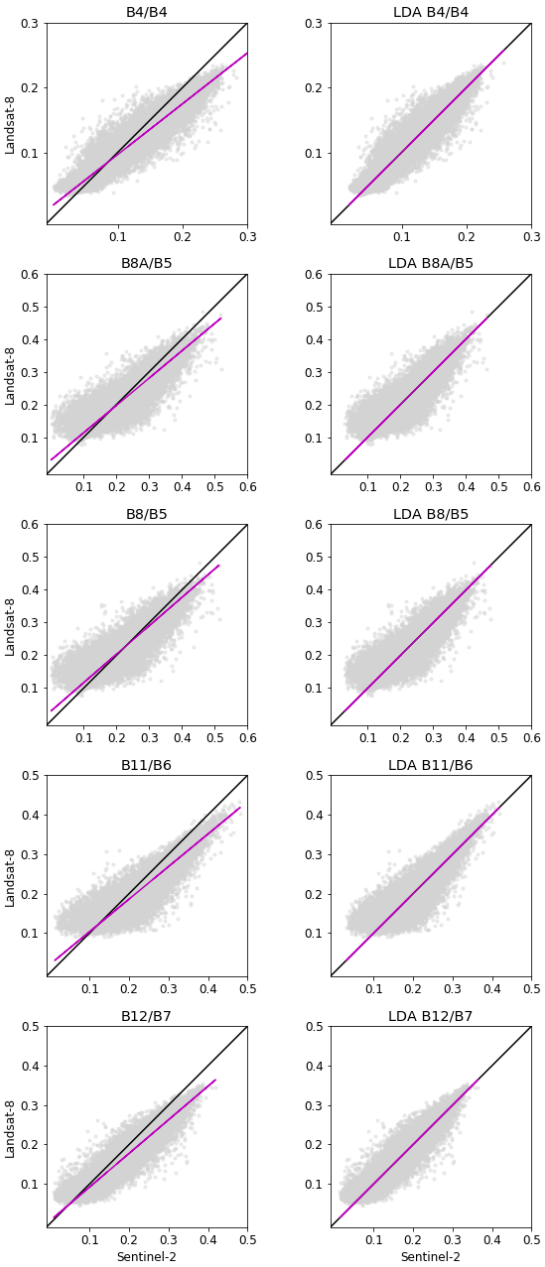

Figure 2.4: Comparison of surface reflectance values from the Sentinel-2 and Landsat-8 corresponding bands for the Lena Delta. Left plots: observed surface reflectance values. Right plots: Lena Delta Adjusted (LDA) Sentinel-2 reflectance values. The solid black line is one-to-one, and the pink line is the ordinary least squares regression trend line. In all plots, the Sentinel-2 values and bands are on the x-axis, while Landsat-8 is depicted on the y-axis.

Overall, the study sites did not differ from one another significantly. The r coefficients ranged between 0.89 (ES B2/B2) and 0.974 (Yakutsk and ES B12/B7), which points at very strong correlations between the Sentinel-2 and Landsat-8 surface reflectance values for all assessed corresponding bands at all study sites. Furthermore, the ordinary least squares regression analyses mainly showed very low intercept and reasonably high slope values.

2.4.2 Spectral Band Adjustment

The ordinary least squares regression results (Table 2.3) were used as the input for the spectral band adjustment, using Equation (2.1). With these coefficients, we adjusted the observed

Sentinel-2 surface reflectance values to fit the Landsat-8 values with respect to the band combination and specific study sites. The adjusted Sentinel-2 results are shown exemplarily for the Lena Delta site in Figure 2.4, while the other two sites, as well as the overall adjustment for Eastern Siberia are shown in the Appendix (Figures 2.6–2.8).

The overall results showed that the Sentinel-2 surface reflectance values can be fitted to the Landsat-8 pixel surface reflectance values (Table 2.4). After the spectral band adjustment by band pair, we recalculated the r coefficient, RMSE, and also the new ordinary least squares regression. Visually, the adjusted Sentinel-2 and Landsat-8 surface reflectance values were well aligned with the one-to-one line (Figure 2.4, Figure 2.6, Figure 2.7, and Figure 2.8). The new intercept and slope results of the ordinary least squares regression now showed that the adjusted datasets had no offset (0) and a slope that was either 0.99 or 1.0, indicating a very good agreement between the two variables. The spread around the mean, demonstrated by the r coefficient, was unchanged, but the RMSE decreased for all band combinations in all study sites. This indicates that the absolute difference between the adjusted Sentinel-2 and Landsat-8 reflectance values for corresponding pixels declined overall. Our results showed that the individual bands correlated better after the Sentinel-2 adjustment for all three study sites and also the Eastern Siberian (ES) regional scale analysis.

Table 2.4: Comparison of surface reflectance values from the Sentinel-2 and Landsat-8 corresponding bands after spectral band adjustment, for same-day acquisitions. Displaying the results of the ordinary least squares regression, Pearson correlation, and root mean squared error for every study site.

Bands		Study	Ordinary Least Square Regression		Pearson's Correlation	Root Mean Square
S2 Band	L8 Band	Site	Intercept	Slope	Coefficient (r)	Error (RMSE)
2	2	Lena Delta	0	0.99	0.927	0.007
		Batagay	0	1.00	0.624	0.006
		Yakutsk	0	0.99	0.92	0.004
		ES	0	1.00	0.89	0.005
3	3	Lena Delta	0	0.99	0.962	0.006
		Batagay	0	1.00	0.726	0.006
		Yakutsk	0	1.00	0.945	0.0042
		ES	0	1.00	0.937	0.005
4	4	Lena Delta	0	0.99	0.97	0.007
		Batagay	0	0.99	0.818	0.006
		Yakutsk	0	0.99	0.964	0.0048
		ES	0	1.00	0.97	0.0054
8A	5	Lena Delta	0	1.00	0.95	0.016
		Batagay	0	0.99	0.902	0.0153
		Yakutsk	0	0.99	0.945	0.0152
		ES	0	1.00	0.941	0.0154
8	5	Lena Delta	0	1.00	0.943	0.017
		Batagay	0	0.99	0.900	0.0154
		Yakutsk	0	0.99	0.942	0.0155
		ES	0	0.99	0.94	0.0158
11	6	Lena Delta	0	0.99	0.951	0.013
		Batagay	0	1.00	0.933	0.0112
		Yakutsk	0	1.00	0.967	0.0102
		ES	0	1.00	0.97	0.0106
12	7	Lena Delta	0	0.99	0.962	0.011
		Batagay	0	1.00	0.938	0.0075
		Yakutsk	0	0.99	0.974	0.0074
		ES	0	0.99	0.974	0.0077

The comparison of the NDVI calculations showed one distinct feature. Negative Landsat-8 NDVI values were found only for few pixels, whereas for Sentinel-2 NDVI values before the adjustment, there were considerably more negative values, especially in Yakutsk. However, after spectral band adjustment, there were hardly any remaining negative Sentinel-2 NDVI values. This was valid for all study sites (Figures 2.5 and 2.9). Negative NDVI values normally indicate non-vegetated land cover types such as snow, clouds, or water with their higher reflectance properties in the visible wavelengths and then a reflectance decline towards near infrared. Despite this, the NDVI comparisons depicted overall a good fit between Landsat-8 NDVI and Sentinel-2 NDVI values for all study sites, with r coefficients ranging from 0.85 (Batagay) to 0.98 (Lena Delta) (Table 2.5). The ordinary least squares regression coefficients, as well as the r and RMSE improved with the Sentinel-2 spectral band adjustment when recalculating the Sentinel-2 NDVI with the adjusted NIR and red values (Figure 2.5 and Table 2.5).

Table 2.5: Comparison of NDVI calculations from Sentinel-2 and Landsat-8 before and after spectral band adjustment (NDVI adj), for same-day acquisitions. Displaying the results of the ordinary least squares regression, Pearson correlation, and root mean squared error for every study site.

Bands		Study	Ordinary Least Square Regression		Pearson's Correlation	Root Mean Square
S2 Band	**L8 Band**	**Site**	**Intercept**	**Slope**	**Coefficient** (r)	**Error (RMSE)**
NDVI	NDVI	Lena Delta	0.054	0.847	0.98	0.054
		Batagay	0.2	0.65	0.85	0.078
		Yakutsk	0.16	0.74	0.93	0.068
		ES	0.12	0.79	0.95	0.068
NDVI adj	NDVI	Lena Delta	−0.017	1.03	0.98	0.033
		Batagay	−0.027	1.04	0.88	0.037
		Yakutsk	−0.017	1.02	0.96	0.03
		ES	−0.031	1.04	0.97	0.033

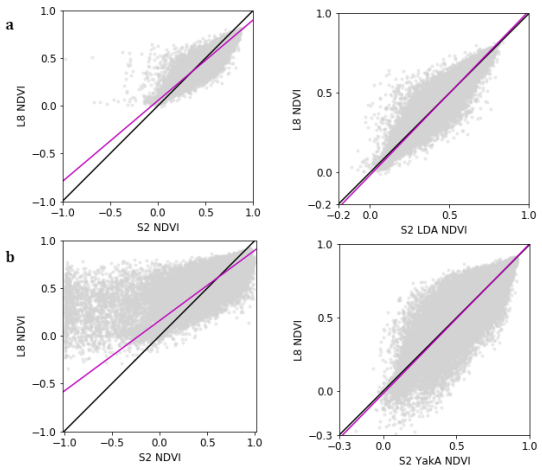

Figure 2.5: Comparison of NDVI values from the Lena Delta ((**a**), upper row) and Yakutsk ((**b**), lower row). Left plots: NDVI calculated from observed Landsat-8 and Sentinel-2 surface reflectance values. Right plots: NDVI calculated from adjusted Sentinel-2 and observed Landsat-8 reflectance values. The solid black line is one-to-one, and the pink line is the ordinary least squares regression trend line.

2.4.3 ES and HLS Spectral Band Adjustment

We used the ES ordinary least squares regression coefficients (Table 2.3) as input for Equation (2.1) and applied these for spectral band adjustment to the three study sites. The results showed that using the ES coefficients for band adjustment also significantly improved the relationship between ES-adjusted Sentinel-2 and Landsat-8 surface reflectance pixel values (Table 2.6). Visually, there was an improvement and a better relationship between ES-adjusted Sentinel-2 and Landsat-8 reflectance values (Figure 2.10). The already previously-observed lower correlation of the visible wavelength bands (B2/B2, B3/B3, and B4/B4) in Batagay were noticeable in this assessment as well.

Table 2.6: Comparison of surface reflectance values from the Sentinel-2 and Landsat-8 corresponding bands after spectral band adjustment, for same-day acquisitions, using the Eastern Siberian (ES) and Harmonized Landsat and Sentinel-2 (HLS) adjustment coefficients. Displaying the results of the ordinary least squares regression, Pearson correlation, and root mean squared error.

			ES Adjustment				HLS Adjustment			
Bands		**Study**	**Ordinary Least Squares**		**Pearson's**	**Root Mean**	**Ordinary Least Squares**		**Pearson's**	**Root Mean**
		Site	**Regression**		**Correlation**	**Squared**	**Regression**		**Correlation**	**Squared**
S2 Band	**L8 Band**		**Intercept**	**Slope**	**Coefficient (r)**	**Error (RMSE)**	**Intercept**	**Slope**	**Coefficient (r)**	**Error (RMSE)**
2	2	Lena Delta	0.0123	0.928	0.927	0.0121	0.020	0.675	0.927	0.014
		Batagay	0.007	0.747	0.624	0.0058	0.013	0.54	0.624	0.0069
		Yakutsk	0	0.970	0.92	0.004	0,008	0.705	0.92	0.0055
3	3	Lena Delta	0.006	0.987	0.962	0.0083	0.019	0.763	0.962	0.010
		Batagay	0.014	0.771	0.726	0.0066	0.025	0.596	0.726	0.0082
		Yakutsk	0.0008	0.968	0.945	0.0043	0.014	0.75	0.945	0.0061
4	4	Lena Delta	0.006	0.962	0.97	0.0077	0.017	0.799	0.97	0.010
		Batagay	0.007	0.884	0.818	0.0067	0.0174	0.734	0.818	0.0109
		Yakutsk	0.00012	0.977	0.964	0.0049	0.012	0.81	0.964	0.0086
8A	5	Lena Delta	−0.0155	1.038	0.95	0.018	0.030	0.834	0.95	0.021
		Batagay	0.0153	0.932	0.902	0.0155	0.057	0.748	0.902	0.0188
		Yakutsk	–0.0001	1.003	0.945	0.0152	0.044	0.805	0.945	0.0186
8	5	Lena Delta	−0.022	1.059	0.943	0.019				
		Batagay	0.012	0.94	0.900	0.0157				
		Yakutsk	0.0003	0.99	0.942	0.0155				
11	6	Lena Delta	0.0098	0.94	0.951	0.014	0.021	0.825	0.951	0.024
		Batagay	0.008	0.953	0.933	0.0113	0.020	0.835	0.933	0.015
		Yakutsk	−0.0028	1.02	0.967	0.0102	0.0096	0.89	0.967	0.014
12	7	Lena Delta	0.003	0.98	0.962	0.011	0.008	0.856	0.962	0.018
		Batagay	0.0039	0.959	0.938	0.0076	0.0039	0.959	0.938	0.0103
		Yakutsk	−0.0009	1.004	0.974	0.0075	0.004	0.88	0.974	0.011

The slope coefficients of the ordinary least squares regression after ES adjustment ranged from 0.928 (Lena Delta B2/B2) to 1.059 (Lena Delta B8/B5). Applying the ES-adjustment coefficients led to some slope coefficients exceeding 1.0 and intercepts that were slightly negative. This was the case for individual band combinations in the Lena Delta and Yakutsk.

Yakutsk seemed to be adjusted the best compared to the Lena Delta and Batagay. This likely was because the ES dataset was dominated by the Yakutsk site, which provided about 80% of the data to the analysis with 1,944,414 pixels compared to 156,315 and 346,053 pixels from the Lena Delta and Batagay sites, respectively (Table 2.2).

Applying the globally-available HLS coefficients for band adjustment to the three study sites showed no significant improvement (Table 2.6). The HLS results actually very much resembled the original spectral band comparisons (Table 2.3). Hence, the relationship between HLS-adjusted Sentinel-2 and Landsat-8 pixel values was not enhanced after HLS adjustment.

2.5 Discussion

Our overall comparison and adjustment results showed a good fit between Sentinel-2 and Landsat-8 in the high latitudes. Despite this, the Batagay study site showed the biggest differences between Landsat-8 and Sentinel-2 reflectance values in the visible wavelength bands. The Batagay same-day image pair, compared to the Lena Delta and Yakutsk example, also contained the highest cloud cover with 38.6% and 49.8% (Table 2.2). While the cloud and cloud shadow detection algorithms still had high omission errors (Foga et al. 2017; Zhu, Wang, and Woodcock 2015), the Batagay images particularly were visibly contaminated with thin cirrus clouds that were difficult to mask. This decreased the quality of the images (Gómez-Chova et al. 2007) and likely was the main cause for a lower correlation coefficient between spectral bands, since the visible wavelength ranges were particularly affected by clouds and cirrus (Bartlett et al. 1998). Landsat-8 and Sentinel-2 were differently sensitive to cirrus clouds, and the acquisition delay of 25 min between the two sensors was sufficient for a change in cirrus conditions in terms of cirrus presence and intensity, which decreased the comparison quality. Claverie et al. (2018) observed this in images with a high cloud cover content as well. The geographic location of the Batagay site between two mountain ranges with very frequent cloud cover and highly variable cloud dynamics precludes better same-day image pair qualities. Arguably, the Batagay image pair should therefore be considered with additional caution; however, in spite of the slightly less favorable adjustment fit, the Batagay study site still had good overall adjustment results and illustrated the applicability of this approach also for challenging areas.

All scatter plots had a reasonable amount of scatter around the one-to-one relationship. Experiments with simulated Landsat-8 and Sentinel-2 data by Zhang et al. (2018) demonstrated that the scatter was emerging from the differing spectral response functions of the bands. Another source for value scatter likely was the different spatial resolutions of the sensors. Mandanici and Bitelli (2016) performed tests that showed that spatially-heterogeneous target surfaces created a lower Pearson correlation coefficient in band comparisons (Mandanici and Bitelli 2016). The Sentinel-2 sensors' high-resolution bands most likely capture the landscape heterogeneity to a greater extent compared to Landsat-8, which then is not averaged out completely in the resampling process to 60-m pixels. Flood (2017) and Roy et al. (2017; 2017) further looked at misregistration, different viewing geometries, and atmospheric path length as potential sources for errors between the sensors. All these points contribute to the scatter between Sentinel-2 and Landsat-8 reflectance values. Overall, we are confident with our

adjustment results as the Pearson's correlation coefficients were high throughout the analyses.

When inspecting the scatter plots, a noticeable number of pixels displayed data discrepancies in the NIR (B8A/B5, B8/B5) and SWIR (B11/B6, B12/B7) band comparisons of Yakutsk and the Lena Delta. In the Lena Delta, Landsat-8 captured little reflectance variability in bands B5 and B6 (between 0.08 and 0.13), while Sentinel-2 recorded reflectance values from 0–0.35 in bands B8A, B8, and B11 for the corresponding pixels. In Yakutsk, the relationship was reversed, where Sentinel-2 recorded nearly no variation in values (0–0.05) in bands B8A, B8, and B11, while Landsat-8 indicated values ranging from 0–0.2 in bands B5 and B6 for the same pixels. This data illustrated the different sensitivities of the two sensors in signal reception and translation to reflectance values. We identified these pixels by building masks to only select the pixels associated with these discrepancies. The majority of these pixels were water or mixed water-land pixels. In the Lena Delta, those pixels were mainly from sandbanks. Despite applying a water mask, these pixels were not masked as they did not fully comply with water characteristics only. The sandbanks have a high bottom reflectance through the thin water column, resulting in mixed reflectance signals, and the extent of water coverage changes strongly with water level changes. Therefore, the water mask failed to mask these pixels properly, and evidently, the Landsat-8 and Sentinel-2 NIR and SWIR bands picked up and converted the mixed signals differently. Likewise, the striking pixels in the Yakutsk NIR and SWIR bands were water body pixels, as well. The Yakutsk area contains many thermokarst lakes and ponds that vary in size and depth, which fosters the likelihood of pixels containing a mixed water and ground signal. Vuolo et al. (2016) made similar observations in pixel differences and accredited the bigger differences to three error sources: heterogeneous and complex terrains, the quality of cloud and cloud shadow masking algorithms, and the challenging and differing atmospheric correction results. Our analyses and study site characteristics confirmed these points and challenges, which underlines that a spectral band comparison can only be based on clear, high-quality images, as reflectance artifacts decrease the quality of the comparison and the adjustment scheme results. Further attention has to be given to the cloud, cloud shadow, and water masking. Under challenging conditions, a manual selection and masking of clear areas for analysis may be inevitable. The NDVI comparison results showed that both Landsat-8 and Sentinel-2 NDVI captured similar vegetation traits and that green vegetation estimations derived from either system would be very similar. However, in this case, it was inevitable to adjust the Sentinel-2 bands spectrally to Landsat-8 since a moderate amount of non-adjusted Sentinel-2 NDVI values were negative in contrast to the Landsat-8 NDVI values.

The overall results demonstrated that Sentinel-2- and Landsat-8-acquired reflectance values for corresponding pixels correlated well in Arctic-Boreal permafrost regions in Eastern Siberia. This was observed for all three study sites separately and also in the combined adjustment for the Eastern Siberian region. This underlines the expected sensor compatibility and agrees with results from similar studies (Claverie et al. 2018; Flood 2017; Gorroño et al. 2017; Mandanici and Bitelli 2016; Zhang et al. 2018). However, our study went slightly beyond some of the previous ones, which partly based their evaluation on simulated Landsat-8 and/or Sentinel-2 image products (Mandanici and Bitelli 2016; Gorroño et al. 2017; Zhang et al. 2018), and not on acquired images. We showed that it is possible to reduce the persistent difference in spectral responses between the measured reflectance values of the spectral bands by deriving and then applying an ordinary least squares regression model, adjusting Sentinel-2 to resemble Landsat-8 reflectance values in Arctic-Boreal permafrost regions. It is possible to create a seemingly perfect fit between spectrally corresponding bands at the individual study site. The best adjustment results were obtained in the local assessments (LDA, BatA, YukA), but closely followed by the regional approach (esA). The ES analysis shows that combining regional data, and deriving overarching adjustment coefficients will lead to a very good fit between Landsat-8 and ES adjusted Sentinel-2 reflectance values in Eastern Siberia as well. We therefore considered our derived adjustment coefficients to be representative for Eastern

Siberia and that they were applicable for a Sentinel-2 to Landsat-8 adjustment throughout Eastern Siberia. The implementation of the globally-applicable HLS coefficients did not improve the spectral comparability of Landsat-8 and Sentinel-2 reflectance values at any of our three Arctic-Boreal study sites or on the regional ES level. This might be because only a few Arctic study sites and merely one Siberian site were included in the HLS product, and therefore, the Eastern Siberian landscape and vegetation forms were not represented enough in the HLS study. This finding is similar to the adjustment results from Flood (2017) for Australian landscapes, and thus, we do not recommend using globally-derived adjustment coefficients for local or regional scale studies, but instead determine region-specific coefficients for a Sentinel-2 to Landsat-8 adjustment.

Being able to adjust Sentinel-2 to Landsat-8 gives the possibility of combining Landsat and Sentinel-2 data in analysis applications. Here, we relied on the already existing data continuity strategy for the Landsat sensors and would like to extend the range of sensors by adjusting Sentinel-2 to Landsat-8 (Flood 2014; Mishra et al. 2014; Teillet et al. 2001; Teillet, Markham, and Irish 2006). Considering the substantial increase in available multispectral images for the high latitudes with Sentinel-2 (Figure 2.1) (Li and Roy 2017), the creation of dense time series is possible. A combined Landsat and Sentinel-2 time series will improve land cover and vegetation mapping and monitoring approaches in detecting shifts in vegetation composition and structure, as well as permafrost region disturbances in a warming climate. A key advantage of dense time series analysis is the capability to detect landscape dynamics and to differentiate between rapid and gradual changes, therefore describing permafrost region disturbances better and being able to conduct detailed trend analysis in Arctic-Boreal permafrost regions.

One of the main motivation to combine Landsat-8 and Sentinel-2 in high latitudes is the frequent cloud cover and therefore the low data availability of cloud-free images. To avoid this disadvantage of optical remote sensing altogether, one can consider using Synthetic Aperture Radar (SAR) sensors that penetrate the cloud cover and acquire data during bad weather conditions, as well. SAR data were applied to a variety of studies focusing on different aspects and applications in northern high latitudes, such as land cover mapping, successfully already (Bartsch et al. 2016). Nonetheless, one general conclusion is that the best results can be obtained from polarimetric SAR data together with optical remote sensing (Ullmann et al. 2014). Despite the advantages of active sensors, in particular SAR, towards frequent cloud cover, we trust assessing permafrost landscape changes with optical remote sensing. On the one hand, the optical remote sensing data archive, mainly Landsat, is the longest archive spanning more than 45 years, providing extensive records of the past. On the other hand, we see high potential in change detection and time series segmentation algorithms, such as LandTrendr, which we would like to apply to permafrost regions and assess disturbance regimes. However, the availability and advantages of SAR data will be an asset when assessing permafrost disturbances, as SAR data can potentially fill data gaps and help as supplementary material to identify and evaluate permafrost landscape disturbances well.

2.6 Conclusions

The overall objective of our study was to compare the spectral characteristics of Landsat-8 and Sentinel-2 across Arctic-Boreal permafrost regions and to assess their compatibility and potential use in a combined time series. Our spectral comparison of Landsat-8 and Sentinel-2 corresponding bands showed that these two sensors correlate well and depict similar trends with only minor differences in Eastern Siberian permafrost regions. Depending on the application purpose, one has to assess whether these differences are negligible or of relevance.

With an ordinary least squares regression based on band comparisons of corresponding Landsat-8 and Sentinel-2 bands, we can successfully adjust the Sentinel-2 reflectance values to resemble Landsat-8 more and homogenize the two data sets. To avoid geolocation errors and account for the sensors' different spatial resolutions, we downscaled our images to 60 m.

The comparison method was valid for adjustments on the local level for sites with different ecological and landscape characteristics, but also when merging data across Eastern Siberia and conducting the spectral comparison and adjustment regionally. This underlines the comparability and compatibility of the two sensors. In contrast, we found that the application of the Harmonized Landsat Sentinel-2 product generated no improvement in spectral adjustment. Relying on global adjustment schemes between Landsat-8 and Sentinel-2 is therefore not advisable for Eastern Siberia or for local to regional time series studies in general. Therefore, we recommend at least regionally-fitted spectral adjustments when jointly using Landsat-8 and Sentinel-2 data products. This minimizes the potentially introduced error from different spectral band responses when combining data from multiple sensors. Our data enable the combined use of Landsat and Sentinel-2 in future time series analysis and other landscape change approaches in Arctic-Boreal permafrost regions of Eastern Siberia. Despite the overall good adjustment results, small differences between the sensors remained, which can be attributed to several factors including heterogeneous terrain, poor cloud and cloud shadow masking, and mixed pixels.

Our assessment was solely based on the use of open source software (GEE, SNAP, Jupyter Notebook) and freely-available data sets (Landsat-8, Sentinel-2). This makes the methodological approach reproducible and allows wide usage also for other study areas. As our results were in line with previous local and regional studies, we acknowledge that these services and softwares are a valuable and useful tool appropriate for such comparison studies.

2.7 Acknowledgements

We acknowledge the support of the Deutsche Forschungsgemeinschaft und Open Access Publishing Fund of University of Potsdam. The authors thank Google for providing the GEE platform at no cost, as well as ESA and USGS for providing Sentinel-2 and Landsat-8 satellite imagery at no cost. Furthermore, the authors thank the three reviewers and editors for their time and valuable input to this manuscript.

2.8 Appendix Chapter 2

Table 2.7: The selected same-day images in Google Earth Engine (GEE) after data filtering for the three study sites.

Study Site	Sensor	Image Name GEE
Lena	L8	LC08_132009_20160823
	S2	20160823T034732_20160823T091448_T51XXA
Batagay	L8	LC08_122012_20160801
	S2	20160801T030546_20160801T064303_T53WMR
Yakutsk	L8	LC08_121017_20160709
	S2	20160709T030011_20160709T081153_T52VEP

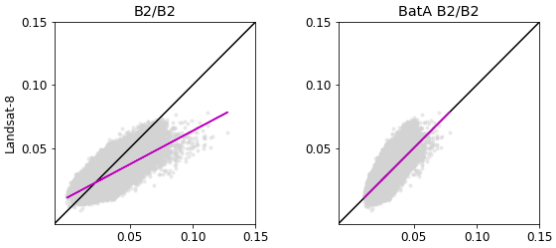

Figure 2.6: Cont.

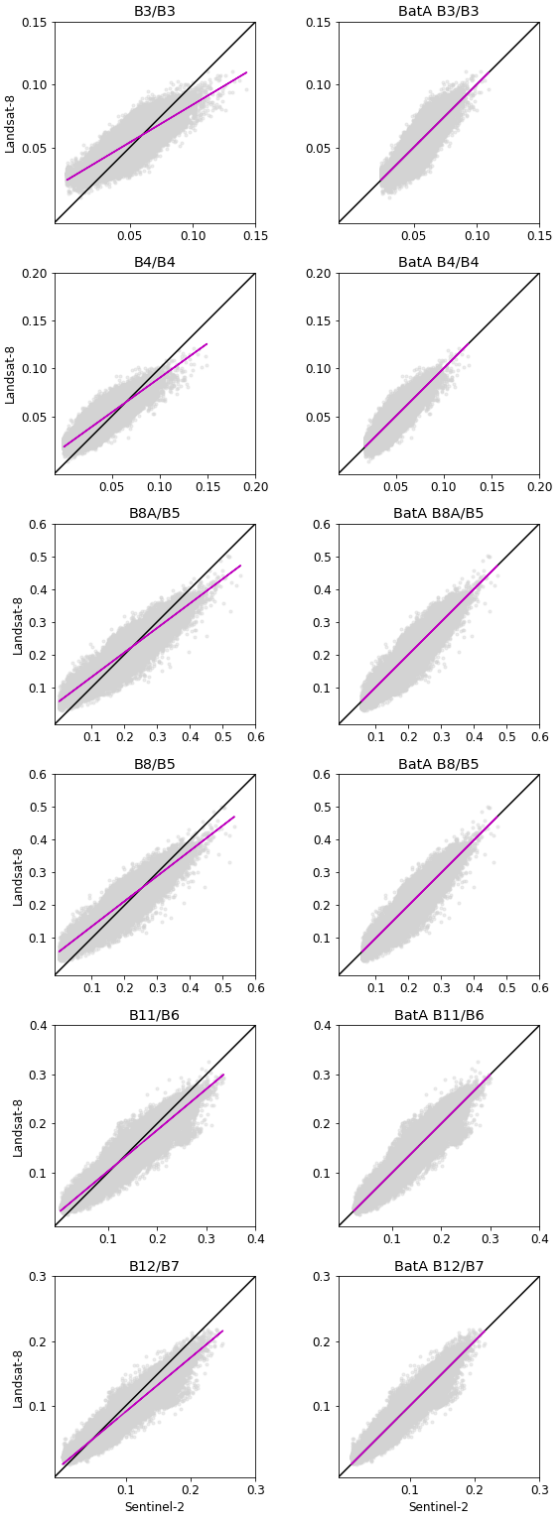

Figure 2.6: Comparison of surface reflectance values from the Sentinel-2 and Landsat-8 corresponding bands for Batagay. Left plots: observed surface reflectance values. Right plots: Batagay Adjusted (BatA) Sentinel-2 reflectance values. The solid black line is one-to-one, and the pink line is the ordinary least squares regression trend line.

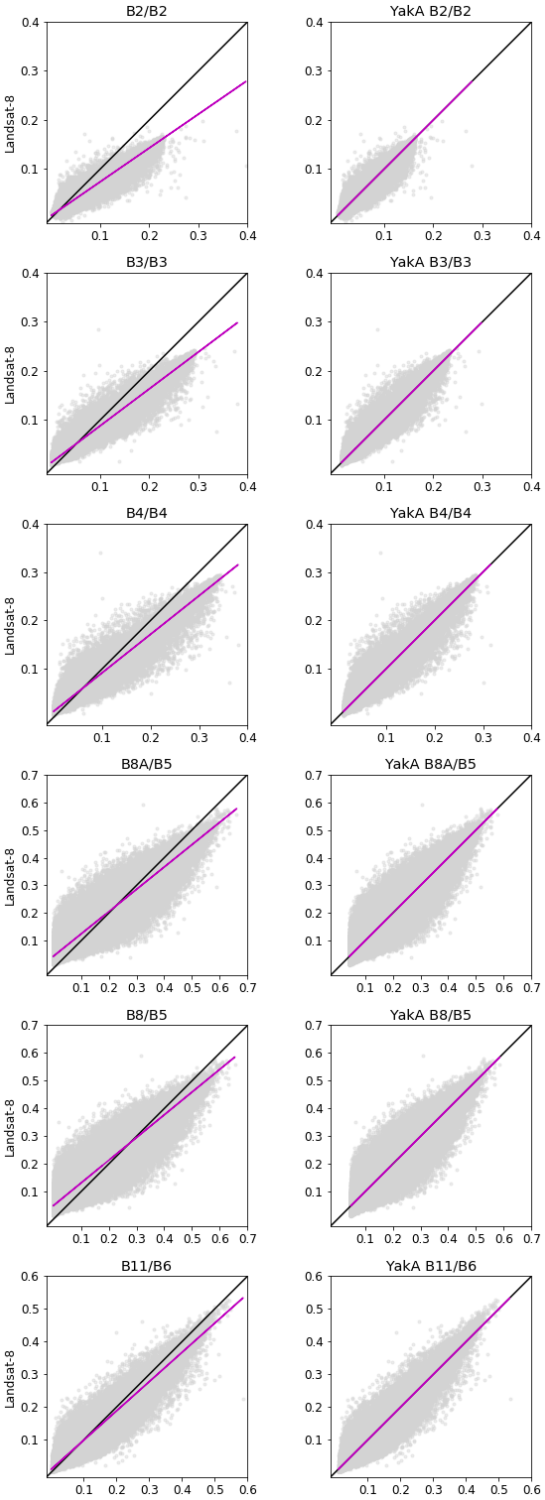

Figure 2.7: Cont.

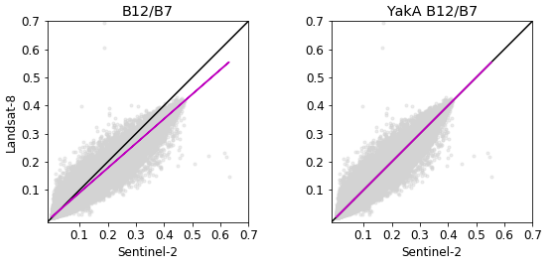

Figure 2.7: Comparison of surface reflectance values from the Sentinel-2 and Landsat-8 corresponding bands for Yakutsk. Left plots: observed surface reflectance values. Right plots: Yakutsk Adjusted (YukA) Sentinel-2 reflectance values. The solid black line is one-to-one, and the pink line is the ordinary least squares regression trend line.

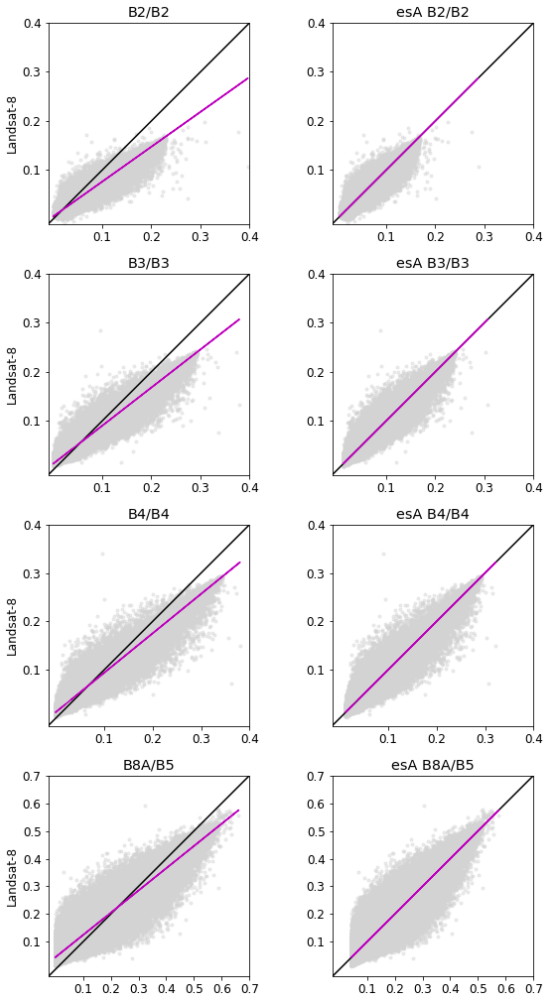

Figure 2.8: Cont.

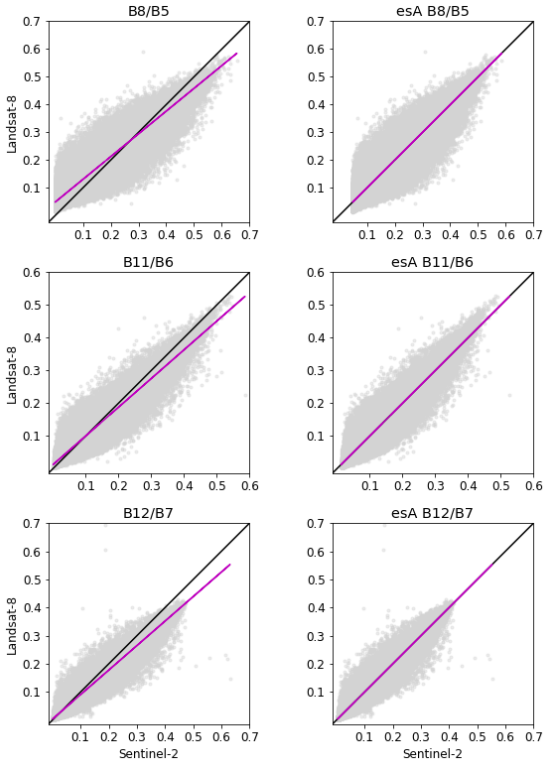

Figure 2.8: Comparison of surface reflectance values from the Sentinel-2 and Landsat-8 corresponding bands for Eastern Siberia. Left plots: observed surface reflectance values. Right plots: Eastern Siberia Adjusted (esA) Sentinel-2 reflectance values. The solid black line is one-to-one, and the pink line is the ordinary least squares regression trend line.

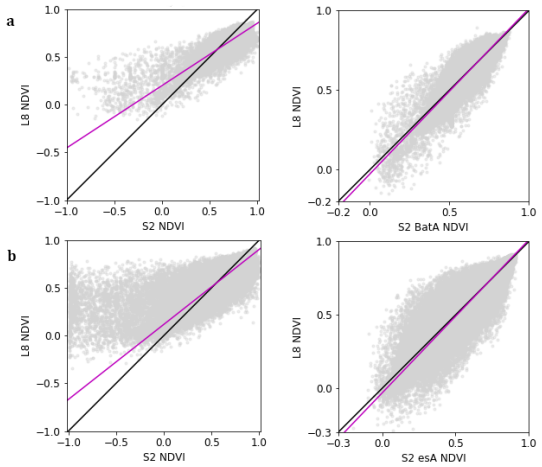

Figure 2.9: Comparison of NDVI values from Batagay ((**a**), upper row) and Eastern Siberia ((**b**), lower row). Left plots: NDVI calculated from observed surface reflectance values. Right plots: NDVI calculated from adjusted Sentinel-2 reflectance values. The solid black line is one-to-one, and the pink line is the ordinary least squares regression trend line.

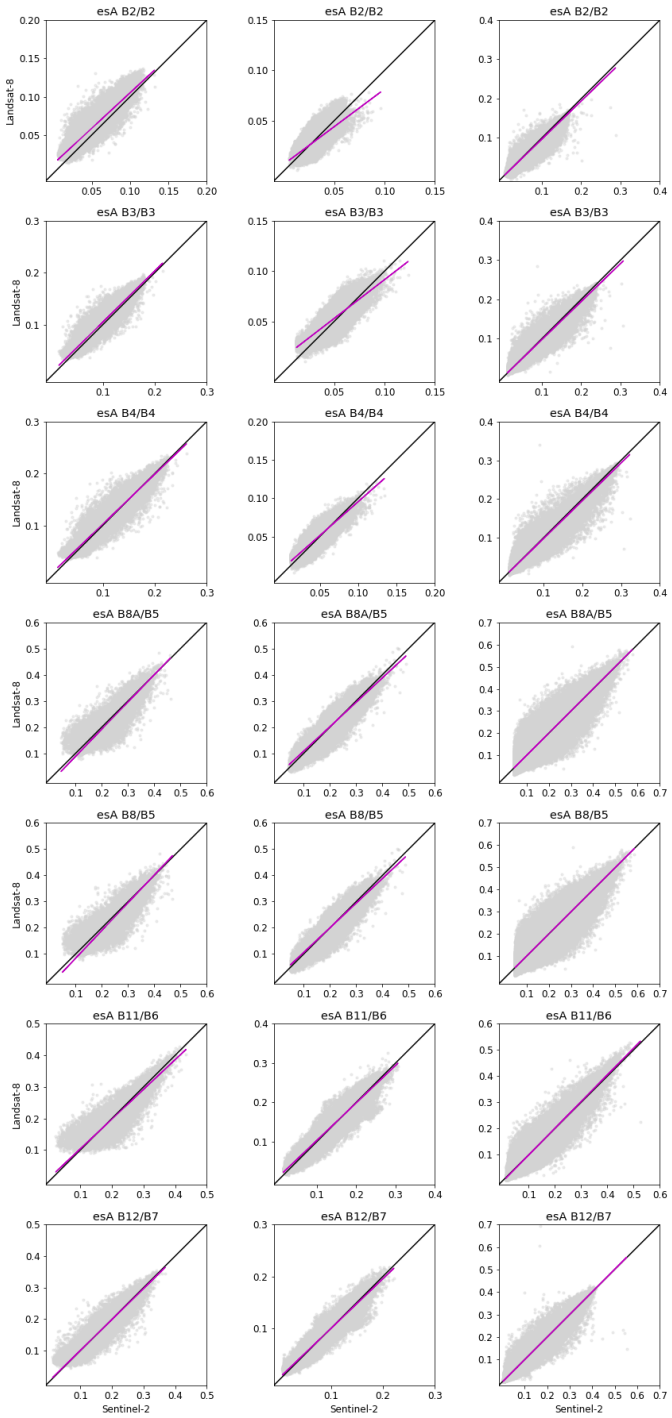

Figure 2.10: Comparison of Eastern Siberian Adjusted (esA) the Sentinel-2 reflectance values and Landsat-8 corresponding bands for the individual study sites. In the order from left to right: Lena Delta, Batagay, and Yakutsk. The solid black line is one-to-one, and the pink line is the ordinary least squares regression trend line.

3

Mosaicking Landsat and Sentinel-2 Data to Enhance LandTrendr Time Series Analysis in Northern High Latitude Permafrost Regions

Alexandra Runge[1,2] and Guido Grosse[1,2]

[1] Alfred Wegener Institute for Polar and Marine Research, Telegrafenberg A 45, 14473 Potsdam, Germany
[2] Institute of Geosciences, University of Potsdam, Karl-Liebknecht-Str. 24-25, 14476 Potsdam-Golm, Germany

Published: 1 August 2020 in *Remote Sensing*, 12(15), doi: 10.3390/rs12152471

3.1 Abstract

Permafrost is warming in the northern high latitudes, inducing highly dynamic thaw-related permafrost disturbances across the terrestrial Arctic. Monitoring and tracking of permafrost disturbances is important as they impact surrounding landscapes, ecosystems and infrastructure. Remote sensing provides the means to detect, map, and quantify these changes homogeneously across large regions and time scales. Existing Landsat-based algorithms assess different types of disturbances with similar spatiotemporal requirements. However, Landsat-based analyses are restricted in northern high latitudes due to the long repeat interval and frequent clouds, in particular at Arctic coastal sites. We therefore propose to combine Landsat and Sentinel-2 data for enhanced data coverage and present a combined annual mosaic workflow, expanding currently available algorithms, such as LandTrendr, to achieve more reliable time series analysis. We exemplary test the workflow for twelve sites across the northern high latitudes in Siberia. We assessed the number of images and cloud-free pixels, the spatial mosaic coverage and the mosaic quality with spectral comparisons. The number of available images increased steadily from 1999 to 2019 but especially from 2016 onward with the addition of Sentinel-2

images. Consequently, we have an increased number of cloud-free pixels even under challenging environmental conditions, which then serve as the input to the mosaicking process. In a comparison of annual mosaics, the Landsat+Sentinel-2 mosaics always fully covered the study areas (99.9–100 %), while Landsat-only mosaics contained data-gaps in the same years, only reaching coverage percentages of 27.2 %, 58.1 %, and 69.7 % for Sobo Sise, East Taymyr, and Kurungnakh in 2017, respectively. The spectral comparison of Landsat image, Sentinel-2 image, and Landsat+Sentinel-2 mosaic showed high correlation between the input images and mosaic bands (e.g., for Kurungnakh 0.91–0.97 between Landsat and Landsat+Sentinel-2 mosaic and 0.92–0.98 between Sentinel-2 and Landsat+Sentinel-2 mosaic) across all twelve study sites, testifying good quality mosaic results. Our results show that especially the results for northern, coastal areas was substantially improved with the Landsat+Sentinel-2 mosaics. By combining Landsat and Sentinel-2 data we accomplished to create reliably high spatial resolution input mosaics for time series analyses. Our approach allows to apply a high temporal continuous time series analysis to northern high latitude permafrost regions for the first time, overcoming substantial data gaps, and assess permafrost disturbance dynamics on an annual scale across large regions with algorithms such as LandTrendr by deriving the location, timing and progression of permafrost thaw disturbances.

3.2 Introduction

Permafrost is warming in the northern high latitudes (Biskaborn et al. 2019), which has considerable impacts on Arctic terrestrial landscapes. Permafrost is ground that remains at or below 0 °C for at least two consecutive years and it covers roughly 25% of the northern hemisphere (Obu et al. 2019). Being defined as a thermal state of the subsurface makes permafrost directly vulnerable to changes in the energy balance of the land surface, in particular the long-term changes in mean annual air temperature, precipitation regimes, and snow distribution and thickness that are currently observed across the high latitudes (Serreze and Barry 2011; Kaplan and New 2006). Continued warming causes widespread permafrost thaw, resulting ultimately in near-surface permafrost loss at local to regional scales (Chadburn et al. 2017). Wide landscape changes can be associated with permafrost thaw and loss and have impacts on ecosystems (Schuur and Mack 2018; Pastick et al. 2019), hydrological systems (Francis et al. 2009; Liljedahl et al. 2016), soil carbon accumulation and decomposition (Hicks Pries et al. 2015), greenhouse gas emissions (Walter Anthony et al. 2018), and stability of infrastructure in permafrost areas (Hjort et al. 2018). Considering the vast area permafrost covers across the northern hemisphere and its strong linkages to the Arctic biophysical system (Box et al. 2019), changes in the distribution of permafrost due to thaw is of high relevance for the Arctic amplification of global climate change (Kaplan and New 2006; Koven et al. 2011).

To make more precise estimations of the impact of permafrost thaw on landscapes and biogeochemical cycles, a more detailed remote sensing-based assessment of permafrost disturbances is necessary. Many thaw-related permafrost disturbances in the northern latitudes such as thermokarst formation, thermokarst lake drainage, flooding, rapid soil erosion, and wildfires (Grosse et al. 2011a; Turetsky et al. 2020) can be tracked with remote sensing methods that provide key information on the distribution, magnitude, duration, and impacts of disturbances (Jorgenson and Grosse 2016; Nitze et al. 2018). However so far, the extent of remotely sensed permafrost disturbance assessments are limited spatially and temporally. Abrupt permafrost disturbance features (Grosse et al. 2011a) have been mainly mapped on local to regional scales, such as retrogressive thaw slumps (Brooker et al. 2014; Nitze et al. 2018; Segal et al. 2016), fires (Frazier et al. 2018), and lake changes (Nitze et al. 2018). These studies either derived disturbance dynamic parameters from few individual time snapshots (Balser, Jones, and Gens 2014; Kokelj et al. 2015a; Lewkowicz and Way 2019; Ward Jones, Pollard, and Jones 2019), or determined

trends across a period of time (Brooker et al. 2014; Nitze et al. 2018). However, knowledge on the annual disturbance dynamics is required on regional to pan-arctic scales. This is crucial for identifying main drivers of abrupt thaw events and including these processes in large-scale climate models.

A number of remote sensing algorithms that were developed for land cover change and forest disturbance applications to detect landscape changes at regional to global scales, capture the temporal dynamics of disturbance features. Since the start of the open access policy of the Landsat data archive in 2008 (Woodcock et al. 2008), Landsat is often chosen for high spatial and temporal resolution land cover and change detection assessments. For example, Hansen et al. (2013) presented a global forest gain and loss algorithm and Pekel et al. (2016) a surface water assessment and its changes with Landsat data. Landsat has the longest available data record, covering more than 48 years, which presents a unique opportunity for long-term assessment studies. Landsat satellites are multispectral sensor systems, providing a spatial resolution of 30 m at nominal revisit times of 16 days covering the whole globe (USGS 2016). The Landsat archive therefore allows to assess processes at high spatial resolution and with a reliable continuous time series for more than several decades by now.

The most widely-used algorithms are the Landsat-based detection of Trends in Disturbance and Recovery (LandTrendr) (Kennedy, Yang, and Cohen 2010), the vegetation change tracker (VCT) (Huang et al. 2010), the Break detection For Additive Season and Trend (BFAST monitor) (Verbesselt, Zeileis, and Herold 2012), the Continuous Change Detection and Classification model (CCDC) (Zhu and Woodcock 2014), and the forest gain and loss algorithm by Hansen et al. (2013), according to a compilation by Zhu (2017) based on algorithm characteristics, such as temporal frequency, change indices, and gradual or abrupt change detection. They all have in common the smallest assessment unit as a pixel but differ in the required temporal data frequency, change index application, the form of disturbance they assess (gradual or abrupt), and whether they are used for near real-time monitoring or past change detection. Since data availability in the northern high latitudes is limited drastically by frequent cloud cover (Ju and Roy 2008), most of the widely-used algorithms that require a very high temporal frequency of input data are not suitable for Arctic applications.

An exception is LandTrendr, as it creates yearly mosaics from cloud-free Landsat images by aggregating cloud-free pixels from a defined period of time, e.g., the summer months (Kennedy, Yang, and Cohen 2010). With this approach, LandTrendr ensures a continuous disturbance assessment with an annual resolution. Using aggregated data as input is a promising method to bypass data limitations in the northern high latitudes (Potapov, Turubanova, and Hansen 2011; White et al. 2014). Moreover, LandTrendr is flexible in change index choice and captures both abrupt and gradual changes. LandTrendr applies a segmentation algorithm for change and trend detection to the time series of annual Landsat mosaics. The segmentation algorithm splits the time series into vertices, points of abrupt spectral change, and time stretches in between of vertices with change, no change or gradual trends, which then represent abrupt and gradual land cover change, respectively. The algorithm results provide information on the disturbance year, magnitude of change, and recovery duration (Kennedy, Yang, and Cohen 2010). Since 2018, LandTrendr is incorporated into Google Earth Engine (GEE) (Kennedy et al. 2018) and is therefore easily transferable to new application areas, benefiting from GEEs processing power and easily available large-scale satellite data sets (Kennedy et al. 2018). The application of LandTrendr to the high latitudes would allow assessing permafrost disturbance processes for the first time with a continuous time series, deriving temporal dynamics on multiyear to annual scales, derived from more than 20 years of data, at high spatial resolution, which has not been achieved before.

However, even the annual LandTrendr mosaics, based on the moderate repeat frequency of Landsat images, contain considerable gaps due to lack of cloud-free images and pixels in some years, in particular at higher Arctic and coastal sites. Additional disadvantages include high latitude environmental factors such as frequent snow and ice cover, a short growing season length, and a challenging solar geometry (Hope and Stow 1996; USGS 2016). As annual cloud- and gap-free mosaics are the prerequisite of a reliable and high-quality time series implementation such as LandTrendr, the single-sensor based algorithm remains prone to local and regional observation gaps in the high latitudes (Egorov et al. 2019). These are major challenges for permafrost disturbance studies as these same regions are also underlain by thaw vulnerable, ice-rich and organic-rich permafrost (Strauss et al. 2013; Obu et al. 2019), where first local studies already show extensive permafrost thaw (Lewkowicz and Way 2019; Ward Jones, Pollard, and Jones 2019). Hence, it is crucial to enhance the input database for a LandTrendr time series analysis for northern high latitude applications.

Active remote sensing sensors such as Synthetic Aperture Radar (SAR) sensors can penetrate clouds and do not rely on sun illumination. Therefore, they are less restricted by weather and illumination conditions, which is very useful in northern high latitudes (Wang et al. 2018). Varying SAR methods have been applied to northern high latitudes for land cover mapping (Bartsch et al. 2016), surface deformation assessments in permafrost regions (Rykhus and Lu 2008; Short et al. 2014; Beck et al. 2015) and active layer thickness estimations (Antonova et al. 2018). While the range of application possibilities of SAR data is broad and promising, one major drawback is its overall sparse data availability due to irregular acquisition schemes from historical SAR sensors such as ERS-1/2 SAR, ALOS-1 PALSAR-1, TerraSAR-X and Radarsat-2 (Strozzi et al. 2018). This has only changed recently since the launch of the Copernicus Sentinel-1 satellites in 2014 and 2016, and their short image acquisition rate in polar areas every 6 to 12 days (Torres et al. 2012). With five years of continuous temporally high-resolution data, the available time series for landscape analysis from Sentinel-1 is comparably short and hence the longer optical remote sensing time series of Landsat is still the preferred choice for long time series analysis assessments as exemplified here.

We here propose to combine Landsat and Sentinel-2 images in the mosaicking workflow to ensure data coverage for a continuous time series and a reliable input basis for change assessment algorithms, such as LandTrendr. The Sentinel-2 system has a comparable sensor to Landsat but consists of two near-identical satellites, which have a combined revisit time of only five days (Drusch et al. 2012). Combining Landsat 8 and Sentinel-2 shortens the overall revisit time in the northern high latitudes drastically, increasing the likelihood of obtaining good quality, cloud-free images (Li and Roy 2017) and potentially enhancing the database for large scale mosaics(Griffiths, Nendel, and Hostert 2019). The two sensors are overall compatible and spectral band adjustment coefficients ensure high spectral comparability (Flood 2017; Claverie et al. 2018), which are also available for Arctic-Boreal regions specifically (Runge and Grosse 2019). Therefore, with the launch of the first Sentinel-2 satellite (Sentinel-2A) there is large potential to improve the annual cloud- and gap-free mosaics from the second half of 2015 onward.

Despite the availability of already existing harmonised Landsat/Sentinel-2 products, such as the Harmonized Landsat and Sentinel-2 surface reflectance data set (Claverie et al. 2018), the Landsat+Sentinel-2 analysis ready data (Frantz 2019) or Sen2Like, a tool to generate Sentinel-2 harmonised surface reflectance products with other sensors (Saunier et al. 2019), these global data sets often show discrepancies to regionally derived and adjusted products (Mandanici and Bitelli 2016; Flood 2017; Runge and Grosse 2019). Hence, a regionally fitted harmonisation approach is favoured for regional applications.

The overall objective of this study is to assess the combination of Landsat and Sentinel-2 data to create good quality mosaics for northern high latitudes as input for high temporal

assessment applications such as LandTrendr in GEE. To address this main objective, we focus on three sub-objectives: (1) adapting a mosaicking workflow to incorporate both Landsat and Sentinel-2 images; (2) evaluating the improved data availability as a basis for annual mosaics when using Landsat and Sentinel-2 data; and (3) demonstrating the Landsat+Sentinel-2 mosaic coverage improvements and the preservation of good mosaic quality. We apply and test this framework to twelve diverse study sites in the high latitude permafrost regions across northern Siberia.

3.3 Materials and Methods

3.3.1 Study Sites

This assessment focuses on the terrestrial northern high latitudes and in particular on northern Siberia. We selected twelve study sites, spanning from Taymyr Peninsula in the west (80°E) to Chukotka Peninsula in the east (172°W) and from the northern margins of the Siberian mainland (77°N) to central Yakutia in the south (61°N) (Figure 3.1). The study sites exemplify a variety of landscapes and cover the range of climatic, geologic, geomorphologic and vegetational conditions in the North Siberian permafrost regions. While all sites except Chukotka are within the continuous permafrost zone (Obu et al. 2019), we included sites which are inland or coastal, with various terrain specifications and elevation levels, within the taiga or tundra ecoregion (Olson et al. 2001), and with different ground ice contents and thus thaw vulnerability (Table 4.1). Climatically the study sites lie within the arctic to boreal climate zones and in both maritime and continental areas which defines the rather broad climate region of northern Siberia (Sayre et al. 2020). The mean annual air temperature (MAAT) for January and July and mean annual total precipitation (MATP) values were extracted from ERA5 data for each study site (**era5**). Furthermore, specific study sites were chosen as they accommodate long field data records and represent frequently visited research areas, such as the Lena Delta, Batagay, Chokurdakh and the Pleistocene Park near Cherskiy.

For our analysis, we defined each study site by determining a centre point and a 25 × 25 km square area around the centre point. From here on, the term study site refers to the general study location while the term AOI refers to the coordinates of the centre point in our processing workflow (Section 3.3.3) and AOIarea to the 25 × 25 km areal (Section 3.3.5) extent of every study site. So, every study site consists of an AOI and an AOIarea.

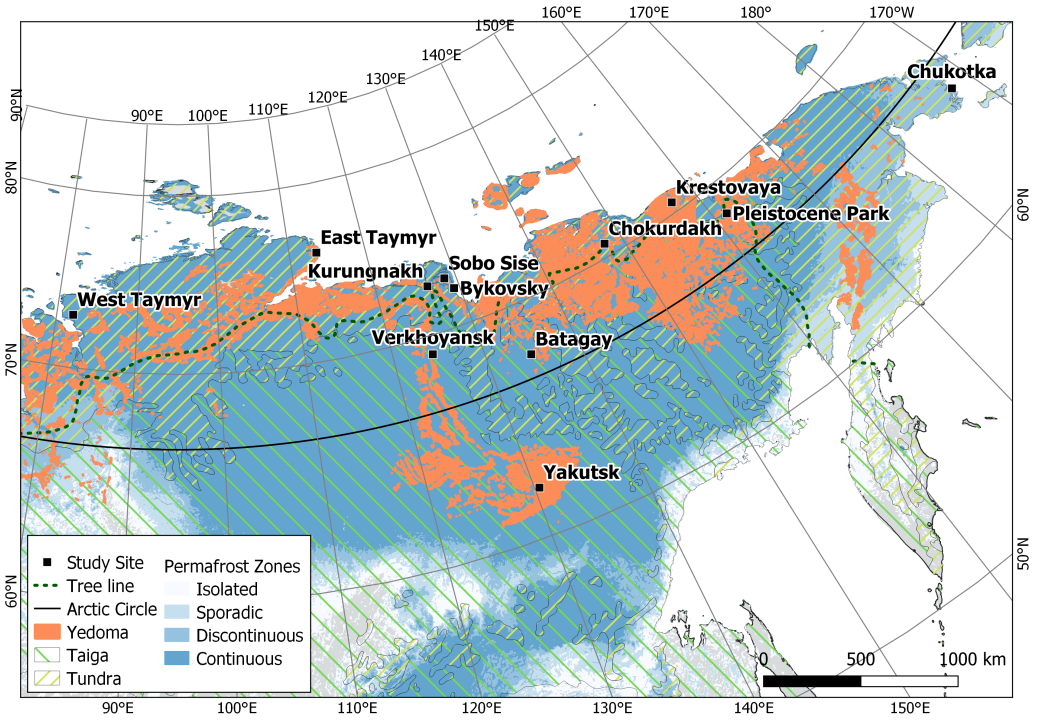

Figure 3.1: Overview of the twelve study sites across northern Siberia. Permafrost zones according to Obu et al. (2019), Yedoma extent according to Strauss et al. (2013) and ecosystem according to Olsen et al. (2001).

Table 3.1: The study sites, their location, and their ecosystem and climatic characteristics.

Study Site	AOI Coord. [°N, °E]	Ecosystem Characteristics	Climatic Characteristics	MAAT Jan, Jul [°C]	MATP [m]
Bykovsky	71.8, 129.3	coastal, lowland, Yedoma, Tundra	Polar, Moist	−28.2, 3.95	0.029
Sobo Sise	72.5, 128.6	coastal, lowland, Yedoma, Tundra	Polar, Moist	−32.1, 8.3	0.024
Kurungnakh	72.4, 126.3	coastal, lowland, Yedoma, Tundra	Polar, Moist	−32.5, 9.97	0.024
East Taymyr	75.6, 113.6	coastal, lowland, Yedoma, Tundra	Polar, Moist	−28.6, 3.8	0.028
West Taymyr	72.6, 82.0	coastal, hilly, Tundra	Polar, Moist	−27.1, 8.1	0.043
Krestovaya	70.5, 157.2	coastal, lowland, Yedoma, Tundra	Polar, Dry	−32.1, 7.7	0.020
Chokurdakh	70.6, 147.9	coastal, lowland to hilly, Yedoma, Tundra	Polar, Dry	−33.9, 10.2	0.024
Pleistocene Park	68.5, 161.4	coastal, lowland to hilly, Yedoma, Tundra	Boreal, Dry	−33.1, 13.1	0.025
Chukotka	65.1, −172.1	coastal, lowland, Tundra	Boreal, Moist	−19.9, 8.97	0.052
Batagay	67.6, 134.8	inland, hilly to mountainous, Yedoma, Taiga	Boreal, Dry	−41.9, 15.7	0.021
Verkhoyansk	69.1, 124.5	inland, hilly to mountainous, Yedoma, Taiga	Boreal, Moist	−36.5, 14.9	0.032
Yakutsk	62.1, 130.5	inland, lowland, Yedoma, Taiga	Boreal, Dry	−38.8, 19.4	0.023

3.3.2 Data

In our study, we worked with Landsat and Sentinel-2 data. The Landsat program is the longest running civilian optical remote sensing operation, continuously acquiring images of our Earth since 1972. Temporally overlapping missions ensured data continuity for more than 48 years already (Irons, Dwyer, and Barsi 2012). The missions' sensors changed moderately over the years but general specifications sustained. Landsat satellites are sun-synchronous, polar-orbiting and have a repeat cycle of 16 days at the equator. The Landsat sensors are multi-spectral imagers, covering a wide range of the electromagnetic wavelength spectrum with their bands, from visible to thermal infrared, and acquiring images with 30 m spatial resolution (Wulder et al. 2019). In 2015 and 2017, the European Space Agency (ESA) launched the Sentinel-2 satellites from their Copernicus program. The Sentinel-2 mission, consisting

of two nearly identical satellites, Sentinel-2A and Sentinel-2B, also operates multi-spectral instruments. Like Landsat, the Sentinel-2 satellites are sun-synchronous and polar-orbiting but have a repeat cycle of 10 days individually and both satellites together of 5 days. Thirteen bands cover the visible to shortwave infrared wavelengths at varying spatial resolutions (10, 20 and 60 m) (Drusch et al. 2012; Hoersch 2015). Landsat 8's Operational Land Imager (OLI, since 2013) and Sentinel-2's Multi-Spectral Instrument (MSI) are overall comparable and their simultaneous operation provides unique opportunities for Earth Observation (Wulder et al. 2019; Wang et al. 2017; Li and Roy 2017). Combined Landsat and Sentinel-2 studies benefit foremost from Landsat's multi-decadal, continuous acquisition scheme and Sentinel-2 high temporal resolution, decreasing gaps in time series from 2015 onward.

We accessed and processed the satellite data on GEE. GEE is a cloud-based platform, providing access to an extensive remote sensing data catalogue, containing a wide range of pre-processed, calibrated, and corrected products, and enabling planetary-scale geospatial analysis supported by Google's computational capacities (Gorelick et al. 2017). For our analysis we accessed the Top-Of-Atmosphere (TOA) image collections from Landsat 5, 7, 8 and Sentinel-2 on GEE (USGS Landsat 5 TM Collection 1 Tier 1 TOA Reflectance; USGS Landsat 7 Collection 1 Tier 1 TOA Reflectance; USGS Landsat 8 Collection 1 Tier 1 TOA Reflectance; Sentinel-2 MSI: MultiSpectral Instrument, Level-1C). The Landsat TOA Tier 1 collections on GEE contain data with calibrated reflectance values (Chander, Markham, and Helder 2009) of the highest geometric and radiometric quality and thus are considered suitable for time series analysis (Google Developers 2020a). Likewise, the Sentinel-2 Level-1C product is also calibrated, geometrically corrected, high quality data (Hoersch 2015). While GEE also incorporates the surface reflectance (SR) products from the Landsat missions, the Sentinel-2 surface reflectance product (Level-2A) is not yet processed globally for the whole Sentinel-2 image archive (Google Developers 2020b). ESA has started to produce Sentinel-2 Level-2A images with their atmospheric correction processor Sen2Cor (Louis et al. 2016; Müller-Wilm, Devignot, and Pessiot 2016) but has not processed the full image archive yet. Currently, only Level-2A images from the most recent acquisitions until March 28th, 2017 are provided with regional differences. For Siberia, only Sentinel-2 Level-2A images from late February, 2019 until now are processed and available on GEE (last checked on July 13th, 2020). As we target to develop an automated workflow taking advantage of easy filtering of continental-scale data sets in GEE, we conducted our analysis with the TOA data for now. While the radiometric quality is improved in the SR products (Flood 2014), the TOA approach is still applicable and relevant, since the TOA spectral properties reflect the ground characteristics well and capture disturbances reliably with prominent spectral signatures. Once the SR product from Sentinel-2 is available, the same workflow can be transferred easily in GEE.

3.3.3 Data Processing and Mosaicking Workflow

The LandTrendr library, provided by Kennedy et al. (2018) on GEE, was the foundation of this work and was successively adapted to the specific needs. In the following, we describe the mosaicking workflow, adaptations and subsequent analysis steps.

We adopted the LandTrendr library and modified the script from image collection filtering, image harmonisation, cloud and cloud shadow masking to mosaic generation. Our code is publicly available: `https://code.earthengine.google.com/8ff1ee9ad801549df413184820bd7f39`.

The biggest modification to the adopted mosaic workflow is the change of input collections. We use the Landsat TOA collections and additionally the Sentinel-2 Level-1C collection

as input (Figure 3.2). Following this adjustment, a harmonisation step for the Sentinel-2 images was included to obtain a consistent spectral database. The remaining overall workflow was maintained and only modified where necessary. The Landsat and Sentinel-2 input was processed in parallel and only combined in the last step before creating a combined mosaic (Figure 3.2, 'buildMosaic: medoid').

The image collections were filtered by AOI, by date and by cloud cover to obtain a subset of the image collection representing the database for the annual mosaics. The AOI was the centre point coordinates of the study sites (Table 4.1), the date filter was set to the summer months (1st July–31st August) to restrict deficiencies due to seasonality and the cloud cover to less than 80%. All collections, Landsat and Sentinel-2, contain pre-processed metadata information on cloud cover extent per scene (Landsat metadata property: cloud cover, Sentinel-2 metadata property: cloud coverage assessment) and cloud and cloud shadow information per pixel (Landsat band: BQA, Sentinel-2 band: QA60), which were used first for general cloud image filtering and later for cloud and cloud shadow pixel masking, respectively (USGS 2020; ESA 2020).

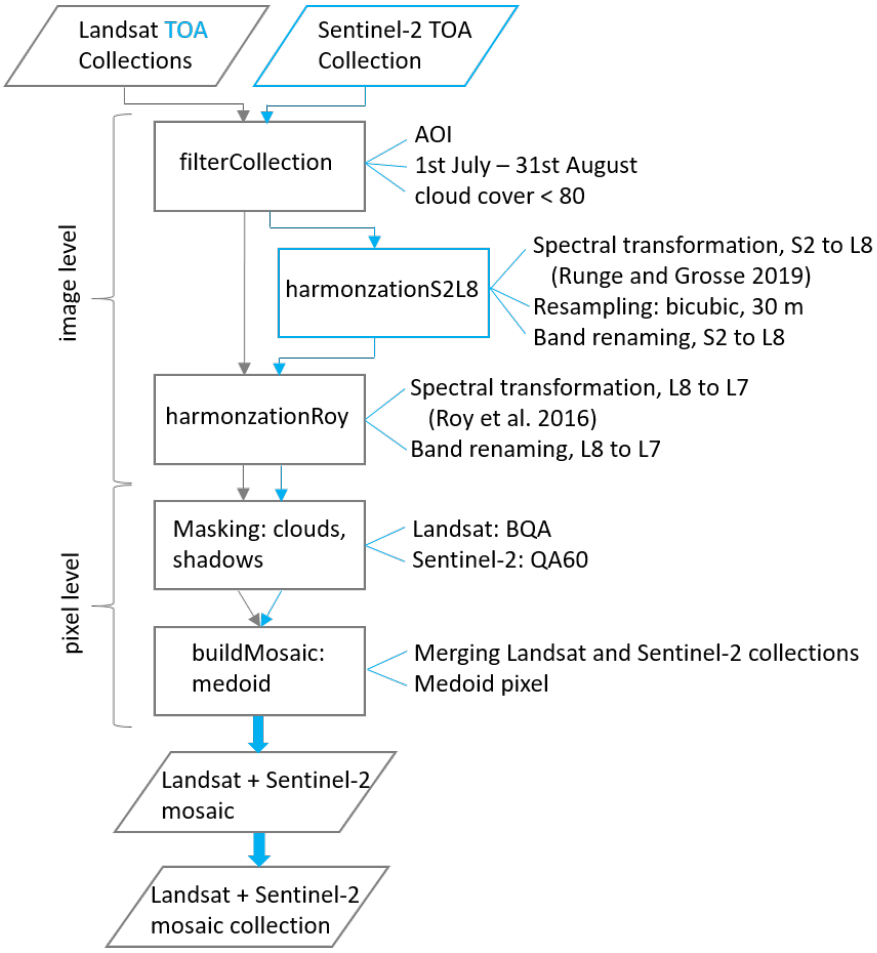

Figure 3.2: Mosaicking workflow. The general workflow follows the method from Kennedy et al. (2018). The modifications are shown in blue.

We implemented Kennedy et al. (Kennedy et al. 2018) harmonizationRoy function, applied to the filtered image collections, to harmonise Landsat 8 OLI images to Landsat 7 ETM+, ensuring consistent spectral properties across the Landsat sensors in the time series. In this case, the TOA spectral transformation coefficients were applied (Roy et al. 2016a) but otherwise the harmonizationRoy function remained unchanged. Six bands are

included in the band transformation, blue (B1), green (B2), red (B3), near infrared (B4), shortwave infrared 1 (B5) and 2 (B7). The band selection is based on Landsat 7's bands and the band availability across the different Landsat sensors. Landsat 8's corresponding bands are selected and renamed in the harmonizationRoy function. Following the example of the harmonizationRoy function, we implemented a similar harmonisation scheme for Sentinel-2 data to guarantee consistent spectral reflectances across Landsat and Sentinel-2 data (harmonizationS2L8). First, we harmonised the Sentinel-2 images to Landsat 8, by applying spectral transformation coefficients for Arctic-Boreal regions for TOA data and resampled them to 30 m spatial resolution, resembling Landsat data. We derived Sentinel-2 to Landsat-8 spectral transformation coefficients for TOA data for Arctic-Boreal regions from the same study set up and workflow as described by Runge and Grosse (2019) but used not the SR same-day images but the same TOA images as data input. We applied GEEs' reproject() and resample() functions for images and reprojected the Sentinel-2 images to Landsats' projection (WGS 84, UTM), a scale of 30 m and applied the bicubic resampling method. Secondly, we transformed the adjusted Sentinel-2 images further to Landsat 7 with the harmonizationRoy function, as described above for TOA Landsat data.

Until here, we operated on the image level. In the next steps, we processed the images in the image collections further on the pixel level. The cloud and cloud shadow masking were achieved by using the provided quality bands. For Landsat we used the quality assessment bitmask (BQA) (USGS 2020) and for Sentinel-2 we used the QA60 Bitmask (QA60) (ESA 2020). Both quality bands are bitmasks that contain information on the presence of clouds and cloud shadows at the pixel level. Consequently, we masked out all pixels with a cloud or cloud shadow, based on the information in the quality band bitmask. The remaining cloud-free pixels form the input database for the mosaic process described next.

After image filtering and pixel masking the last step was to generate annual mosaics based on our processed database, which can be applied to every study site and assessment year. Kennedy et al. (2010; 2018) create medoid mosaics in their LandTrendr workflow. A medoid is similar to a median and represents the point with the minimal summed distance to all points in a data set but considers multiple dimension in its selection, which are the different bands in this case (Flood 2013). Medoid mosaics are resilient against extreme values, such as outliers from unmasked cloud or cloud shadow pixels, and provide representative mosaics of a defined time period (Flood 2013). As the cloud and cloud shadow masking is not impeccable (Coluzzi et al. 2018) and our assessment strongly relies on a specific narrow time period, the summer months July and August, we maintained the medoid mosaic approach and applied the medoid mosaic function from the LandTrendr library (Kennedy et al. 2018). Input of the medoid mosaic function are the annual Landsat and Sentinel-2 image collections that already are filtered, harmonised and cloud masked at this point. Both collections are merged and then the medoid mosaic function identifies the medoid for every pixel within the merged collection. Output of the function is a mosaic image, which is cloud-free and spectrally representative for the summer months as we used the medoid function.

The above described workflow runs systematically for every year of the assessment period, generating a cloud-free mosaic. These annual mosaics are combined in a mosaic collection, representing a mosaic time series for a study site. For our assessment we created a 21-year mosaic collection from 1999 to 2019. This time period includes seventeen years of Landsat-only mosaics, from 1999 to 2015, when Landsat data started to be reliably and consistently available for Siberia, and the last four years of combined Landsat and Sentinel-2 mosaics. We extended the assessment period beyond the overlapping Landsat and Sentinel-2 period to draw comparisons between Landsat-only and combined Landsat+Sentinel-2 mosaics.

3.3.4 Data Availability Assessment

Prerequisite of good quality annual mosaics are a good input database. The above described processing workflow defines the framework for high quality mosaic outputs, minimising artefacts from seasonality, merging of multi-sensors or clouds and cloud shadows. We further assess the quality of the combined Landsat+Sentinel-2 mosaic output by looking at the input data availability and the spectral characteristics of the mosaic outputs.

We assessed the data availability on both image and pixel level. As a general rule, the bigger and more robust the input database is in form of number of images and number of cloud-free pixels, the better the mosaic output. Therefore, we derived for every study site the image list of available images with the GEE filterCollection function, for Landsat and Sentinel-2 separately. The image list contains all images fulfilling the filter requirements from the mosaicking workflow (AOI, date and cloud cover). The result is an available image count for the specific study site per year, specifying images that cover the AOI, were acquired in July and August, and are not completely cloudy. The image count number illustrates the general input database for the mosaicking workflow.

The previously derived image list is input for a cloud-free pixel analysis. The filtered image list might still contain images with a high cloud or cloud shadow cover across the AOIarea, as the filtering is based on metadata information (Landsat metadata property: cloud cover, Sentinel-2 metadata property: cloud coverage assessment), which were derived for the full Landsat (185 × 185 km) or Sentinel-2 (290 × 290 km) scenes. Input to the medoid mosaicking process should be cloud-free pixels only, hence we apply pixel-based cloud and cloud shadow masking as described in Section 3.3.3. Therefore, not only the available image count is of interest but more importantly the number of cloud-free pixels. To assess this, we applied the buildClearPixelCountCollection function from the LandTrendr library to every study site (Kennedy et al. 2018). The buildClearPixelCountCollection function takes the filtered image collection as input, applies the cloud and cloud shadow masking to every image in the collection, which operates on the pixel level, and counts the remaining number of clear pixels for every pixel at the study site, for every year of the assessment period. The output of the function is an image collection, containing one band image per year (1999–2019) with the cloud-free pixel count for every location. For a more representative picture, we did not look at the clear pixel count at every pixel but calculated the average number of clear pixels for every study site, aggregated across the AOIarea. Within the 25 × 25 km square of a study site the cloud-free pixel count slightly varies spatially, mainly because of overlapping sensor swaths, the Landsat 7 ETM+ scan line corrector failure and partial cloud cover, but not significantly. Hence, an aggregated average per study site is a good representation. This averaged cloud-free pixel count is derived for every year in the assessment period.

3.3.5 Mosaic Coverage and Quality Assessment

Eventually, the main goal is to generate good quality mosaics. We assessed the quality of the resulting combined Landsat+Sentinel-2 mosaics by study area coverage and spectral characteristics. For the four years that we have both Landsat and Sentinel-2 data available, 2016 to 2019, we created two mosaics for every year and study site. One mosaic with Landsat TOA data only (Landsat-only mosaic) and the second one with Landsat and Sentinel-2 data together (Landsat+Sentinel-2 mosaic), following the above mosaic workflow. For both mosaics we calculated the percentage they cover of the study site area (AOIarea). The annual mosaics can contain holes from data gaps, given that no cloud-free pixel was available at a location for the mosaic. With the area calculation we can compare which mosaicking result, Landsat-only

or Landsat+Sentinel-2 mosaic, more reliably produces a full study site coverage (Roy et al. 2010).

As described in Section 3.3.3 we ensure spectral consistency across the different sensors by applying harmonisation functions, including spectral transformations. Nevertheless, to confirm that the combined Landsat and Sentinel-2 data workflow produces representative and radiometric consistent good quality mosaics, we conducted a spectral comparison between cloud-free images and the Landsat+Sentinel-2 mosaic (White et al. 2014).

For every study site we selected individual cloud-free Landsat 8 and Sentinel-2 images, fulfilling the previously stated filtering requirements, by AOI and date range, except lowering the maximum cloud cover value to less than 30%. We selected the images with no cloud or cloud shadow across the AOIarea. For every study site we found for one year a cloud-free Landsat 8 and Sentinel-2 image fulfilling these requirements (Table 3.2) and conducted the spectral comparison for that years' Landsat+Sentinel-2 mosaic and the selected Landsat 8 and Sentinel-2 images.

For comparability, we applied the same harmonisation approach that is also part of the mosaic workflow, to the individual Landsat 8 and Sentinel-2 images. The Landsat 8 images were transformed with the harmonizationRoy function and the Sentinel-2 images in two steps, first with the Sentinel-2 to Landsat 8 band transformation (harmonizationS2L8) and then also with the harmonizationRoy function. We then sampled 5000 random pixel locations (GEE sample function) per study site (AOIarea) and extracted the spectral band values of the Landsat image, the Sentinel-2 image and the Landsat+Sentinel-2 mosaic. The random pixel locations were only taken from the areas where both images and the mosaic overlapped. We downloaded the data sets with the spectral pixel values from GEE and conducted a spectral band comparison in Jupyter Notebook. For every band we compared the corresponding spectral values between the Landsat image and the Landsat+Sentinel-2 mosaic and the Sentinel-2 image and the Landsat+Sentinel-2 mosaic separately and calculated the correlation coefficients (r-value), indicating the strength of linear relationship between image and mosaic pixel spectral values (Cowan 1998). Six bands were included in this assessment, blue (B1), green (B2), red (B3), near infrared (B4), shortwave infrared 1 (B5) and 2 (B7).

Table 3.2: The cloud-free Landsat and Sentinel-2 images per study site for the spectral band comparison.

Study Site	Year	Landsat (LANDSAT/LC08/C01/T1_TOA/)	Sentinel-2 (COPERNICUS/S2/)
Bykovsky	2018	LC08_127010_20180826	20180727T035541_20180727T035537_T52WEE
Sobo Sise	2018	LC08_130009_20180815	20180828T034529_20180828T034525_T51XXA
Kurungnakh	2018	LC08_132009_20180728	20180809T040541_20180809T040543_T51XXA
East Taymyr	2018	LC08_204237_20180805	20180825T051639_20180825T051642_T49XEE
West Taymyr	2019	LC08_160009_20190719	20190718T064629_20190718T064632_T44XNF
Krestovaya	2016	LC08_109010_20160806	20160804T013657_20160804T032423_T56WPD
Chokurdakh	2018	LC08_116010_20180813	20180804T022549_20180804T022545_T55WEU
Pleistocene Park	2019	LC08_105012_20190819	20190816T012701_20190816T012658_T57WWS
Chukotka	2019	LC08_085014_20190705	20190806T231601_20190806T231556_T02WMT
Batagay	2018	LC08_122012_20180807	20180711T024549_20180711T024544_T53WMR
Verkhoyansk	2018	LC08_129011_20180808	20180808T034529_20180808T034530_T51WWS
Yakutsk	2019	LC08_120017_20190727	20190726T024559_20190726T024554_T52VEP

3.4 Results

3.4.1 Data Availability Assessment

We assessed the number of available Landsat and Sentinel-2 images by study site for 1999 to 2019 (Figure 3.3). For 1999 to 2015, only Landsat images from the sensors Landsat 5 TM, 7 ETM+, and 8 OLI are available. The absolute number of available Landsat images varies across study sites but overall the number of Landsat images increases within the study period. The lowest number of images available for most study sites is in 1999, ranging from 0 Landsat images in East Taymyr to 6 Landsat images in West Taymyr. The number of applicable Landsat images increases continuously, with the number of available Landsat images exceeding 25 for West Taymyr in 2013 (33 images), Yakutsk in 2015 and 2017 (26 and 27 images) and Batagay in 2013 (26 images). Sobo Sise has the lowest total number of available Landsat images from 1999 to 2019 with 105 images and Yakutsk the highest total number of images with 303. There are noticeable image count peaks in the time series, including for West Taymyr, Bykovsyk and Batagay in 2013 (33, 17, and 26 images, respectively), Chokurdakh in 2014 (25 images), Chukotka in 2007 and 2015 (14 images) and Yakutsk in 2007, 2005 and 2011 (22, 25, and 23 images, respectively).

The steady increase of Landsat images from 1999 to 2019 as well as the image peaks are due to temporally overlapping satellite missions and changes in acquisition specifications. The image peaks described correspond to acquisition mission overlaps of Landsat 5 TM and Landsat 7 ETM+ (peaks 2005, 2007, 2011) or Landsat 7 ETM+ and Landsat 8 OLI (peaks 2013, 2014) (Wulder et al. 2019). Similarly, the overall low number of Landsat images at East Taymyr can be explained with unavailable Landsat 5 TM acquisitions. Additionally, Landsat 8's changed acquisition specifications facilitate better coverage of northern high latitudes. The increased acquisition rate (>700 scenes/day), increased storage capacities, and changed off-nadir viewing capability of Landsat 8 allow for acquisitions up to 84° latitude for the first time (Wulder et al. 2019), a tremendous benefit for northern high latitudes.

For 2016 to 2019 also Sentinel-2 images are available. From 2016 onward the number of available Sentinel-2 images generally increases. Chukotka has the lowest number of Sentinel-2 images in 2016 with 4 images and East Taymyr the highest number of Sentinel-2 images in 2018 with 162 images. The absolute number of Sentinel-2 images per year mostly exceeds the number of Landsat images for the same year. The years 2018 and 2019 represent Sentinel-2 image peaks for all study sites, except Yakutsk. Since 2017, the Sentinel-2 mission is in full operation after its staggered satellite launch in 2015 (Sentinel-2A) and 2017 (Sentinel-2B), acquiring images continuously and resulting in an enhanced image availability from 2018 onward (Drusch et al. 2012). The observable decline in available images and cloud-free pixels in 2019 is a result of the extensive wildfires throughout Siberia in that year.

The number of cloud-free pixels by study site corresponds closely to the trend of the number of images, the more images available the more cloud-free pixels are available as well. There are no cloud-free pixels for East Taymyr in 1999 and 2002 and Krestovaya in 2001. For all study sites, the maximum number of cloud-free pixels is in either 2018 or 2019, except for Chukotka, West Taymyr and Yakutsk. In general, the highest numbers of cloud-free pixels are from 2016 to 2019, where both Landsat and Sentinel-2 images are available.

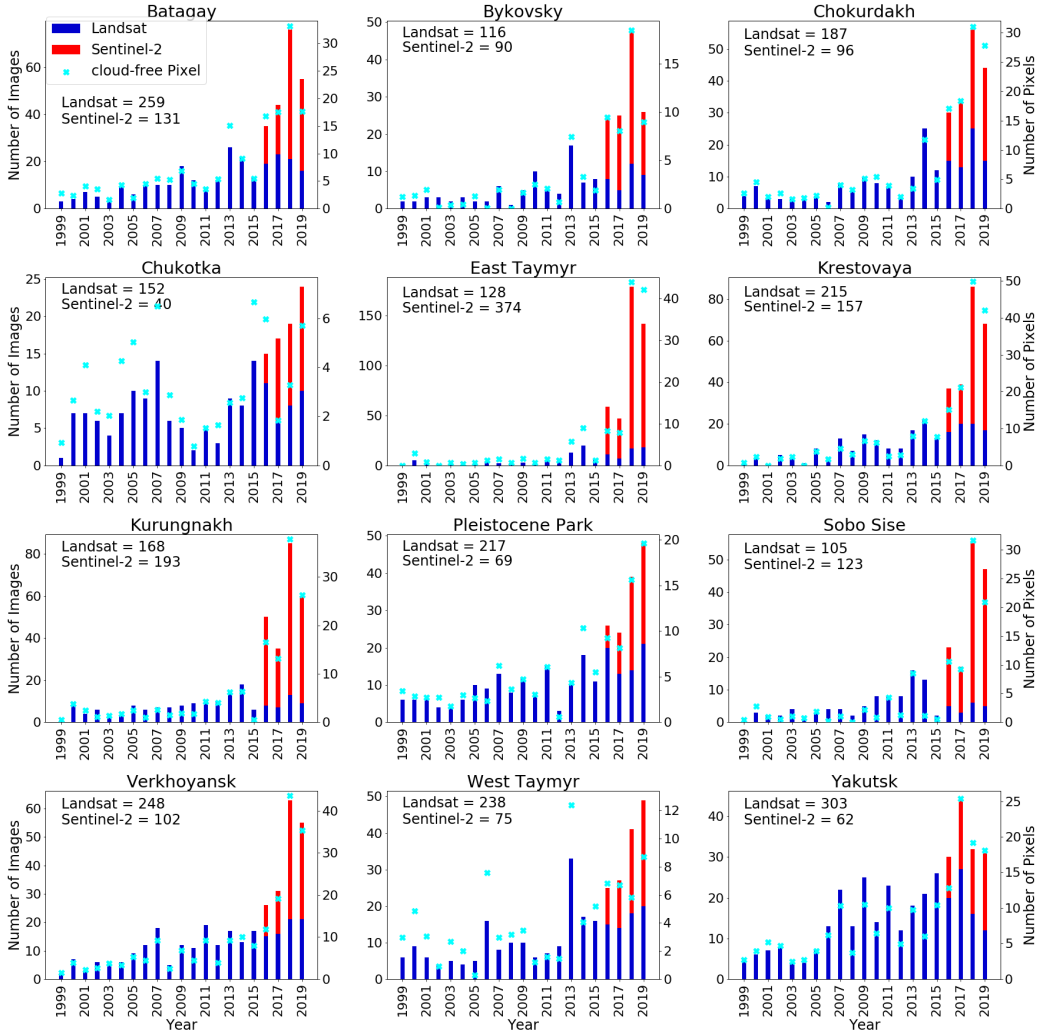

Figure 3.3: Data availability results for all twelve study sites. The bar plots indicate the number of available Landsat (blue) and Sentinel-2 (red) images, corresponding to the first y-axis (left). The crosses indicate the average number of cloud-free pixels per study site (AOIarea), corresponding to the second y-axis (right). The total number of Landsat and Sentinel-2 images are stated in the left corner of each plot.

Overall, the number of available images increases drastically with the addition of Sentinel-2 images and likewise the number of cloud-free pixels, enhancing the database for the mosaicking workflow greatly.

3.4.2 Mosaic Coverage and Quality Assessment

For the predefined 25 × 25 km study site areas (AOIarea) we calculated the mosaic coverage percentages for 2016–2019 and created the Landsat-only mosaics and also the Landsat+Sentinel-2 mosaics for all twelve study sites. Table 3.3 shows the area coverage results exemplarily for Kurungnakh for 2016–2019, and for those study sites where one or both mosaics did not fully cover the AOIarea. Figure 3.4 illustrates the difference between the Landsat-only and Landsat+Sentinel-2 mosaic for Kurungnakh in 2019. Mosaic gaps are clearly visible in the Landsat-only mosaic and discolouring from cirrus and haze. Contrary to this, the Landsat+Sentinel-2 mosaic shows full coverage and a homogeneous mosaic result. The study sites and years not shown in Table 3.3 have an area coverage of >99.9% for both mosaics. We consider a difference of <0.1% between the Landsat-only and Landsat+Sentinel-2 mosaic

coverage of a study site as negligible.

While the Landsat+Sentinel-2 mosaics consistently cover the whole study areas, the Landsat-only mosaics frequently contain holes and gaps (Table 3.3). Sobo Sise has the lowest Landsat mosaic coverage with 27.2% in 2017 and East Taymyr a considerably low coverage of 58.1% in 2017 as well. For the same years, the combined Landsat+Sentinel-2 mosaic achieves a full coverage of the study sites. While Table 3.3 clearly points out the benefits of the Landsat+Sentinel-2 mosaics in terms of area coverage for several sites, it also shows that there are study sites with only very small area coverage discrepancy between Landsat-only and Landsat+Sentinel-2 mosaic. We conducted the area comparison in mosaics for four years (2016–2019) for each study site, which results in 48 area comparisons in total. Out of the twelve study sites, six study sites (Kurungnakh, Bykovsky, Sobo Sise, East Taymyr, Krestovaya, Chukotka) show differences in area coverage of >0.1% for thirteen years of area comparison together (Table 3.3). The other six study sites (West Taymyr, Yakutsk, Verkhoyansk, Batagay, Chokurdakh, and Pleistocene Park) show no differences in the same four years. Our analysis clearly shows that combining Landsat and Sentinel-2 images in the mosaic workflow always reliably produces a full study area coverage of 99.9–100%.

Table 3.3: Area Coverage Calculation showing the percentage covered of the study sites (AOIarea) by the Landsat mosaic and the combined Landsat+Sentinel-2 mosaic.

Study Site	**Year**	**Landsat Mosaic** [%]	**Landsat+Sentinel-2 Mosaic** [%]
Kurungnakh	2016	99.7	100
	2017	69.7	100
	2018	100	100
	2019	92.2	100
Bykovsky	2016	97.3	100
	2017	72.9	100
	2019	98.7	100
Sobo Sise	2017	27.2	100
	2019	83.6	100
East Taymyr	2016	97.1	99.9
	2017	58.1	99.9
Krestovaya	2019	98.5	100
Chukotka	2017	95.3	100
	2019	99.7	100

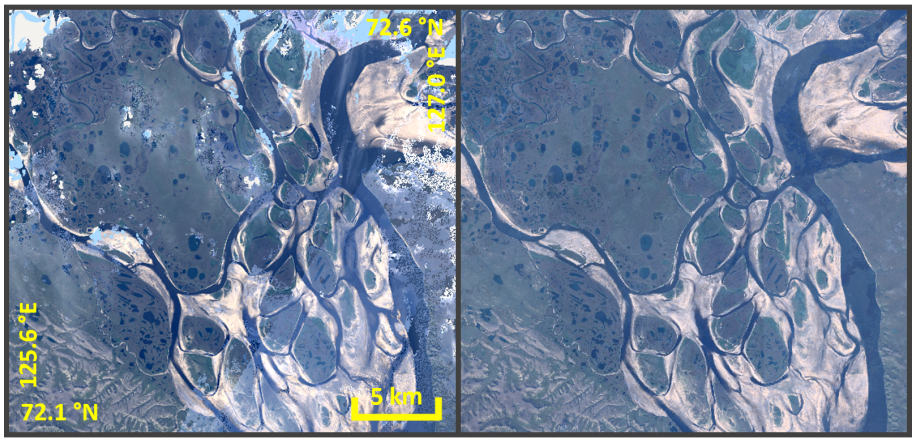

Figure 3.4: Landsat-only mosaic (**left**) and Landsat+Sentinel-2 mosaic (**right**) of Kurungnakh for 2019.

To assess the quality of the Landsat+Sentinel-2 mosaics we conducted spectral band comparisons between the mosaics and single cloud-free Landsat and Sentinel-2 images (Table 3.2), assessing the radiometric consistency of the mosaics. We here depict the spectral band comparisons as scatter plots from Kurungnakh as a representative example of all study sites (Figure 3.5). In Table 3.4 we also display the correlation coefficients (r-values) of the spectral band comparisons of the other study sites.

There is a strong agreement between the Kurungnakh Landsat+Sentinel-2 2018 mosaic and the Landsat 8 image as well as the mosaic and the Sentinel-2 image, only showing minor scatter along the one-to-one line (Figure 3.5). The spectral band comparisons show a strong correlation between both images and the mosaic, across all six bands. The r-values illustrate this as well with the lowest r-value of 0.91 and 0.92 (Band 1) and the highest of 0.97 and 0.98 (Band 4) for the Landsat and Sentinel-2 image, respectively.

We found similar close correlations for the other study sites as well (Table 3.4). An exception is the Krestovaya spectral comparison of Band 1 of the Sentinel-2 image and the Landsat+Sentinel-2 mosaic with an r-value of 0.28, indicating poor correlation. However, all other Sentinel-2 band correlations for Krestovaya are much higher, ranging from 0.60 (Band 2) to 0.93 (Band 5), signalling medium to good agreement. It is noticeable, that the general correlation between the images and mosaics for Band 1 are the lowest, for both Landsat and Sentinel-2 comparisons, followed by Band 2 and Band 3. The comparisons for Band 4–7 are overall much higher and indicate strong correlations. The noticeable lower correlation coefficients for Band 1, 2 and 3, the blue, green and red wavelength spectrum respectively, are likely on account of the poorer quality of TOA products (USGS Product Guide 2018) as well as the stronger effect of atmospheric conditions, clouds and cirrus, on the visible wavelength ranges (Bartlett et al. 1998; Gómez-Chova et al. 2007; White et al. 2014).

There are no distinct differences or trends across the twelve study sites. All study sites show a good correspondence between the mosaic, the Landsat, and Sentinel-2 image. Furthermore, there is also no noticeable difference between the Landsat - mosaic and Sentinel-2 - mosaic comparison. The correlation coefficient values between these two comparisons for one study site are always very close to one another. This underlines that there is no specific trend or sensor bias in the Landsat+Sentinel-2 mosaic as neither Landsat image nor Sentinel-2 image shows higher agreement to the output mosaic.

Table 3.4: The correlation coefficients (r-values) from the spectral band comparisons for each study site between the Landsat image and the Landsat+Sentinel-2 mosaic and between the Sentinel-2 image and the Landsat+Sentinel-2 mosaic (see Table 3.2).

	Landsat 8						Sentinel-2					
Study Site	**B1**	**B2**	**B3**	**B4**	**B5**	**B7**	**B1**	**B2**	**B3**	**B4**	**B5**	**B7**
Bykovsky	0.82	0.87	0.85	0.99	0.99	0.99	0.75	0.88	0.89	0.99	0.99	0.99
Sobo Sise	0.46	0.58	0.63	0.91	0.9	0.85	0.88	0.91	0.91	0.96	0.94	0.92
Kurungnakh	0.91	0.93	0.94	0.97	0.96	0.93	0.92	0.95	0.95	0.98	0.97	0.95
East Taymyr	0.40	0.51	0.78	0.95	0.92	0.90	0.48	0.71	0.91	0.99	0.99	0.99
West Taymyr	0.68	0.77	0.80	0.94	0.89	0.90	0.57	0.64	0.68	0.89	0.86	0.86
Krestovaya	0.55	0.76	0.90	0.97	0.97	0.97	0.28	0.60	0.78	0.91	0.93	0.91
Chokurdakh	0.61	0.78	0.85	0.98	0.98	0.96	0.61	0.79	0.84	0.97	0.97	0.95
Pleistocene Park	0.64	0.84	0.79	0.96	0.97	0.96	0.67	0.88	0.87	0.98	0.99	0.98
Chukotka	0.70	0.85	0.90	0.99	0.99	0.99	0.68	0.88	0.93	0.99	0.99	0.99
Batagay	0.73	0.87	0.94	0.97	0.97	0.97	0.66	0.84	0.89	0.95	0.95	0.94
Verkhoyansk	0.91	0.95	0.96	0.98	0.99	0.98	0.91	0.95	0.96	0.99	0.99	0.98
Yakutsk	0.69	0.81	0.93	0.93	0.97	0.97	0.66	0.80	0.92	0.93	0.97	0.97

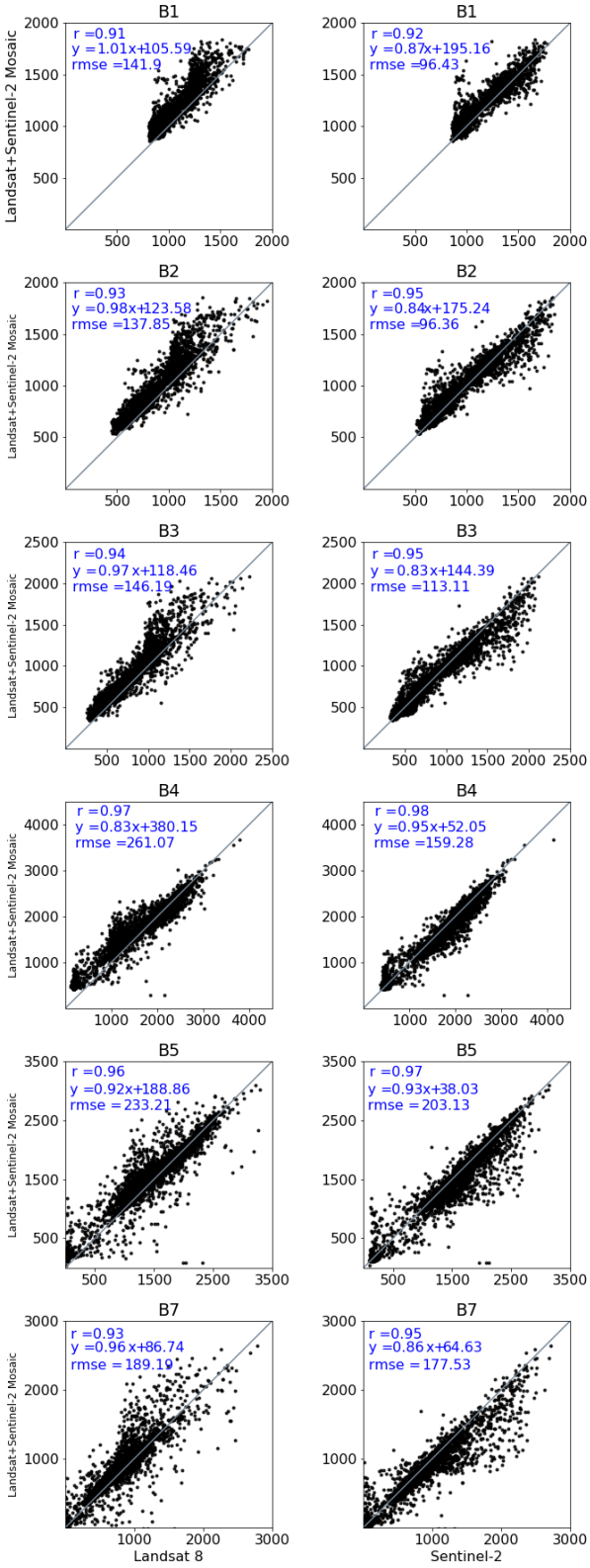

Figure 3.5: Spectral band comparison for the Kurungnakh site, with the TOA Landsat+Sentinel-2 mosaic reflectance values on the y-axis and the Landsat 8 TOA (**left column**) or Sentinel-2 TOA (**right column**) reflectance values on the x-axis. The grey line is the one-to-one trend line. The correlation coefficient (r-value), least square regression equation and root mean squared error (rmse) for every band comparison is also shown.

3.5 Discussion

The mosaic results and the study area coverage highly depend on the available images and cloud-free pixels in one year, which in turn is dependent not only on the scene acquisition rate but also on climatic and local weather conditions during July and August. In general, both Landsat and Sentinel-2 are highly influenced by local weather conditions as they are both optical sensor systems. Yet, the combined Landsat 8 and Sentinel-2 revisit time is very short, at around 2.9 days at the equator and even shorter in the northern high latitudes (Li and Roy 2017). Their combined use highly increases the likelihood of obtaining cloud-free images during July and August in a year, potentially providing a more robust database for the mosaics, which is the most important prerequisite for large scale mosaics (Potapov, Turubanova, and Hansen 2011; White et al. 2014). Our results confirm this, as not only the number of images but especially also the number of cloud-free pixels increases greatly for all twelve study sites when combining Landsat and Sentinel-2, enhancing the input database for the mosaic workflow.

When the usable image database is sufficient, the Landsat-only mosaics can achieve a full coverage of a study area. In 2018 for example this is possible for Kurungnakh. The same applies for the six study sites mentioned in Section 3.4.2 where the Landsat-only mosaics achieve a coverage of 99.9–100%. These findings suggest that the existing Landsat-only approach may be sufficient in some cases. However, at the same time half of our study sites were not fully covered by Landsat-only mosaics and the mosaic coverage strongly benefited from the adapted Landsat and Sentinel-2 mosaic workflow. The increased number of images and especially also the increased number of cloud-free pixels when adding Sentinel-2 data to the mosaicking workflow ensured a full coverage of the study areas. Hence, a full study site coverage can most reliably be achieved by the combined Landsat+Sentinel-2 mosaics.

In our assessment we can observe a north to south gradient in both Landsat image and cloud-free pixel availability as well as in the study area coverage. The total number of Landsat images for every study site extends from Sobo Sise in the north with the least number of images to Yakutsk, the most southern study site, with the highest number of usable Landsat images. This north-south gradient in usable image numbers is observable across the whole Landsat acquisition period due to the differing data acquisition strategies of Landsat sensors, satellite on-board memory capacities, and satellite and sensor geometries (Egorov et al. 2019; Ju and Roy 2008). In addition, there is a south to north gradient in cloudiness from more drier continental sites farther inland with less cloudiness to sites with more maritime influence at the Arctic coast with more frequent clouds and fog. Hence, predominantly the most northern study sites are not fully covered by the Landsat-only mosaics in certain years, such as Kurungnakh, Bykovsky, Sobo Sise, East Taymyr, Krestovaya and Chukotka. These areas are especially prone to cloud cover and fog, which decreases the number of usable images considerably, making the mosaicking more challenging (White et al. 2014). The two platforms of Sentinel-2 help counterbalancing this effect along the north-south gradient, ensuring a more stable database across the latitudes. Thus, assessments in the northern high latitudes especially benefit from the Landsat+Sentinel-2 mosaic workflow as it ensures full spatial coverage and a reliable time series.

Our analysis primarily focused on the spatial dimension of mosaic coverage but the spatial completeness of annual mosaics also directly impacts time series assessments. In time series analysis the complete annual mosaics ensure a temporally consistent database without data gaps across years. In contrast, spatially incomplete mosaics result in missing years and thus temporal gaps in the time series. For example, there are no images and therefore also no cloud-free pixels available for East Taymyr in 1999 and 2002, and in six more years (2001, 2003, 2004, 2005, 2008, 2010) there are only few images available and therefore on average less than 1 cloud-free pixel across the AOIarea. A Landsat-only time series analysis for the high

Arctic coastal site East Taymyr is therefore questionable since the yearly database is irregular and unreliable. Only from 2016 onward with the additional availability of Sentinel-2 data does the number of cloud-free pixels increase substantially, allowing for spatially complete annual mosaics and indicating the first stretch of temporal consistent data useful for a potential time series analysis. Our findings underline the advantage of combining data from multiple sensors on the overall data availability for continuous, good quality time series analyses (Egorov et al. 2019).

Being able to create a reliable annual mosaic database starting as early as 1999 for time series analysis is already an extensive improvement. However, for certain ecosystem or biophysical dynamics, such as changes in vegetation phenology, an annual time stamp is not sufficient but a much higher intra-annual temporal resolution is required (Zeng, Jia, and Epstein 2011; Beamish et al. 2020). While we do not assess this here specifically, we assume that this combined mosacking workflow of Landsat and Sentinel-2 data has the potential to produce intra-annual mosaics. As the combined repeat cycle of Landsat and Sentinel-2 data is less than 2.9 days in the northern high latitudes (Li and Roy 2017), the enhanced Landsat and Sentinel-2 image database may allow to create multiple mosaics for a year, covering for example spring, summer and autumn time. While we cannot obtain a very high temporal resolution as for example MODIS does yet, we however achieve a much higher spatial resolution with Landsat and especially Sentinel-2 (10 to 30m), delivering new insights into small-scale changes in heterogeneous permafrost landscapes.

In this study we closely follow the workflow from the GEE LandTrendr algorithm. However, changing the input data sets from the SR product to the TOA collections and adding another sensor, potentially introduces inaccuracy to the mosaic output. One step to minimise errors is to apply a stringent workflow and apply per-pixel compositing rules (Potapov, Turubanova, and Hansen 2011), which was already established in the LandTrendr workflow and is maintained in this adaptation. The overall spectral comparisons between Landsat+Sentinel-2 mosaic and Landsat and Sentinel-2 images show close agreement between the input images and the resulting mosaic. The strong correlation to both independent, single-date Landsat and Sentinel-2 images underlines that there are no systematical artefacts introduced in the mosaicking process. The applied image transformation and harmonisation steps, which were further extended to the Sentinel-2 images, result in a compatible database. Since the correlation coefficients of both comparisons do not show a better fit to either Landsat or Sentinel-2 image, the medoid mosaic output evidently manages to create representative, sensor-unbiased annual output mosaics (Flood 2013; White et al. 2014). Overall, surface reflectance images are of higher quality than TOA images, because of their advanced calibration and radiometric corrections. In order to detect and monitor more subtle changes, that are reflected in smaller spectral change signatures such as shifts in vegetation, it is necessary to use SR data instead of TOA (Masek et al. 2006). We are confident that once Sentinel-2 SR data is available the workflow can be easily adapted to SR data and deliver mosaic results with similarly good spectral characteristics, as the TOA spectral comparison results are already very positive.

The huge potential of earth observation applications combining Landsat and Sentinel-2 have been comprehensively discussed even before the launch of Sentinel-2 (Drusch et al. 2012; Wulder et al. 2015; Gómez, White, and Wulder 2016). An important step is the harmonisation and transformation of the sensor products that enables the combined use of Landsat and Sentinel-2 (Runge and Grosse 2019; Flood 2017; Chastain et al. 2019; Mandanici and Bitelli 2016; Claverie et al. 2018). The possibilities of sensor combination range from data fusion approaches (Wang et al. 2017), temporal aggregations (Carrasco et al. 2019; Shang and Zhu 2019) to combined spatial annual mosaics for large area coverage, such as Canada (White et al. 2014), Germany (Griffiths, Nendel, and Hostert 2019), or Africa (Xiong et al. 2017). Creating large scale mosaics, especially in areas with data limitations, remains challenging (White et al. 2014; Roy et al.

2010; Potapov, Turubanova, and Hansen 2011). Especially the northern high latitudes benefit from earth observation approaches combining multiple platforms and sensors, as they are otherwise very restricted in data availability, limiting remote sensing time series analysis hugely.

This study presents an approach to achieve full spatial coverage of northern high latitude permafrost regions with remote sensing data on an annual basis for the first time. The combined Landsat and Sentinel-2 mosaic workflow accomplishes both a high spatial and also temporal data coverage, needed for studying a range of ecosystem and landscape dynamics in rapidly changing Arctic and Boreal regions (Box et al. 2019). A high temporal resolution of data is important for understanding disturbance evolution, frequency, and impacts (Kasischke et al. 2013). An annual temporal resolution of time series analysis allows to assess highly dynamic permafrost pulse disturbances and possibly even identify the main disturbance drivers. Thermokarst lake dynamics and particularly lake drainage events have currently only been identified and described based on multiple-date images or trend analysis (Jones et al. 2020; Nitze et al. 2017; Olthof, Fraser, and Schmitt 2015; Hinkel et al. 2007). An annual time series analysis will help to narrow down change drivers and identify inter-annual lake dynamics, such as partial or full drainage, or intermittent infilling, which otherwise remain undiscovered in multi-year trend data. This similarly applies to retrogressive thaw slumps, which occur widely across the terrestrial Arctic (Nitze et al. 2018). They are highly dynamic permafrost disturbances but an annual monitoring was not possible so far across large regions, limiting understanding of potential links to climatic and weather conditions that drive the slumping dynamics (Brooker et al. 2014; Balser, Jones, and Gens 2014; Kokelj et al. 2015a; Lewkowicz and Way 2019; Ward Jones, Pollard, and Jones 2019). We therefore anticipate that these processes can be detected and monitored in greater detail when applying LandTrendr with Landsat+Sentinel-2 annual mosaics. The LandTrendr analysis output will deliver information on the location and timing of thaw disturbances, the temporal progression on an annual basis since 1999, and possibly forms a foundation for volumetric change analysis in areas where multi-year digital elevation models are available. These results will give new estimations of the impact of permafrost thaw on landscapes, biogeochemical cycles, and the biophysical systems. Since this approach is fully scalable, the more detailed and homogeneous remote sensing-based assessment of permafrost disturbances and their annual dynamics on regional to pan-arctic scales will provide crucial information for identifying main drivers of abrupt thaw events in the permafrost domain. The results will also help including these processes in large-scale climate models, something that has been lacking so far and was identified as an important knowledge gap (Grosse et al. 2011c; Grosse et al. 2016; Turetsky et al. 2020).

3.6 Conclusions

The overall objective of this study was to assess the combination of Landsat and Sentinel-2 data in a mosaic workflow to create good quality annual mosaics for the growing season (July and August) as input for high temporal time series assessments in northern high permafrost latitudes. We found that the number of available images, as well as the number of cloud-free pixels, increases drastically when combining Landsat and Sentinel-2 images. The combined Landsat and Sentinel-2 input database for mosaics is thus highly enhanced, which improves the mosaic results as the combined Landsat+Sentinel-2 mosaics cover the spatial extent of study areas reliably without data-gaps. Especially northern, coastal sites benefit from the combined Landsat+Sentinel-2 approach, where Landsat-only mosaics show poorer results. A stringent mosaic workflow, including spectral harmonisation functions between Landsat and Sentinel-2, ensures data consistency across sensors and achieves homogeneous, good quality mosaics from Landsat and Sentinel-2 as shown by spectral comparison between images and

mosaic outputs. Applying the Landsat+Sentinel-2 mosaic approach by aggregating image data annually for a set time period accomplishes not only high spatial but also continuous temporal coverage enabling large scale time series assessments. Based on our findings we conclude that our approach combining Landsat and Sentinel-2 data makes LandTrendr in principle suitable for permafrost disturbance assessments also in challenging environments of northern high latitudes, where frequent clouds, fog, and snow and ice cover limit the acquisition of good quality multispectral imagery. The application of LandTrendr with our combined Landsat- and Sentinel-2 mosaic approach to the high latitudes will allow assessing permafrost disturbance processes for the first time with a continuous time series, deriving temporal dynamics, such as disturbance location, timing and temporal progression since 1999, on an annual scale which has not been achieved before. Following large-scale or circumpolar permafrost disturbance assessments will deliver highly needed consistent and scalable input for climate models.

3.7 Acknowledgements

We thank Google for providing access to the Google Earth Engine resources and R. Kennedy and his team for providing the original LandTrendr algorithm and thorough documentation. We thank the four anonymous reviewers for their time and valuable input to this manuscript. We acknowledge the support of the Deutsche Forschungsgemeinschaft and Open Access Publishing Fund of University of Potsdam.

4

Remote Sensing Annual Dynamics of Rapid Permafrost Thaw Disturbances with LandTrendr

Alexandra Runge [1,2], Ingmar Nitze [1] and Guido Grosse [1,2]

[1] Alfred Wegener Institute for Polar and Marine Research, Telegrafenberg A 45, 14473 Potsdam, Germany
[2] University of Potsdam, Institute of Geosciences, Karl-Liebknecht-Str. 24-25, 14476 Potsdam-Golm, Germany

in Review in *Remote Sensing of Environment*

4.1 Abstract

Permafrost is warming globally, leading to widespread permafrost thaw. Particularly ice-rich permafrost is vulnerable to rapid thaw and erosion, impacting whole landscapes and ecosystems. Especially retrogressive thaw slumps (RTS) are abrupt disturbances that expand by up to tens of meters each year and lead to an increased soil organic carbon release. Local remote sensing studies have identified increasing RTS activity in the last two decades by increasing number of RTS or heightened RTS growth rates. However, a large-scale assessment across diverse permafrost regions and in high temporal resolution allowing to further determine RTS thaw dynamics and its main drivers is still lacking.

In this study we adapt the automatic disturbance detection algorithm LandTrendr for large-scale RTS identification and mapping at high temporal resolution. We adapted and parametrised the temporal segmentation algorithm for annual gradual and abrupt disturbance detection to incorporate Landsat+Sentinel-2 mosaics, ran the temporal segmentation for the tasseled cap greenness index with tailored parameters, conducted spectral filtering based on the LandTrendr output, spatial masking and filtering, and finally a binary machine-learning object classification of the disturbance output to separate between RTS and false positives (F1

score: 0.609). We apply the algorithm to North Siberia (8.1 x 10^6 km^2). Ground truth data for calibration and validation of the workflow was collected from 9 known RTS cluster sites using very high-resolution RapidEye and PlanetScope.

Our study presents the first automatically derived assessment of RTS distribution and temporal dynamics at continental scale. We identified 50,895 RTS and a steady increase in RTS-affected area from 2001-2019 across North Siberia, with a more abrupt increase from 2016 onward, indicating heightened thaw slump dynamics in this period. Overall the RTS-affected area increased by 331 % compared to 2000 (2000: 20,158 ha, 2001-2019: 66,699 ha). Contrary to this, 5 focus sites show spatio-temporal variability in their annual RTS dynamics, with periods of increased and decreased RTS development, indicating a close relationship to varying thaw drivers. The majority of identified RTS was active from 2000 onward and only a small proportion initiated during the assessment period, highlighting that the increase in RTS-affected area was mainly caused by enlarging existing RTS and not by new RTS. The detected increase in RTS dynamics underlines the importance of assessing abrupt permafrost disturbances with high spatial and temporal resolution at continental scales. Obtaining such consistent disturbance products will be useful to parametrise regional and global climate change models.

4.2 Introduction

Permafrost is warming globally and experiences intensifying rates of degradation (Biskaborn et al. 2019; Vasiliev et al. 2020; Farquharson et al. 2019). As permafrost is defined by the thermal state of the ground, with a temperature being at or below 0 °C degrees for at least two consecutive years, the state and extent of permafrost is highly dependent on the prevailing thermal regime of the land surface (Brown et al. 1997). Key indicators of Arctic climate change such as increasing air temperatures, intensifying precipitation events, declining sea ice thickness and spring snow cover extent impact the state of the permafrost (Box et al. 2019), ultimately leading to increased permafrost temperatures and inducing widespread permafrost thaw (Biskaborn et al. 2019). Near-surface permafrost loss impacts whole landscapes (Jorgenson and Grosse 2016), ecosystems (Schuur and Mack 2018), hydrological systems (Liljedahl et al. 2016), urban infrastructure (Hjort et al. 2018) and soil carbon accumulation and decomposition (Hicks Pries et al. 2015; Walter Anthony et al. 2018), resulting in increased rates of soil organic carbon release (Schuur and Abbott 2011; Turetsky et al. 2019).

While permafrost warming is observed to cause widespread gradual active layer deepening across the pan-arctic permafrost region (Park, Kim, and Kimball 2016), ice-rich permafrost is particularly vulnerable to rapid thaw and erosion as high ground ice contents may accelerate degradation by thermokarst (Kokelj and Jorgenson 2013) and thermo-erosion (Are 1988) processes. These processes are often driven by other pulse disturbances such as strong warming or precipitation events, hydrological changes, fires, or direct anthropogenic impacts on the soil thermal regime (Grosse et al. 2011b). Resulting degradational landforms include thermo-erosional gullies and valleys (Morgenstern et al. 2021), degrading ice wedge polygons (Liljedahl et al. 2016), thermokarst lakes (Grosse, Jones, and Arp 2013), steep permafrost coastal bluffs (Günther et al. 2013), active layer detachment slides (Lewkowicz 2007), and retrogressive thaw slumps (Burn and Lewkowicz 1990), all which change landscapes more drastically and much faster than gradual top-down thaw by active layer deepening (Turetsky et al. 2020).

While remote sensing does not directly sense permafrost, a subsurface phenomenon defined by ground temperature only, it does allow improved estimation of the distribution, magnitude and impact of permafrost thaw landforms and processes associated with melt of

excess ground ice. In addition, other permafrost region characteristics such as land cover, land surface temperature, and soil moisture can be observed with remote sensing (Jorgenson and Grosse 2016; Westermann et al. 2015b; Trofaier, Westermann, and Bartsch 2017) and help improve landscape-scale permafrost models (Obu et al. 2019). Given the remoteness and vast extent of permafrost regions, remote sensing-based data and techniques are the only tools to detect, monitor and assess permafrost disturbances at regional to continental scales with spatial and temporal consistency. Abrupt permafrost region disturbances, such as wildfires (Frazier et al. 2018), retrogressive thaw slumps (Brooker et al. 2014; Segal et al. 2016; Nitze et al. 2018), coastal erosion (Irrgang et al. 2018; Jones et al. 2018), and thermokarst lake change and drainage (Nitze et al. 2017; Nitze et al. 2020) have been mainly mapped on local to regional scale. Additionally, the temporal resolution of many assessments ranges from few individual snapshots in time on decadal scales (Irrgang et al. 2018; Morgenstern et al. 2021), which is characterised by labour and time intensive manual mapping approaches, to deriving disturbance trends from multi-decadal time series data (Brooker et al. 2014; Nitze et al. 2018), which rely on automatic algorithm-based methods.

Open image archives and newly available cloud-computing possibilities abolished previous data and processing restrictions and led to an expanded development of remote sensing-based time series and disturbance detection algorithms, with an increased focus on high temporal resolution assessments (Zhu 2017). Especially the Landsat archive, containing the longest continuous data set comprising nearly 50 years of multi-spectral high resolution (30 m) images acquired with a 16-day revisit cycle, has been used for large-scale time series assessments (Wulder et al. 2019). Prominent examples are annual global forest maps (Hansen et al. 2013) and global surface water changes (Pekel et al. 2016). Advanced disturbance algorithms differ in targeted observed change (gradual vs. abrupt), spectral index applications, temporal input data frequency, and whether they detect past changes or conduct near real-time monitoring (Zhu 2017). This development also provides new means to detect and monitor abrupt permafrost disturbances in large-scale assessments at high temporal resolution. While the existing algorithms already provide diverse assessment options, change and disturbance detection in northern high latitudes is still challenging as time series studies with optical remote sensing are restricted due to frequent cloud cover, short summer periods, and low illumination angles. This confines data availability drastically and limits algorithm applications that require high temporal input data. However, the combination of imagery from multiple similar sensors, such as Landsat and Sentinel-2, increases data availability in the northern high latitudes strongly and enhances change and disturbance detection at high temporal resolution (Runge and Grosse 2019; Runge and Grosse 2020).

In this study we focus on the development of a remote sensing method for automatically identifying and mapping retrogressive thaw slumps across continental scale regions. Retrogressive thaw slumps (RTS) result from slope failure after thawing of ice-rich permafrost which is found either in ice-rich Yedoma regions (Strauss et al. 2017b) or formerly glaciated areas that still contain permafrost-preserved buried glacial ice (Kokelj et al. 2017). Initiated by fluvial processes, thermo-erosion or mass wasting following heavy precipitation events and the exposure of ice-rich permafrost, RTS expand successively into the landscape with retrogressive growth of a steep headwall and the increase of a slump floor, rapidly and irreversibly changing the landscape (Ardelean et al. 2020; Kokelj and Jorgenson 2013; Séjourné et al. 2015). RTS vary in size, ranging from under 0.15 ha to mega slumps of 52 ha and more (Ramage et al. 2017; Kokelj et al. 2015a; Lacelle et al. 2015; Günther et al. 2015). Individual RTS are local, small-scale disturbances but often occur in regional clusters that then impact the surrounding landscape drastically by affecting topographic gradients and sediment transport (Kokelj et al. 2013; Mu et al. 2020), water quality (Kokelj et al. 2005), coastal erosion (Lantuit and Pollard 2008; Ramage et al. 2017) and carbon cycling (Cassidy, Christen, and Henry 2017; Turetsky et al. 2020). Commonly observed RTS growth rates range from meters to tens of meters

per year (Kokelj and Jorgenson 2013). Increasing permafrost thaw due to climate change is predicted to intensify their thaw dynamics (Lantuit and Pollard 2008; Segal et al. 2016; Lantz and Kokelj 2008). Their combined impact on landscapes and biogeochemical cycling and the abruptness of their rapid development make RTS a highly important permafrost disturbance feature that require better monitoring and prediction capabilities.

Several local remote sensing studies find an acceleration of RTS dynamics by increasing numbers of active RTS, increasing sizes of RTS, and faster headwall retreat rates (Lewkowicz and Way 2019; Ramage et al. 2017; Ward Jones, Pollard, and Jones 2019), a development indicating intensified permafrost thaw and landscape degradation. Previous RTS studies covered a range of local to regional spatial extents and annual to decadal temporal resolutions. Commonly, RTS dynamics were estimated using very high resolution remote sensing imagery for limited local spatial extents from a selected number of points in time, allowing assessment of individual or a cluster of few RTS (Ardelean et al. 2020; Balser, Jones, and Gens 2014; Lantuit and Pollard 2005; Lantuit and Pollard 2008; Lantz and Kokelj 2008; Luo et al. 2019; Segal et al. 2016; Séjourné et al. 2015; Mu et al. 2020). Based on manually digitised RTS extents and limited fieldwork, these studies found increasing rates of RTS activity for varying time periods. A key restriction for such analyses is the limited availability of very high-resolution imagery, allowing only small study extents and a low temporal resolution. Manual mapping using high resolution SPOT imagery provided a first regional insights into RTS distribution across a 1.27×10^6 km^2 region in NW Canada (Kokelj et al. 2017). Advancing these approaches, RTS disturbance trends were derived from multi-decadal Landsat image stacks, which help mapping the distribution of active RTS at regional scales in Canada, Alaska, and Siberia (Brooker et al. 2014; Kokelj et al. 2015a; Nitze et al. 2018) and a deep learning algorithm applied to map RTS from very high-resolution images in the Tibetan Plateau (Huang et al. 2020). These first automatic mapping approaches enabled assessments of RTS dynamics at larger scales and results suggest that local permafrost disturbances occurring in regional clusters may have a significant impact on the landscape-scale. Ward Jones et al. 2019 and Lewkowicz and Way 2019 conducted the first high temporal resolution RTS assessments from annual input data for the last or last two decades, respectively. They derived the first results indicating the increase in occurrence and thaw dynamics of RTS at a high temporal resolution from manual RTS digitisation and image assessments and linked these to climatic drivers, advancing our RTS knowledge greatly. Despite this, it sill remains unknown how high temporal RTS dynamics are caused and may shift with climate change at a larger scale, as both studies are restricted to rather local study sites in the High Arctic. To achieve a better understanding of RTS temporal dynamics and for example their potential contribution to the global carbon cycle, more representative, large-scale, high temporal RTS assessments are required.

The aim of this study is to combine two key elements from the previous RTS assessments: firstly, to apply an automatic RTS mapping approach for large-scale assessments, taking into account the diversity of permafrost regions; secondly, to conduct a high temporal resolution assessment, which addresses the year-to-year dynamics of RTS. Our main objective is to assess RTS disturbance dynamics at high temporal resolution in North Siberia. For this, we developed a new adaptation of LandTrendr (LT), an algorithm for automatic time series disturbance mapping and analysis (Kennedy, Yang, and Cohen 2010), and designed a tailored algorithm parametrisation specifically for the assessment of RTS. LT performs pixel-based temporal segmentation of spectral trajectories and identifies break-points of spectral change which indicate a landscape disturbance. The algorithm captures both gradual and abrupt disturbances from annual Landsat mosaics, enabling the quantification and assessment of annual change. An annual resolution of data is appropriate to detect RTS dynamics related to annual thaw cycles and the 30 m spatial resolution is also sufficient to map RTS (Brooker et al. 2014; Nitze et al. 2018). However, for a enhanced spatial and temporal coverage, especially at northern high latitude coastal areas, we here combine Landsat + Sentinel-2 mosaics as

input data for LT, overcoming some of the restrictions of optical remote sensing due to frequent cloud cover in Arctic regions (Runge and Grosse 2020). We assess the applicability and accuracy of our method at local focus sites and derive quantitative annual disturbance dynamics of RTS from 2000 to 2019. Further, we upscale this method to an approximate 8.1 x 10^6 km^2 study region to map the occurrence and distribution of RTS and determine their annual disturbance dynamics for North Siberia.

4.3 Study Area and Methods

4.3.1 Study area

The study area covers the terrestrial northern high latitudes of Siberia, Russia, ranging from Taymyr Peninsula in the West (80° E) to Chukotka in the East (170° W) and roughly from 77° N to 55° N, comprising an area of approximately 8.1 x 10^6 km^2. Based on the geographic location we refer to this extent as North Siberia. The majority of this area is characterised by continuous permafrost, discontinuous permafrost is found only in Chukotka as well as along the southern margins of the study area, where permafrost extent further declines to a sporadic or isolated coverage (Fig. 4.1). Unglaciated areas experienced long-term syngenetic freezing and continuous sedimentation during the Pleistocene, which led to the accumulation of ice-rich periglacial deposits (Kanevskiy et al. 2011). Ground ice volume varies across North Siberia but can reach more than 40 % as in the southern part of the Lena Delta or even up to 80 % in the Yedoma ice complex (Stolbovoi and McCallum 2002; Strauss et al. 2017b). The climate regions are broadly defined by the arctic and boreal zones and varying maritime and continental influences, resulting in a range of sub-regional climatic characteristics (Sayre et al. 2020). Bioclimatic zones in the region range from polar desert to tundra and taiga (Olson et al. 2001). Furthermore, the study area is defined by interior and coastal lowlands and several mountain ranges such as the Central Siberian Plateau, Byrranga, Verkhoyansk, Cherskiy, Kolyma, and Koryak mountains, as well as the major river systems of the Khatanga, Anabar, Olenek, Lena, Yana, Indigirka, Kolyma, and Anadyr (Fig. 4.1).

A total of nine focus sites are used for the methodological set-up, especially calibration and validation, but also for in-depth result analysis. The focus sites cover the extent of the study area and represent varying geologic, geomorphologic, climatic and vegetational conditions. Table 4.1 lists the focus sites and gives insights into the specific ecosystem characteristics.

Table 4.1: Focus site locations and their characteristics. Mean annual air temperature (MAAT) and mean annual total precipitation (MATP) are derived from ERA5 data copernicus2017era5.

Focus site	Coordinates (centre)	Site characteristics	MAAT Jan /Jul [°C]	MATP [m]
Lower Lena	69.1 °N, 124.5 °E	inland, hilly-mountainous, Yedoma, Taiga	-36.5 / 14.9	0.032
Iultinsky	67.7 °N, 176.5 °W	coastal, lowland, Tundra	-25.1 / 7.1	0.040
Chukotka	65.1 °N, 172.1 °W	coastal, lowland, Tundra	-19.9 / 9.0	0.052
East Taymyr	75.6 °N, 113.6 °E	coastal, lowland, Yedoma, Tundra	-28.6 / 3.8	0.028
West Taymyr	73.3 °N, 86.9 °E	coastal, hilly, Tundra	-27.1 / 8.1	0.043
Kolyuchinskaya Bay	66.7 °N, 174.4 °W	coastal, lowland, Tundra	-21.5 / 5.2	0.048
Chokurdakh	70.6 °N, 147.9 °E	coastal, lowland to hilly, Yedoma, Tundra	-33.9 / 10.2	0.024
Batagay	67.6 °N, 134.8 °E	inland, hilly to mountainous, Yedoma, Taiga	-41.9 / 15.7	0.021
Southwest Verkhoyansk Mountain Range	67.1 °N, 125.6 °E	inland, lowland, Yedoma, Taiga	-36.2 / 14.9	0.049

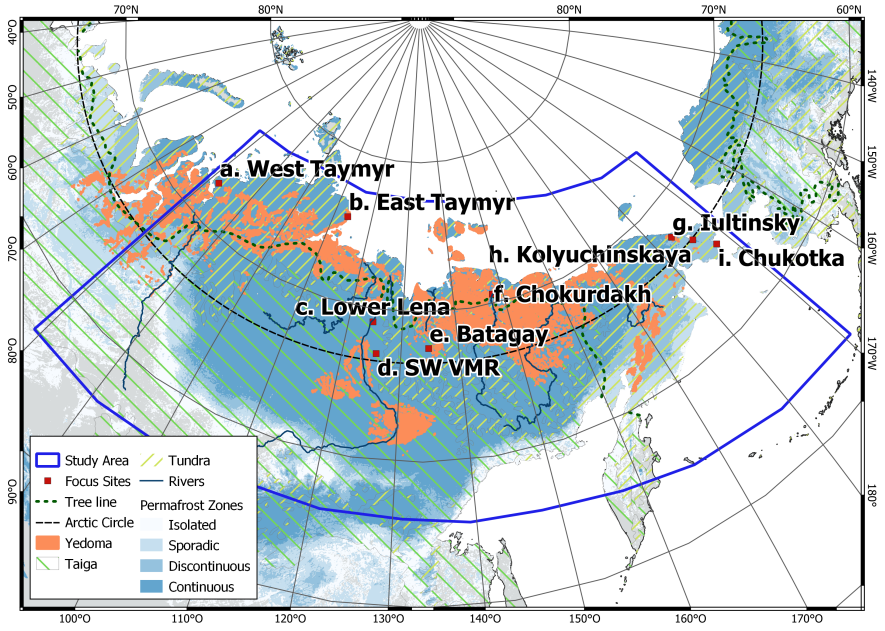

Figure 4.1: Overview of the study area and focus sites across North Siberia. From West to East: a. West Taymyr, b. East Taymyr, c. Lower Lena, d. Southwest Verhoyansk Mountain Range, e. Batagay, f. Chokurdakh, g. Iultinsky, h. Kolyuchinskaya, and i. Chukotka. Permafrost zones according to Obu et al. 2019, Yedoma extent according to Strauss, Laboor, Fedorov, et al. 2016 ecosystem according to Olson et al. 2001 and rivers from Natural Earth Data kelso2010introducing.

4.3.2 General workflow and ground truth data

LandTrendr (LT) was originally developed and designed to detect and capture forest disturbances. Therefore, we had to parametrise the algorithm to be applicable for RTS disturbance dynamics. This comprises several individual steps, which required continuous calibration and validation. Ground truth (GT) data is sparse in North Siberia and only few RTS clusters are known so far. We therefore concentrated on the focus sites and collected as much GT data as possible for calibration and validation. To achieve robust results we assessed every parametrisation step individually. Figure 4.2 shows the general workflow to adapt LT to LT-LS2 (LandTrendr Landsat + Sentinel-2) and to parametrise LT-LS2 to be applicable to RTS. The individual steps will be discussed in the following sections.

We collected GT data for six focus sites across North Siberia to assess the temporal dynamics of RTS. We obtained very high-resolution (VHR) RapidEye images (5m) (Krischke, Niemeyer, and Scherer 2000) for as many years as available for the focus sites (Tab. 4.2). There are only images available from 2013 onward, which implies that the period 1999-2012 cannot be assessed with RapidEye data as independent GT data. This lack of VHR data is a general limitation for North Siberia and unfortunately reflects how infrequent qualitatively sufficient VHR data is available for this region also from other missions such as SPOT, Pléiades, WorldView and GeoEye prior to 2013. Hence, we make use of the maximum amount of RapidEye data available. We manually digitised multi-temporal RTS extents from the RapidEye images by visualising false-color composites for better RTS identification and with additional guidance of the permafrost region disturbance trend product (PRD) of the ESA GlobPermafrost project (Nitze et al. 2018) and ESRI's VHR satellite basemap (ESRI 2017). The collection of RTS extents shows the RTS size at different times and depicts the RTS development over several years at the six focus sites. Following the development of RTS as indicated by the digitised extents, we defined observation points along central transects through individual RTS, which

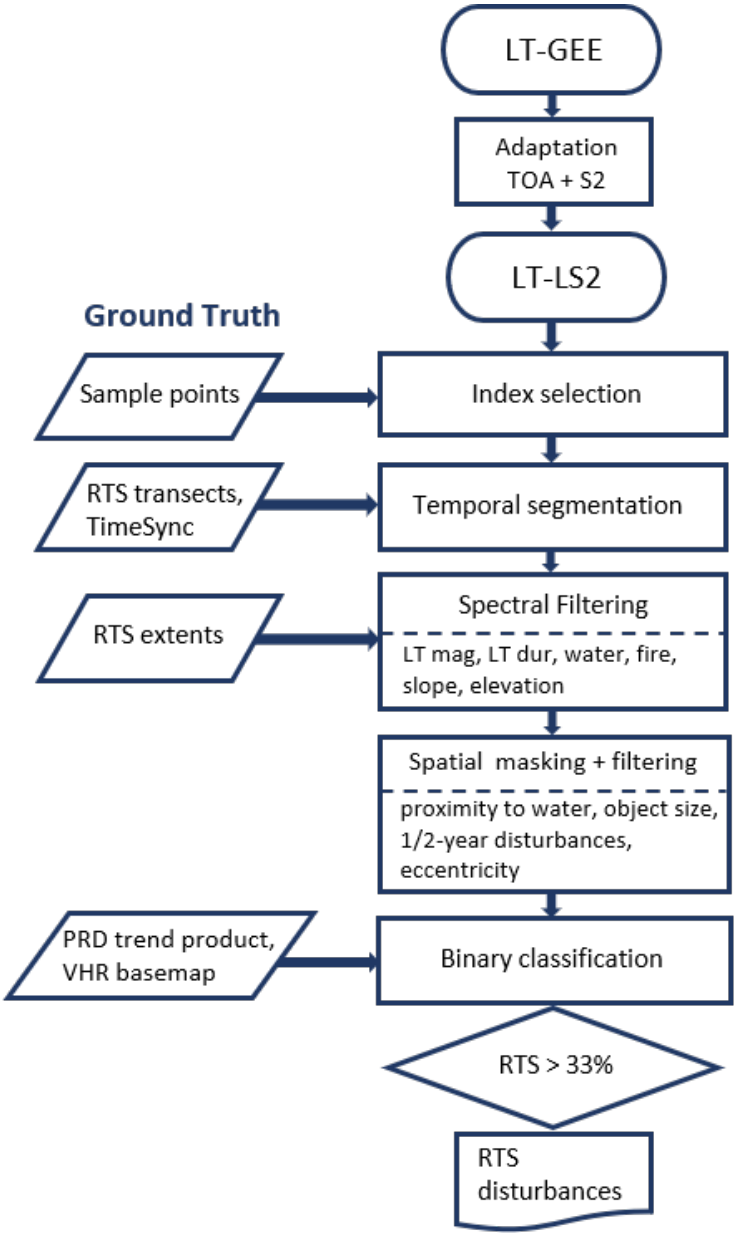

Figure 4.2: Workflow to adapt LT-GEE to LT-LS2 and parametrise the algorithm for retrogressive thaw slump (RTS) assessment.

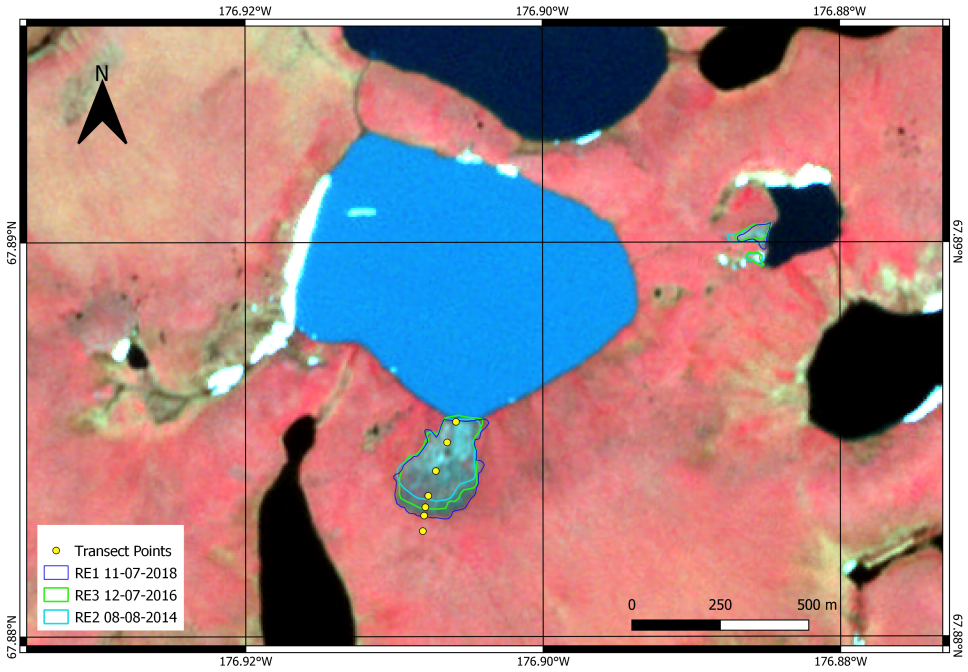

Figure 4.3: The RTS extents at different years and determined observation transect points for an exemplary retrogressive thaw slump on a lake in Iultinsky. The base picture is a false-colour composite of the RapidEye image RE1 11-07-2018. Bluish color of the lake indicates substantial sediment influx from the RTS as opposed to other dark lakes in the surrounding.

are representative for different disturbance years of the slump (Fig. A 4.3) (Brooker et al. 2014).

To assess the extent of RTS at the end of the time series period and to calibrate and validate the spatial filtering and mapping capability of the LT-LS2 algorithm, we manually digitised the RTS extents from the most recent VHR images available to us (Tab. 4.2). For those focus sites where no RapidEye image was available from 2018 or 2019 we therefore obtained additional cloud-free PlanetScope images (3m) (Planet Team 2017).

Table 4.2: Focus sites and very high-resolution image data used for calibration and validation of the temporal segmentation and the spatial mapping step for LT-LS2 parametrisation. R = RapidEye, P = PlanetScope.

Site	Temporal segmentation	Years VHR images (R)	RTS transects	Assessment points	Spatial mapping	Year RTS extent (R/P)
Chukotka	Calibration	2013, 2014, 2016, 2017, 2018, 2019	4	18	Calibration	2019 (R)
Batagay	Calibration	2013, 2016, 2017	4	19	Validation	2018 (P)
Lower Lena	Calibration	2013, 2014, 2016, 2018	4	24	Calibration	2019 (P)
Iultinsky	Validation	2014, 2016, 2018	3	20	Calibration	2018 (R)
Kolyuchinskaya Bay	Validation	2013, 2014, 2015, 2016, 2017, 2018, 2019	4	25	Validation	2019 (R)
Southwest VMR					Validation	2019 (P)

In a second step we used TimeSync for calibration and validation of the run parameters for the temporal segmentation in LT-LS2. TimeSync consists of four components for visual assessment of time series data: (1) annual image chips from the assessment region, in our case the yearly Landsat+Sentinel-2 mosaics (Runge and Grosse 2020), (2) spectral trajectories of observation points extracted from the mosaic time series, (3) Google Earth window with recent and past high-resolution images for a general overview, and (4) an assessment database for result documentation (Cohen, Yang, and Kennedy 2010). For every transect point (Fig.

4.3) we assessed the annual image chips, spectral trajectory and Google Earth history images to visually identify the timing of RTS disturbance, greatest disturbance segment, and the temporal segmentation of the overall spectral trajectory accordingly. As output of the manual TimeSync assessment, we recorded the year of disturbance (GT YOD) for every transect point. We used the GT results of Chukotka Coast, Batagay and Lower Lena for calibration of the LT-LS2 temporal segmentation ('run parameters'), and Iultinsky, and Kolyuchinskaya Bay for validation (Tab. 4.2).

In a last step we conducted a binary machine-learning classification to further remove abundant false positive objects. Based on the LT-LS2 disturbance detection results, we created a training and validation data set, by manually labelling all identified objects into either RTS (label id 1) or no RTS (label id 0) for the focus sites Lower Lena, Iultinsky, Chukotka, West Taymyr, and Chokurdakh. For identification of the disturbance objects, we used again the PRD and ESRI's VHR stellite basemap (Nitze et al. 2018; ESRI 2017). Table 4.3 gives an overview of the identified RTS for validation for each focus site.

Table 4.3: The identified RTS in the disturbance data set for training of the machine-learning algorithm.

Study Site	Number of RTS
Chukotka Coast	53
Iultinsky	66
Lower Lena	71
West Taymyr	116
Chokurdakh	206
Total	512

4.3.3 Data and LandTrendr

Landsat and Sentinel-2 images are the input for this time series assessment as they together have the densest and longest continuous multi-spectral high resolution image archive. Their combined increased image acquisition frequency ensures good data coverage in northern high latitudes despite frequent cloud cover (Li and Roy 2017), which is required for high-temporal time series analysis. In this assessment we are adapting and applying the LandTrendr (Landsat-based detection of Trends in Disturbance and Recovery) algorithm (Kennedy, Yang, and Cohen 2010). LandTrendr captures disturbance dynamics at high temporal resolution while only requiring annual mosaics as input, which is attainable in northern high latitudes by combining Landsat and Sentinel-2 (Runge and Grosse 2020). LT is fully integrated on Google Earth Engine (GEE) as LT-GEE (Kennedy et al. 2018) and we followed the established workflow for adaptation.

We filtered the full archives of Landsat (Thematic Mapper (TM), Enhanced Thematic Mapper Plus (ETM+) and Operational Land Imager (OLI)) and Sentinel-2 (MultiSpectral Instrument (MSI)) top-of-atmosphere (TOA) image collections for North Siberia by image acquisition dates from 1999 to 2020 and for the peak-growing season months, July-August. Constraining the data to peak growing season reduces seasonal variations in reflectance values and ensures spectral comparability of land covers between years independent of phenological phases. An initial cloud cover filter, less than 80 %, was included as a first image quality criterion, as cloud coverage is an issue in Arctic regions and reducing the image selection to cloud-free images improves the overall assessment quality. Additionally, we masked cloud and cloud shadow pixels based on the provided pre-processed metadata information for both image products (Landsat band: BQA (CFMASK), Sentinel-2 band: QA60 (adapted CFMASK)) to

ensure data quality. Lastly, we applied spectral band transformations from MSI to OLI (Runge and Grosse 2019) and OLI to ETM+ data (Roy et al. 2016a) for spectral harmonisation and temporal continuity across the different sensors in the time series. The filtered, masked and harmonised image collections were input for a combined annual mosaicking process. We applied the medoid mosaicking function (Flood 2013), which produces cloud-free, good quality and seasonally representative annual mosaics in Arctic-Boreal regions (Runge and Grosse 2020). With these consistent annual mosaics we ensured temporal continuity in the time series and therefore had a robust input for the LT-LS2 assessment. Since we extended the input database to also include Sentinel-2 images and rely on TOA data as opposed to surface reflectance in the original LT-GEE algorithm, we will refer to the adapted algorithm as LandTrendr Landsat + Sentinel-2 (LT-LS2) to avoid confusion.

4.3.4 Index selection

RTS can be mapped from multi-spectral data as there are distinct spectral differences between the RTS ground dominated by bare or sparsely vegetated, disturbed soils and wet mudflows and the surrounding undisturbed vegetated landscape (either tundra or forest). In a multi-spectral time series, we expect to detect the change in reflectance values from undisturbed vegetation to disturbed ground (Fig. 4.4). To determine the multi-spectral index, which captures this spectral change in the time series most reliably, we conducted a comparative analysis of six indices: the normalized difference vegetation index (NDVI) (Rouse et al. 1974), normalized burn ratio (NBR) (Key and Benson 2005), normalized difference moisture index (NDMI) (Wilson and Sader 2002), and the tasseled cap transformation indices greenness (TCG), brightness (TCB), and wetness (TCW) (Huang et al. 2002). At three focus sites, Lower Lena, Batagay and Iultinsky, we assessed the sensitivity of the indices to distinguish between pre-disturbance, RTS disturbance and post-disturbance in a time series (Quintero et al. 2019; Yang et al. 2018). The TCG and NDVI showed the clearest differentiation between the three stages in a spectral time series compared to the other indices, representatively depicting the indices for the focus site Lower Lena (Figure A 4.10). TCG showed more significant differences between pre-, post- and the RTS disturbance year, while the variation in NDVI was more subtle. We therefore proceeded with TCG as the assessment index, which is also in accordance with the RTS mapping study by Brooker et al. 2014.

4.3.5 Temporal Segmentation

LT-GEE is primarily a time series segmentation algorithm that determines disturbance events and change trends from spectral trajectories on a pixel-basis. The spectral temporal trajectory is extracted from the time series of medoid mosaics and based on individual spectral bands or indices. From a sequence of break-point and straight segment analysis steps, the temporal segmentation is derived which describes the temporal spectral trajectories more simplistically and eliminates noise from the time series (Fig. 4.4) (Kennedy, Yang, and Cohen 2010). This segmentation process is controlled by a set of run parameters. Relating this to RTS disturbances, the segment with the greatest change that describes a loss of vegetation in the time series depicts the landscape disturbance.

The temporal segmentation process requires eight run parameters constraining the algorithm to achieve the best fitted temporal trajectory representation of the disturbance. To identify the most suitable run parameters for RTS disturbances we defined the range of possible values for each parameter based on recommendations defined by the algorithm developers and previous adaptations (Tab. 4.4) and compared the different temporal segmentation outputs

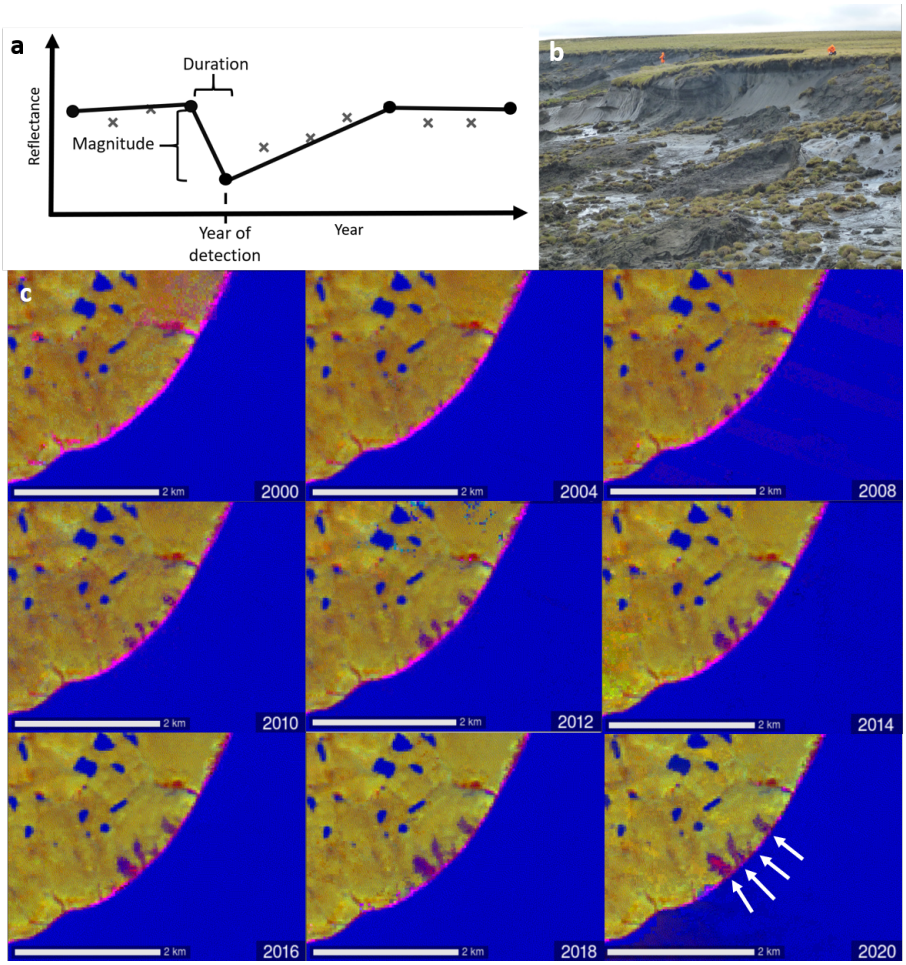

Figure 4.4: Retrogressive thaw slump detection by LandTrendr. a. LandTrendr temporal segmentation schematic, indicating the year of detected disturbance from change in spectral magnitude and disturbance duration. b. Picture of coastal thaw slumping at Bykovsky Peninsula (129.2 °E, 71.5 °N) in 2014 (G. Grosse). Note persons for scale. c. Thumbnails indicating the development of RTS (white arrows in 2020) at the coast of Chukotka (172.2 °W, 64.6 °N) 2000-2020. Illustration based on a TCB/TCG/TCW visualisation in the LT-GEE Time Series Animator App (J 2020).

to the GT data (Section 4.3.2). In total we ran 48 LT-LS2 temporal segmentations for each calibration site and extracted the year of disturbance (LT-LS2 YOD) for the greatest loss segment for each observation point. We calculated an error matrix between the GT YOD and LT-LS2 YOD for all temporal segmentation runs at each focus site and recorded the overall accuracy and Pearson's correlation coefficient to determine the best fitting temporal segmentation run and its corresponding run parameters. The segmentation results with the highest Pearson's correlation coefficient and overall accuracy were not the same for each focus site but showed tendencies of the individual parameters. We therefore compared the runs with the highest scores and picked the run parameters with the highest agreement between sites and run options (Tab. 4.4). The selection of run parameters are in agreement with recommendations from Kennedy et al. 2010 and their sensitivity assessment for a successful LT set-up.

Table 4.4: List of necessary LT-LS2 run parameters for the temporal segmentation algorithm, indicating all tested values and eventually selected values (in bold) for processing. Standard values were chosen for vertex count overshoot, minimum observations needed and one year recovery prevention.

Run parameter	Values
Max segments	3, **4**, 6
Spike threshold	**0.75**, 0.9
Vertex count overshoot	3
Recovery threshold	**0.25**, 0.5
Best model proportion	**0.75**, 1.0
Pval	**0.05**, 0.1
Minimum observations needed	6
Prevent one year recovery	True

The results from the comparison between GT YOD and LT-LS2 YOD show that the LT-LS2 temporal segmentation depicts the progression of annual temporal dynamics of RTS well. We assessed the LT-LS2 temporal segmentation results using the run parameters indicated in table 4.4 to compare GT YOD and LT-LS2 YOD for the RTS observation transects and extended the assessment to two independent validation sites. The Pearson's correlation coefficient between GT YOD and LT-LS2 YOD show an agreement of up to 0.98 for individual RTS transects (Chukotka 1 and 4, Iultinsky 2, 3 and Kolyuchinskaya Bay 1), which verifies that the LT-LS2 temporal segmentation parametrisation captures the progression of the RTS thaw dynamics at an annual temporal resolution (Tab. 4.5). Individual transects show little agreement between the GT YOD and LT-LS2 YOD data (Lower Lena 1 and 2, Iultinsky 1, Kolyuchinskaya Bay 2 and 3). A visual assessment showed that this is mainly due to individual faulty data points in the temporal spectral trajectories. These resulted from irregularities in the mosaics, for example from ETM+ scan-line errors in earlier years or from individual invalid pixels, which deviated from the expected temporal trajectory while all immediate neighboring pixels in the LT-LS2 data set represented the GT data more closely. Hence, overall LT-LS2 captures and depicts the dynamic development of RTS well. Further, we derived the mean deviation and standard deviation between absolute GT and LT-LS2 identified years of disturbance for the transect observation points to evaluate the precision of detected disturbance year 4.5. Transects marked with an asterisk contained transect observation points, which were disturbed before the time series assessment period (first transect point) and were therefore excluded from the analysis. The mean deviation ranges from -4.4 to +3 years for Kolyuchinskaya Bay transect 3 and Lower Lena transect 1, respectively. Half of the mean values demonstrate that LT-LS2 YOD values are later compared to the GT YOD, which shows a delay in disturbance recognition in the LT-LS2 analysis. Contrary to this, negative mean values illustrate that LT-LS2 implies a disturbance

earlier than the GT YOD data set. An issue is probably that by a spatial resolution of 30 m we have to account for mixed pixels, which delay the detection of a disturbance, as the multi-spectral data only recognises the disturbance when bare soil dominates the mixed pixel. The assessment shows no clear trend on whether LT-LS2 identifies RTS disturbances rather too early or delayed but that we have to account for inaccuracies of approximately ±2 years for the disturbance year of LT-LS2.

The overall parametrisation results show a good fit and promising first results indicating that LT-LS2 captures annual dynamics of RTS as anticipated. With this parametrisation we ran LT-LS2 for the full study area of North Siberia and generated LT-LS2 change images for the greatest change segment. Six bands describe the disturbance at every pixel: 1) magnitude of spectral change, 2) year of disturbance, 3) duration of disturbance, 4) pre-change spectral value, 5) rate of spectral change, and 6) DSNR as a fit metric.

Table 4.5: Assessment of the LT-LS2 temporal segmentation based on the GT YOD and LT-LS2 YOD transect observation points. The first value is the Pearson's correlation coefficient indicating the general level of agreement between GT and LT-LS2. The second value is the mean deviation between the absolute GT YOD and LT-LTS YOD value and the third the standard deviation, demonstrating the error in absolute year of disturbance in the temporal segmentation. For transects marked with an asterisk we excluded the earliest transect point for the mean and standard deviation.

Step	Site	All transects	Transect 1	Transect 2	Transect 3	Transect 4
Calibration	Chukotka Coast	0.63 / -0.3 / 2.6	0.65 / 1* / 1.4	0.40 / -1.3 / 2.8	0.98 / -2 / 2.1	0.95 / 2* / 1.2
	Batagay	0.78 / 0.8 / 3.3	0.8 / 1.7* / 0.9	0.66 / 2.8* / 1.9	0.81 / -2.8 / 3.4	0.76 / 2.5* / 1.2
	Lower Lena	0.23 / 0 / 3.9	0.22 / 3* / 5.1	0.14 / 1.5 / 1.4	0.81 / 1.8 / 0.7	0.59 / -1.7* / 4.6
Validation	Iultinsky	0.49 / -0.13 / 3.9	0.06 / -1.5* / 6.2	0.90 / 2.3* / 1.8	0.92 / -0.7 / 1.8	
	Kolyuchinskaya Bay	0.40 / -2.1 / 5.3	0.97 / -0.4 / 1.0	0.05 / -1.4* / 5.4	0.05 / -4.4 / 6.7	

4.3.6 Spectral Filtering

The majority of spectral change captured in the temporal segmentation is not RTS disturbance or change-related but due to general spectral change and trend, other landscape disturbances such as wildfires or lake drainage, erroneous pixels (cloud, haze, fire smoke) or other artefacts. To remove small spectral change not associated to RTS disturbances, we filtered the temporal segmentation result by applying thresholds to the LT-LS2 image bands. To determine the filter thresholds for magnitude of spectral change (mag), duration in years (dur), and pre-disturbance value (preval) that still map RTS but remove other spectral change, we defined possible threshold values (mag: 200, 400, 600, 800; dur: 1, 2, 4, preval: 50, 100, 200) and compared the disturbance mapping results to GT data (Section 4.3.2. We compared the mapped area size of RTS from the 36 spectral filtering options to the GT area size (RTS extents 2019) and chose the threshold combination, which showed the highest correlation to the GT based on the Pearsons' correlation coefficient. With the exception of Chukotka Coast and East Taymyr, the Pearsons' correlation coefficients show high agreement between a dur value of 2 and mag values of 400, 600, and 800 (Tab. 4.6). The preval did not contribute significantly to the spectral filtering and was therefore excluded. A dur threshold of 2 ensures the inclusion of disturbance events that are last at least 2 years which can be expected for RTS. At the same time this threshold excludes short term spectral disturbances, which are most likely related to anomalies, such as longer or earlier snow cover or other changes, as well as pixel artefacts. The best fitting mag threshold varied across the focus sites but as indicated in table 4.6 there is a high correlation between several mag values. The mag threshold is critical to ensure full spatial coverage of the RTS objects. We therefore chose the lower mag

threshold of 400 (Fig Appendix 4.9). While this enhances the RTS object coverage it also leads to high commission errors, including more non-RTS disturbance pixels and noise which has to be removed in the following steps.

Table 4.6: The tested mag and dur values for spectral filtering with the highest Pearson's correlation coefficient for the calibration and validation focus sites .

Site	Magnitude	Duration	Pearson's correlation coefficient
Lower Lena	400	2	0.98
	600	2	0.92
Chukotka	800	2	0.51
	600	2	0.26
	400	2	0.24
Iultinsky	800	2	0.94
	600	2	0.70
	400	2	0.56
East Taymyr	200	2	0.37
	400	2	0.28
Southwest VMR	400	2	0.99
Kolyuchinskaya Bay	800	1	0.99
	600	2	0.97
	400	2	0.95

4.3.7 Spatial masking and filtering

The spectral disturbance signature of RTS is distinct but not completely differentiated from other disturbances, such as wildfires, landslides, changes in river water levels or other. Hence, also the LT-LS2 disturbance map after spectral filtering, despite its explicit parametrisation to RTS disturbances, does not only depict thaw slumping features but includes other, spectrally similar disturbances. To further narrow the LT-LS2 disturbance map to RTS, we applied several spatial masks with additional environmental information. We applied a water mask to exclude permanent water bodies (Pekel et al. 2016), a fire mask which included detected fire scars from 2000 to 2019 (Hansen et al. 2013), a slope mask to only include disturbances on sloped terrain from 3-15° as well as an elevation mask to exclude mountainous regions above 250 m a.s.l. both based on the ArcticDEM mosaic (Porter et al. 2021), a water buffer to only include disturbances in the proximity of lakes, rivers, and coastlines prone to RTS initiation (Pekel et al. 2016), and finally we only included identified disturbances within the the continuous and discontinuous permafrost zones (Obu et al. 2019). Table 4.7 shows an overview of spatial masks and thresholds applied.

Table 4.7: Overview of spatial masks applied.

Mask	Data set	Threshold	Reference
Water	Global surface water data set		Pekel et al. 2016
Fire	Global forest cover change		Hansen et al. 2013
Slope	ArcticDEM	3–15 °	Porter et al. 2021
Elevation	ArcticDEM	<250 m a.s.l.	Porter et al. 2021
Water buffer	Global surface water data set	300m buffer	Pekel et al. 2016
Permafrost	Extent and Ground Temperature	Continuous, discontinuous	Obu et al. 2019

Following the spatial masking on the pixel-level, we performed object-oriented spatial filters to further exclude false-positive disturbances and to restrict the subsequent analysis to RTS disturbances. We identified disturbance objects with scikit-image's connected component algorithm in a 2-connectivity neighbourhood. For every labelled object, we extract feature properties including the object centre coordinates, area, eccentricity, orientation, perimeter, and solidity. Based on the LT-LS2 year of disturbance band, we further derived the minimum year and maximum year of disturbance for every labelled object, representing the disturbance period of that object within the assessment period. Additionally, we filtered all labelled objects by their eccentricity property. We set the eccentricity threshold to > 0.75, which was derived empirically from validating RTS at three focus sites, Lower Lena, Chukotka and Iultinsky. Other object properties, such as orientation, perimeter or solidity did not show a similar trend for separating between RTS and false positives.

Next, we applied an area size filter, defined by a minimum mapping unit (mmu) and maximum mapping unit (maxmu). We set the mmu to 0.0036 km^2 (0.36 ha), which represents 2*2 30 m pixels, a minimum RTS size also suggested by Brooker et al. 2014 for their RTS mapping study from Landsat images. To remove bigger disturbance patches, which are most likely not RTS but 2020 fire scars, remnants of previous fire scars or other extensive disturbances, we set the maxmu to 0.15 km^2. These mapping unit filters still include the general known RTS size ranges as reported in other studies (Lacelle et al. 2015; Lewkowicz and Way 2019; Kokelj et al. 2015a; Lantz and Kokelj 2008; Segal et al. 2016; Ramage et al. 2017).

Lastly, we used the minimum and maximum disturbance year property of every labelled object and removed all objects with a disturbance activity duration of less than two years. The likelihood, that these are RTS, which mostly evolve over multiple years, is very low. Instead it is more likely that these are 2020 fire scars, remnants from previous fire scars, small active layer detachment slides, artefacts or other disturbances not representing RTS.

4.3.8 Machine-learning object filter

The disturbance data set after spatial masking and filtering still contained a high amount of commission errors (false positives). Therefore we included a final binary classification step to classify each remaining disturbance object either as a RTS or other. We used the pycaret (version 2.3) package (A 2020) in python to setup a classification pipeline. As input data we used basic statistics (min, mean, max values) of all LT-LS2 output bands, except "year of disturbance", and Landsat Tasseled Cap Index Trends (slopes of TC brightness, greenness and wetness) per polygon object. In the model comparison Light Gradient Boosting Machine (Ke et al. 2017) came out as the best model, where we used the F1 score as the primary estimator metric. To account for the extreme class imbalance we used the "SMOTE" resampling algorithm (Chawla et al. 2002) implemented in pycaret. We optimised the model and performed a 10-fold stratified cross-validation on the input data set. We used pycaret's built-in model evaluation functionality to determine the best separation threshold between classes, as the initial discrimination was strongly imbalanced with a bias towards the no-slump class. We repeated the cross-validation on a regional basis, training on four tiles and validating on the fifth, rotating through all tiles. We added the regional validation to test the transferability to unseen regions. Finally, we trained the production model on all five ground-truth tiles and ran the inference on the entire study area. The output data set contains final class labels (0 or 1) and class specific probability scores. With this we reduced the false positives of LT-LS2 drastically, which improved the RTS disturbance mapping greatly compared to the purely LT-LS2 automatic algorithm.

The validation results prove the challenging task of mapping RTS on continental scales. 10-fold cross-validation (CV) on the full GT data set without regional differentiation revealed a mean accuracy (statistics of all 10 folds) of 0.9479±0.0106 and kappa of 0.5452±0.1042 (Tab. 4.8). The class specific performance for RTS (class 1) metrics revealed a mediocre performance with a F1 score of 0.609. The higher precision (0.655) compared to recall (0.569) shows a slight bias towards an "underdetection" of RTS. To overcome this bias and to receive a balanced classification we used the "threshold" estimator in pycaret. This revealed an optimum threshold (probability score for class 1) of 0.33 to maximize the F1 score and a threshold of 0.25 for an equilibrium of precision and recall (Fig. A 4.11). The regional cross-validation (5 sites) revealed the challenges of model transferability. RTS class specific F1 score ranged from 0.07 (Lower Lena) to 0.37 (West Taymyr) and therefore lower than a CV on the entire data set (Tab. 4.9). The classification bias, as observed on the full CV, was more diverse in the regional CV. Three of five regions have a higher recall, while only two exhibit an excess in precision.

Table 4.8: Overall 10 fold cross-validation. Mean and standard deviation of scores from all 10 folds.

	Accuracy	**AUC**	**Recall**	**Precision**	**F1**	**Kappa**
Mean	0.9479	0.9014	0.4846	0.6765	0.5622	0.5355
Standard Deviation	0.0106	0.0172	0.1025	0.1034	0.1013	0.1061

Table 4.9: Regional Cross-validation (RTS class only).

Site	**Precision**	**Recall**	**F1**	**Support (n objects)**
Chukotka	0.45	0.27	0.34	48
Iultinsky	0.28	0.34	0.30	56
Lower Lena	0.04	0.44	0.07	61
Chokurdakh	0.38	0.18	0.24	212
West Taymyr	0.63	0.26	0.37	110

4.4 Results

4.4.1 Focus sites

For five focus sites we mapped RTS and assessed their annual thaw dynamics in detail to demonstrate the capability and applicability of our method. The focus sites comprise a square area of 625 km^2 and represent known RTS clusters. The number of identified RTS varies at the focus sites and demonstrates differing RTS densities (Tab. 4.10). Chukotka presents a coastal site with many active RTS along the coastline. Here, as the RTS grow retrogressively, neighbouring RTS merge together and form bigger RTS objects with time. At Iultinsky and Lower Lena we identified RTS at lake shores and often 2-3 RTS at one lake. Both focus sites are located at the border of the Last Glacial Maximum (LGM) glacial ice extent in Siberia and are close to areas with ice-rich Yedoma deposits (Fig. 4.7). The other two focus sites, West Taymyr and Chokurdakh, also feature RTS at lake shores but often with more than 3 RTS at a lake. Chokurdakh is special, as not only individual RTS developed but complete lake shores erode. Here, LT-LS2 often identified multiple individual RTS, for the more active erosion parts of the shore. Chokurdakh is characterised by extensive Yedoma deposits, whereas West Taymyr is located within pre-LGM glacial moraine complexes. The minimum RTS size with 0.45 ha was found at Iultinsky, Chukotka and Chokurdakh and is determined by the predefined minimum mapping unit. The biggest identified RTS is in Chukotka with 14.94 ha, the limit

set up the maximum mapping unit. While the mean RTS size for the sites ranges from 1.4-4.8 ha. In West Taymyr the average RTS activity duration is 11.8 years compared to 15.2 years in Chukotka. The initial RTS-affected area in 2000 per focus site varies greatly (Iultinsky: 5.9 ha, West Taymyr: 69 ha) and likewise does the increase in RTS affected area from 2001-2019. The RTS-affected area in Iultinsky, West Taymyr and Lower Lena increased by 188 %, 144 % and 141 %, respectively. In contrast, the area increase of only 73 % was much lower for Chokurdakh.

Table 4.10: Overview of identified RTS for the focus sites (625 km^2) and all of North Siberia. The number of identified RTS, average slump size and the average slump activity duration (last - first year of disturbance pixel) are based on the identified RTS objects. The summarised slump area for 2000 and the summarised slump area from 2001-2019 are compiled from all RTS pixels in a focus site. The summarised area from 2001-2019 percentage indicates the area growth compared to the RTS area in 2000. The peak growth years are the two years with the highest RTS area in the time series. *The initial RTS area was derived from 2000 and 2001.

Site	Number of RTS	RTS min/mean/max [ha]	Average slump activity duration [yr]	RTS area in 2000 [ha]	RTS area from 2001-2019 [ha]/[%]	Average growth/year [%]	Average growth/RTS [%]	Peak growth years ([ha])
Lower Lena	18	0.72 / 2.34 / 6.2	13.7	17.5	24.6 / 141	7.4	7.8	2013 (3.9), 2015 (3.7)
Iultinsky	9	0.45 / 1.9 / 8.46	11.9	5.9	11.16 / 188	9.9	20.9	2008 (2.61), 2009 (1.53)
Chukotka	9	0.45 / 4.83 / 14.94	15.2	19.5	23.9 / 123	6.5	13.6	2016 (5.4), 2007 (2.97)
Chokurdakh	64	0.45 / 1.4 / 7.56	12.3	50.9	36.9 / 73	3.8	1.1	2009 (6.03), 2011 (5.58)
West Taymyr	88	0.45 / 1.9 / 11.8	11.8	69.0*	99.5 / 144	7.6	1.6	2016 (43.2), 2013 (20.5)
North Siberia	50,895	0.45 / 1.7 / 14.94	12.3	20,158	66,699 / 331	17.4	0.007	2019 (9,669), 2016 (7,136)

We determined the dynamic progression of RTS by identifying the first and last year of slump activity within the assessment period for each identified RTS and by resolving the summarised RTS affected area per year, indicating the annual RTS growth as depicted in figure 4.6. The first year in the assessment period, 2000, comprises not only newly disturbed RTS area in 2000 but also the accumulated dynamics from previous years before our time series starts (Fig. 4.5). Although we can derive the average RTS growth for each year or for every RTS (Tab. 4.10), the annual RTS area analysis shows that the increase in RTS area is not uniformly during the observation period but that distinct years with accelerated RTS area growth can be determined. Iultinsky had two periods of increased slump activity, 2008-2010 and 2015-2018, with the highest RTS area growth in 2008 (Fig. 4.5 d). Similarly, did West Taymyr also show two periods with increased slump activity, 2005-2006 and 2012-2017. The RTS affected area in Lower Lena increased in 2008 and lasted until 2017, with the exception of 2014. About 60 % of the RTS slumps in West Taymyr showed their last activity in 2016-2017 (Fig. 4.5 c), which is either the peak slump year (2016) or one year later (2017). This suggests that the heightened slump activity was caused by a temporary trigger. There is little new RTS initiation during the assessment period in Iultinsky and Lower Lena alike and more than 80 % of the identified RTS were active since 2000. Most of the RTS had their last slump activity in the second half of the time series, specifying higher slump activity during the last two decades in Iultinsky and Lower Lena compared to West Taymyr. Chokurdakh und Chukotka show very similar annual RTS-affected area trends as Iultinsky and Lower Lena. The results show an alternation between time periods of high RTS activity and less RTS development during the observation period (Fig. A 4.12).

4.4.2 North Siberia

Within our study area of approximately 8.1 x 10^6 km^2 covering North Siberia from Taymyr Peninsula to Chukotka, a total number of 50,895 RTS were identified and mapped. The

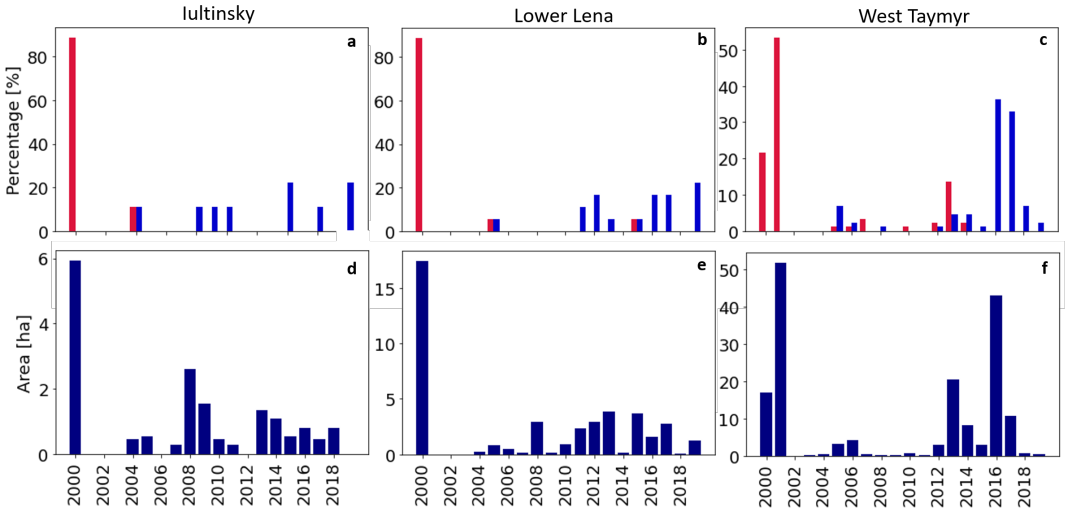

Figure 4.5: The first year of RTS activity (red bar) and last year of RTS activity (blue bar) for Iultinsky, Lower Lena and West Taymyr on the top panel (a-c) and the annually summarised RTS areas for the same sites below (d-f).

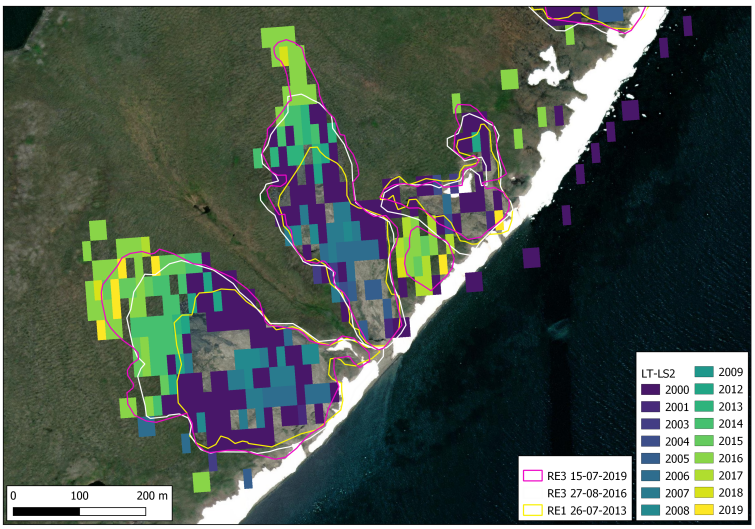

Figure 4.6: Annual progression of RTS in Chukotka (172.2 °W, 64.6 °N), showing the year of disturbance for every pixel. Digitised RTS extents from RapidEye images are indicated.

majority of RTS was found between 61-73 °N (Fig. 4.8 b). This RTS abundance is highly related to the uneven latitudinal land mass distribution in the study area. There is less land area north of 72 °N, which also explains the decrease in number of RTS. Similarly to this, the lower latitudes in the East of the study area (140 °E, 55-60 °N) cover less land mass, which explains the lower geographic boundary of identified RTS. Figure 4.7 shows the geographic density of identified RTS for 40km x 40km grid cells. The majority of RTS were identified in the continuous permafrost zone. Where the permafrost extent becomes discontinuous, sporadic or isolated permafrost, RTS occurrence and density decrease as well. Furthermore, the RTS density map reveals clusters of RTS between 80-90 °E in the West of the study area, between 140-160 °E and north of 65 °N and along the border of the LGM glacial ice extent in Siberia (Ehlers and Gibbard 2003). The abundance of RTS along the margins of the LGM glaciation is most likely associated to degrading buried glacial ice in moraines (Barr and Clark 2012; Kokelj et al. 2017). Moreover, the occurrence and density of RTS correlates closely with the distribution of thick ice-rich Yedoma permafrost deposits that are particularly vulnerable to thermokarst and thermo-erosion processes such as RTS (Fig. 4.7) (Strauss et al. 2017b; Strauss, Laboor, Fedorov, et al. 2016). A high density of RTS can be found in central Yakutia near Yakutsk, a known hot spot region for permafrost degradation and thermokarst development (Séjourné et al. 2015; Ulrich et al. 2017). In contrast to this, we also identified vast areas with no or low RTS densities across North Siberia, most notably in mountainous regions and the central West of the study area.

The normalised area frequency plot (Fig. 4.8 d) illustrates that the vast majority of identified RTS are small and close to the predefined minimum mapping unit. 50 % of all identified RTS are smaller than 1.17 ha and 90 % of the RTS are smaller than 3.42 ha, which indicates that the normalised area frequency is positively skewed. The proportion of bigger slumps is much lower. This positively skewed distribution of RTS object size can be explained by common RTS characteristics and by detection limitations of LT-LS2. First, RTS are rather small-scale disturbance features, with commonly reported sizes of 0.4-5.3 ha (Lacelle et al. 2015; Segal et al. 2016), which our results show as well. RTS exceeding this size by far, so-called mega slumps, occur but are less common. Secondly, RTS are polycyclic which is another reason for the predominance of smaller identified RTS objects. RTS often alternate between periods of active degradation and periods of stabilised dormancy, which can differ spatially with only part of a stabilised RTS re-initiating, depending on slumping drivers and environmental factors such as remaining ice content, exposure of the ice, the sloped terrain, drainage and sediment transport, and climatological conditions (Balser, Jones, and Gens 2014; Kokelj et al. 2009). The stabilised part of a RTS cannot be detected by LT-LS2 as the temporal spectral signature of these areas does not resemble a disturbance trajectory and therefore is not captured by LT-LS2. LT-LS2 only detects the actively degrading RTS areas, which might not be the full extent of a RTS. Likewise, LT-LS2 can only capture disturbances occurring within the assessment period (1999-2020). The first captured year of the time series, 2000, contains an accumulation of the most recent disturbances, approximately from 1997-2000, but disturbance events from before cannot be accounted for and therefore only the actively degrading part and not the whole RTS size can be determined by LT-LS2. Therefore, we consider our findings of RTS numbers and areas conservative low.

Most slumps had their first active year at the start of the assessment period with almost 50 % and 25 % in 2000 and 2001, respectively (Fig. 4.8 a). The remaining RTS had their first activity year in the course of the time series until 2016 but no new RTS initiations were detected in 2017-2018. About 25 % of the RTS had their last slump activity in 2019, which is the end of the time series. However, a bigger proportion of about 30 % of the RTS deceased slumping already before the end of the assessment period, namely in 2016-2018. The overall summarised RTS affected area increases steadily during the time series, illustrating extended RTS growth and development. Heightened increase rates were determined for 2016, 2017 and

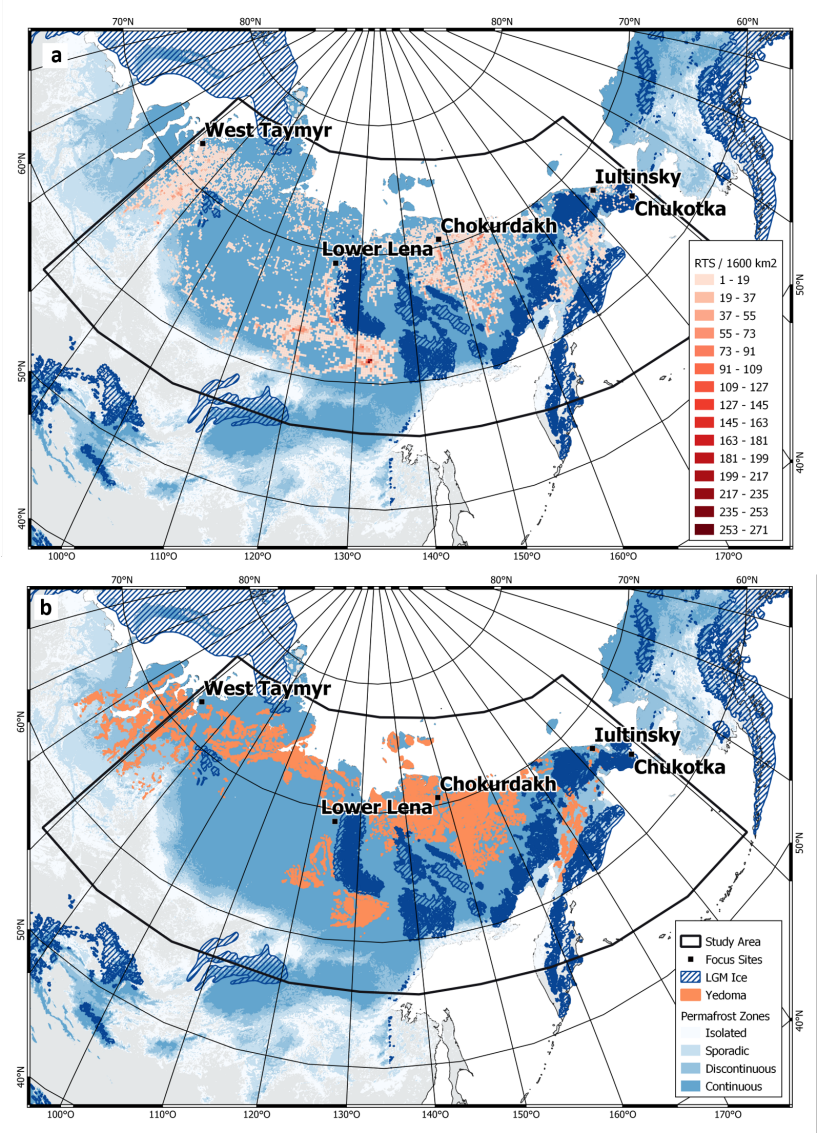

Figure 4.7: a) Density map of identified RTS per 40 km x 40 km grids in North Siberia. b) The permafrost zones are according to Obu et al. 2019, the Last Glacial Maximum (LGM) glaciation ice extent according to Ehlers et al. 2003 and the Yedoma distribution according to Strauss et al. 2016.

2019. From 2001-2019 the RTS affected area increased by 331 % compared to 2000, which shows a drastic increase in area affected by permafrost degradation in only 19 years (Tab. 4.10). Combining these results, we can determine, that the increase in RTS-affected area at the end of the time series is not caused by newly or re-initiated RTS but most likely by RTS growth of already existing and active RTS. Furthermore, the high number of inactive RTS in 2016-2018 (last year of activity), suggests that the increase in RTS area is not necessarily caused by successive thaw, which would prevail for a longer time period, but by explicit triggers in those years. Whether these RTS remain inactive and stabilise for a longer period cannot be derived from this assessment.

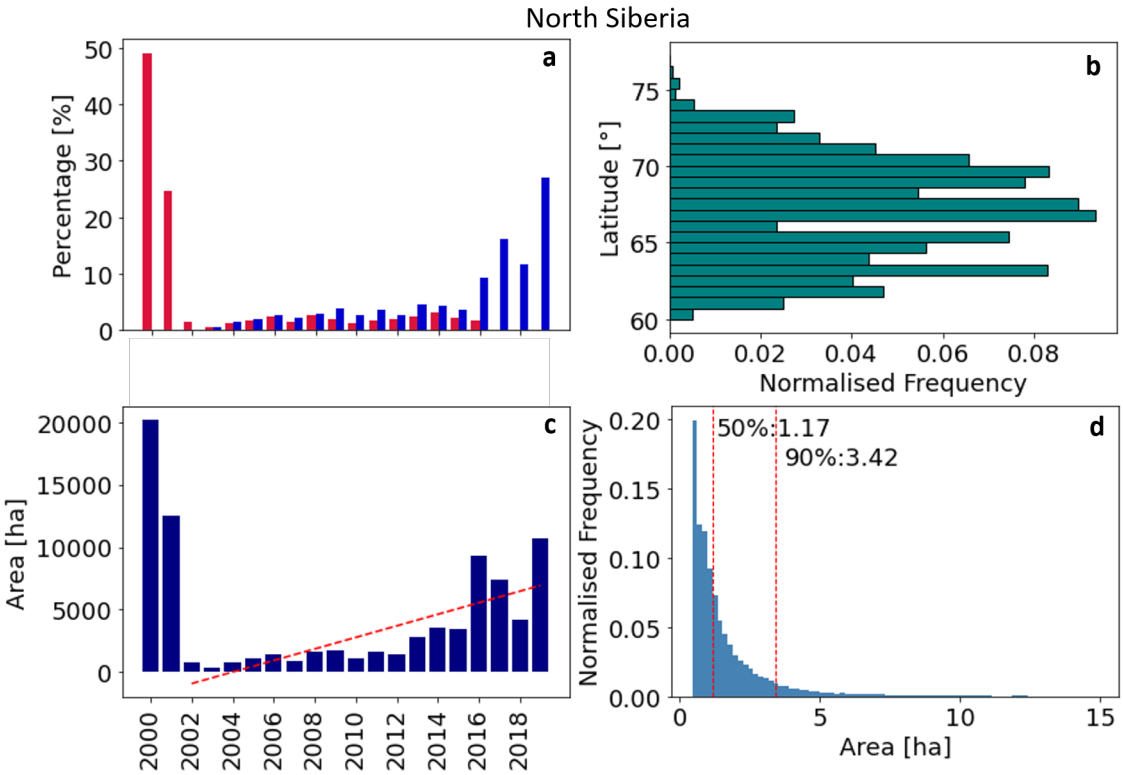

Figure 4.8: Identified and mapped RTS in North Siberia: a. First year (red bar) and last year (blue bar) of RTS object activity; b. Normalised frequency of RTS by geographic latitude; c. Summarised annual RTS area [ha] with trend line indicating an increase in area from 2002 to 2019 with a slope of 374 ha per year; d. Normalised frequency of RTS object sizes.

4.5 Discussion

4.5.1 Mapping of RTS

The results obtained in this study on RTS are overall in agreement with previous studies. The mean size of identified RTS ranges between 1.4 ha (Chukordakh) to 4.8 ha (Chukotka), which exceeds the RTS sizes recorded by previous studies slightly, stating average RTS sizes of 0.15-1.63 ha (Ramage et al. 2017; Lewkowicz and Way 2019). The range of mega slumps, 3.8-9.9 ha, as stated by Kokelj et al. 2015, is mirrored by maximum RTS sizes of 6.2-11.8 ha (Chukotka even 14.94 ha) in this assessment. This indicates that LT-LS2 is well suited to identify RTS across very large regions. Furthermore, we found a strong correlation between the detection of RTS and environmental factors. RTS generally occur in clusters in ice-rich permafrost areas, mostly from glaciogenic deposits or syngenetic permafrost, along sloped terrain and in proximity to lakes, rivers and coasts, where climatic conditions drive their development (Kokelj and Jorgenson 2013; Kokelj et al. 2017; Ardelean et al. 2020). Our results also show that the majority of the RTS and the highest RTS density can be found in the proximity to the LGM glacial ice extent (moraine complexes) and in areas with thick ice-rich Yedoma deposits, emphasising that the primary determining factor for RTS is ice-rich permafrost. The RTS density distribution underlines the vulnerability of ice-rich permafrost to abrupt thaw and furthermore, the threat of rapidly mobilizing increased amounts of sediment and organic carbon over short periods of time (years) in icy permafrost regions experiencing thaw.

4.5.2 Spatio-temporal variability of RTS dynamics

Between 2000-2019 we detected 50,895 RTS and a steady increase in RTS affected area for North Siberia. From 2016 onward we detected a more abrupt increase in RTS affected area, which indicates heightened thaw slump dynamics at the end of the observation period. Overall, the RTS-affected area increased by 331 % between 2001-2019 (from 20,158 ha in 2000 to 66,699 ha), confirming the projected intensification and growing impact of abrupt permafrost thaw (Nitzbon et al. 2020; Turetsky et al. 2020). The majority of RTS was active at the beginning of the time series, 2000-2001, and only a smaller number of newly initiated RTS was detected in the course of the observation period. This suggests that the increase in RTS affected area is predominantly driven by growth of existing RTS and not by initiation of new slumps, as also shown by Lewkowicz and Way 2019 for the Canadian High Arctic. However, the spatial resolution of 30 m and the applied minimum mapping unit prevent to detect smaller scale changes, such as RTS initiation at higher spatial resolution. Therefore, we emphasise again that most likely we underestimate the number of actual RTS as well as the RTS affected area. In contrast to the steady increase of RTS-affected areas for North Siberia, the focus sites showed differing annual variability in the RTS thaw dynamics, indicating spatio-temporal variability of RTS thaw dynamics. All five focus sites do not show a uniform year-by-year development of RTS area but distinct periods of increased and decreased thaw dynamics. The peak slump years and periods vary between focus sites, which further confirms a strong connection to spatio-temporal varying slump drivers and environmental triggers, which lead to exposure of ice-rich ground, increased thaw, drainage and sediment transport during the thaw period. Such assessments of a high spatial variability in RTS activity and dynamics could only be addressed in limited ways by previous high temporal resolution assessments focusing more on local to regional study extents in the Canadian High Arctic or on the Qinghai-Tibet Plateau (Lewkowicz and Way 2019; Ward Jones, Pollard, and Jones 2019; Luo et al. 2019).

Lewkowicz and Way 2019 correlated their annual detection of growing RTS and newly initiated RTS mainly to warm summer years on Banks Island. A similar relationship was found by Ward Jones et al. 2019 for their Canadian High Arctic study sites on Ellesmere and Axel Heiberg Islands. Besides this, Kokelj et al. 2015 linked increased slumping activity to heavy precipitation events and downward sediment fluxes for the more southern study area of the Peel Plateau, in NW Canada. All these studies point towards the strong correlation between climatic and environmental drivers and RTS activity. The annual variability of RTS dynamics at the focus sites point at spatio-temporally varying thaw triggers that cause the increased slump dynamics in some years. Following this, we correlated the yearly affected RTS area to climate variables. We derived the mean temperature, the total annual precipitation, the total precipitation for July and August and the number of thawing days from ERA5 reanalysis data for the focus sites (Copernicus Climate Change Service 2017). However, we found no significant correlation between these climate variables and the annual RTS area, but only varying tendencies for the different focus sites. Lewkowicz and Way 2019 and Kokelj et al. 2015 pointed out a temporal lag of one or two years between the occurrence of reinforcing thaw drivers and actual increased permafrost thaw and RTS development. Therefore, a closer analysis of possible climate drivers and annual RTS dynamics is required to identify the spatio-temporal RTS drivers at the different focus sites, but outside the scope of this study. Overall, combining the results from the focus sites and North Siberia, we can imply that the steady increase in RTS-affected area in North Siberia results from spatio-temporal variability of RTS thaw dynamics at local to regional scale. This emphasises the heightened relevance of abrupt permafrost disturbances at the continental scale but without underestimating the importance of local to regional assessments when it comes e.g. to infrastructure planning or other site-specific analyses. The impact of advancing permafrost degradation by rapid RTS development on local-scale is very pronounced in changing topographic gradients, hydrological systems, and biogeochemical cycling and can largely be considered irreversible. Most numerical

permafrost models do not yet include rapid thaw processes. However, in a recent modeling study for the cold and ice-rich permafrost regions of Northeast Siberia, which were previously thought to remain largely stable despite gradual warming, (Nitzbon et al. 2020) included thermokarst dynamics for the first time and found the landscape to be considerably affected by permafrost degradation already by 2100. Current carbon models show that by 2300 abrupt permafrost thaw disturbances will occur on less than 20 % of the permafrost region, but their carbon contribution will be of global relevance due to their rapid and deep erosion of ice-rich permafrost (Turetsky et al. 2020). The combination of this high carbon release potential and the abrupt and widespread thaw process by RTS, also discovered in this assessment for North Siberia, make RTS a highly important disturbance feature.

4.5.3 LT-LS2 capabilities and limitations

LT-LS2 identifies disturbances from temporal segmentation of spectral trajectories. The accuracy of the temporal segmentation showed that the progression of the year-to-year thaw dynamics of RTS are captured well, with correlations up to 0.98 between LT-LS2 temporal segmentation and GT data. Yet, this correlation varies and depends on good quality input data as seen for few GT transects. By using medoid mosaics combining both Landsat and Sentinel-2 we enhanced the input database greatly (Runge and Grosse 2020), similarly to approaches for MODIS time series ingesting both Aqua and Terra images (Sulla-Menashe et al. 2014). However, even Landsat and Sentinel-2 mosaics might not succeed in providing full spatial and temporal coverage in cloud-prone areas, such as northern coastal and high Arctic areas. Besides this, Sentinel-2 images are only available since 2016 for Siberia and before that we rely on Landsat-only mosaics. Thus, we assessed a possible correlation between input data and affected RTS area. For the focus sites we derived the average number of cloud-free pixels for each year, which is an indicator for the input mosaic quality as the likelihood of obtaining consistent and gap-free mosaics increases with the number of cloud-free pixels. Although the number of clear pixels increased drastically with Sentinel-2 in 2016 for all focus sites, we did not find a correlation between the average yearly clear-pixel count and identified RTS-affected area. This suggests that there is no bias between detected RTS area and enhanced mosaic coverage at the end of the time series, but it rather implies reliable disturbance detection throughout the assessment period. This is in contrast to findings from a study on cropland change, where the image availability and detection of cropland changes showed a correlation (Dara et al. 2018). However, cropland changes and abandonment are largely gradual changes, which are further distorted by land cover phenology and outliers that are more likely and pronounced in low quality input mosaics (Dara et al. 2018). Compared to this, the detection of RTS disturbances is based on determining and extracting the biggest disturbance segment, following abrupt, drastic spectral change. This method is more robust to shifts in phenology and outliers, which might arise in Landsat-only mosaics in years with few cloud-free images and affirms reliable disturbance detection also for the first 15 years in the time series.

Despite the vigorous temporal segmentation of RTS dynamics, insecurities on the definite year of disturbance remain and a deviation of approximately ± 2 years has to be taken into account. While this lowers the confidence for explicit year of disturbance associations, the 20-year time series assessment is still able to depict peak periods of abrupt thaw. Furthermore, the accuracy of the annual dynamics is affected by the 30 m spatial resolution of the input data. Small scale initial disturbances of only a few meters width will not be captured by 30 m spatial resolution, which will result in a delay of detecting RTS initiation and early growth and is therefore considered a low-resolution bias (Sulla-Menashe et al. 2014). A delay of detection can further be perpetuated by thaw slumping processes where the vegetation cover and hence the spectral land cover reflectance remains intact while the soil column already

subsides or erodes underneath. Contrary to this, the identification of a disturbance can be premature if other changes precede the RTS disturbance, such as vegetation change, active layer detachment slides or flooding of lake or river shores.

In spite of the reliable detection of temporal RTS dynamics with LT-LS2 at local-scale, the application at large-scale required further attention as we encountered high commission errors. The spectral-temporal segmentation included a variety of false-positives, such as remnants of fire scars, lake change and drainage, changing water levels and sediment transport in rivers, shadows in mountains and other commissions. The difficulty to detect and map RTS at large-scale and to separate from false positives has been discussed before and was solved by a final manual RTS confirmation (Nitze et al. 2018). This was possible for us at the focus sites but not for the large-scale North Siberian application. Hence, a rigorous post-classification of the identified disturbance objects was necessary to reduce the amount of false positives and narrow the analysis to RTS disturbances. Considering that RTS are very local, small-scale features, the amount of training and validation data, compared to the false positives was very low and sparsely scattered across North Siberia as qualitative VHR data is only infrequently available for North Siberia. Also, prior studies of detailed local RTS assessments are very sparse in this large study region (e.g., Sejourne et al. 2015). This sparseness in high-resolution data decreases the LT-LS2 RTS classification accuracy to a F1 score of 0.609 for RTS. At the same time, the LT-LS2 classification reduced the overall number of identified disturbance objects drastically. We are confident that final RTS mapping and analysis of RTS across North Siberia, represents a reasonable and fitting framework for a first continental-scale assessment at high temporal resolution.

The RTS distribution and density map indicates local and regional RTS clusters, closely related to climatic, geologic and topographic conditions. The use of VHR imagery and assessment methods can therefore now be regionally targeted and used for a high spatial resolution assessment of RTS in the future, provided the availability of VHR data. Multi-sensor constellations such as RapidEye and PlanetScope acquire images at increased rates and high spatial resolution, which increases the likelihood of obtaining high quality images. This could confirm and narrow the identified RTS objects in conjunction with the high temporal resolution assessment presented here as well as enhance the identification of initiation and small scale changes. So far, the long time series of high temporal high spatial resolution cannot be replaced by VHR data but a combination of both will enhance the detection of small scale changes. Similarly, the development of new improved mapping methods, such as deep learning algorithms, may help achieving a high mapping accuracy. For example, RTS in Tibet were mapped using deep learning techniques with CubeSat images at high spatial resolution, which ensured a more accurate estimation of RTS-affected area but is currently still limited to local study sites and only short assessment periods (Huang et al. 2020).

4.6 Conclusion

Our study includes the adaptation of the LandTrendr algorithm to capture the rapid permafrost disturbance dynamics of RTS at high temporal resolution in a first continental-scale assessment across North Siberia. Parametrisation of LT-LS2 by extending the data input to Landsat and Sentinel-2, adjustment of the temporal segmentation, and adaptation of the spectral and spatial masking parameters allowed us to identify and map RTS. While ground truth is sparse, we aimed to thoroughly assess and parametrise the individual workflow steps with high-resolution data available, resulting in a reliable and robust assessment framework for high temporal RTS analysis. Our assessment showed an overall steady increase in RTS-affected area

in the 8.1 x 10^6 km^2 study region and highlights the abundance and rapid dynamics of abrupt permafrost thaw processes in ice-rich permafrost landscapes. Local focus-site assessments indicated spatio-temporal variability of RTS thaw dynamics. These patterns and year-by-year processes can only be detected at high temporal resolution and would be missed by low temporal resolution assessments and trend analysis. It is apparent that RTS do not develop uniformly but are caused by varying drivers. The data set with annual resolution of RTS thaw dynamics now allows for a detailed assessment of thaw slumping drivers. Our study covered heterogeneous permafrost regions with varying climatic, geologic, geomorphological and vegetational conditions, which are also common in other regions of the pan-arctic. In our rather short time series covering 19 years (2000-2019), we observed an increasing impact of abrupt permafrost disturbances on the landscape. Considering that numerical models project increasing permafrost thaw due to climate change and strong Arctic warming also in very ice-rich permafrost regions, we assume that this observed trend will continue further.

Code and Data products:
The LT-LS2 RTS disturbance data set will be provided on PANGAEA for public access.

Acknowledgments:
We thank Sophia Barth (AWI) for delineating RTS extents, Cornelia Zygar (AWI) for a first framework for LandTrendr parametrisation, and Ulrike Herzschuh and Birgit Heim for constructive discussions of this research. Lastly, we thank Google for providing access to the Google Earth Engine resources and R. Kennedy and his team for providing the original LandTrendr algorithm and thorough documentation.

4.7 Appendix

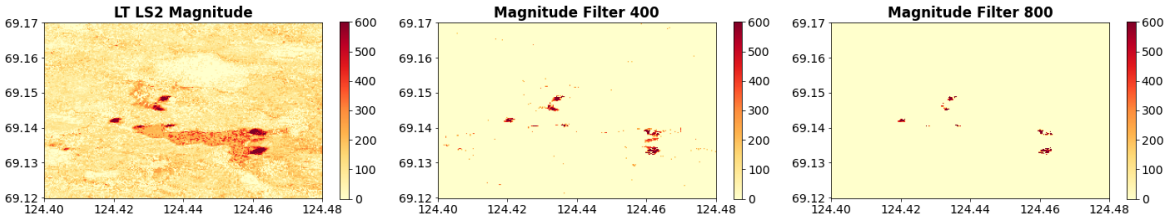

Figure 4.9: Spectral filtering example of a close-up at the focus site Lower Lena. The dur threshold is set to 2 and the mag threshold varies from 400 (middle panel) to 800 (right panel). The dark red areas show RTS along lakes.

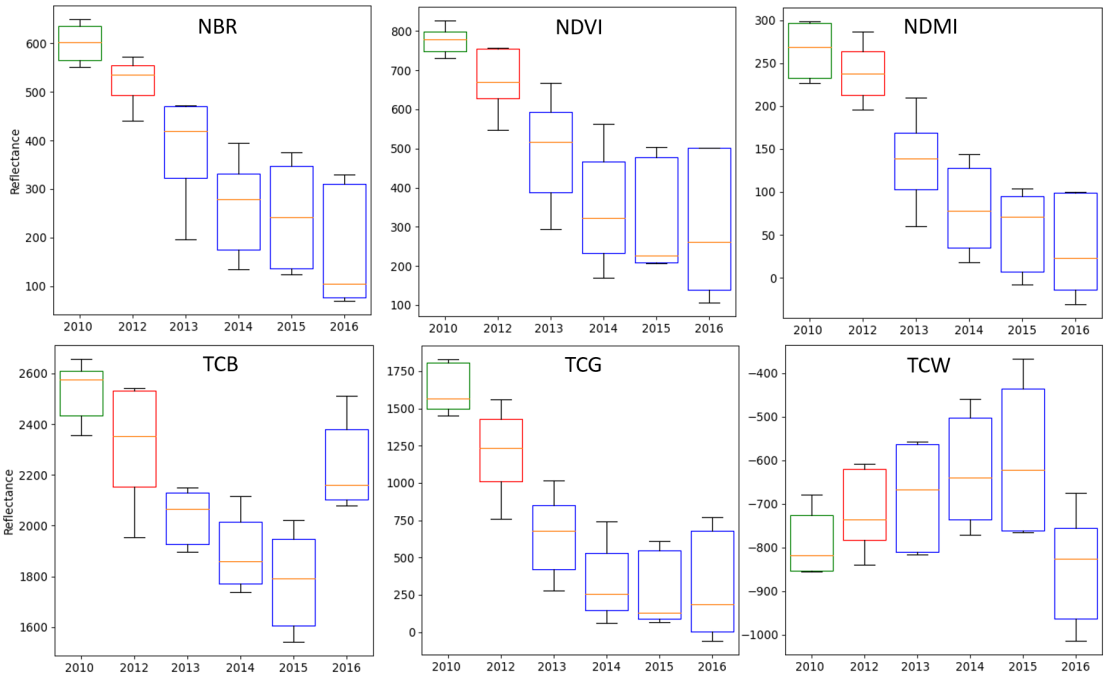

Figure 4.10: Spectral indices for pre-disturbance (2010), disturbance (2012) and post-disturbance (2013-2016) years for the focus site Lower Lena. Boxplots illustrate the spectral reflectance dynamics from representative RTS disturbance pixels.

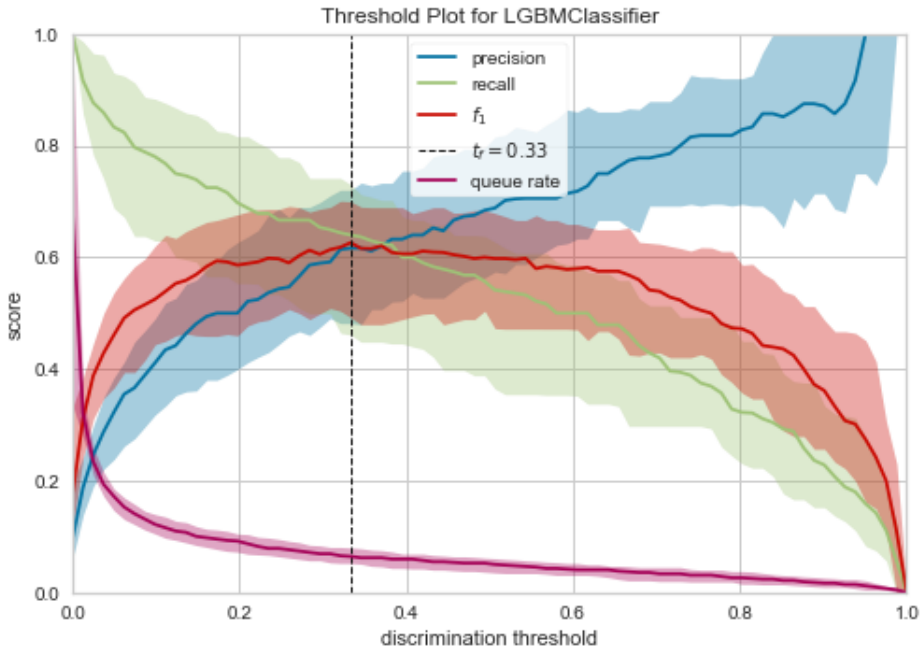

Figure 4.11: "Threshold" estimator in pycaret for the classification model.

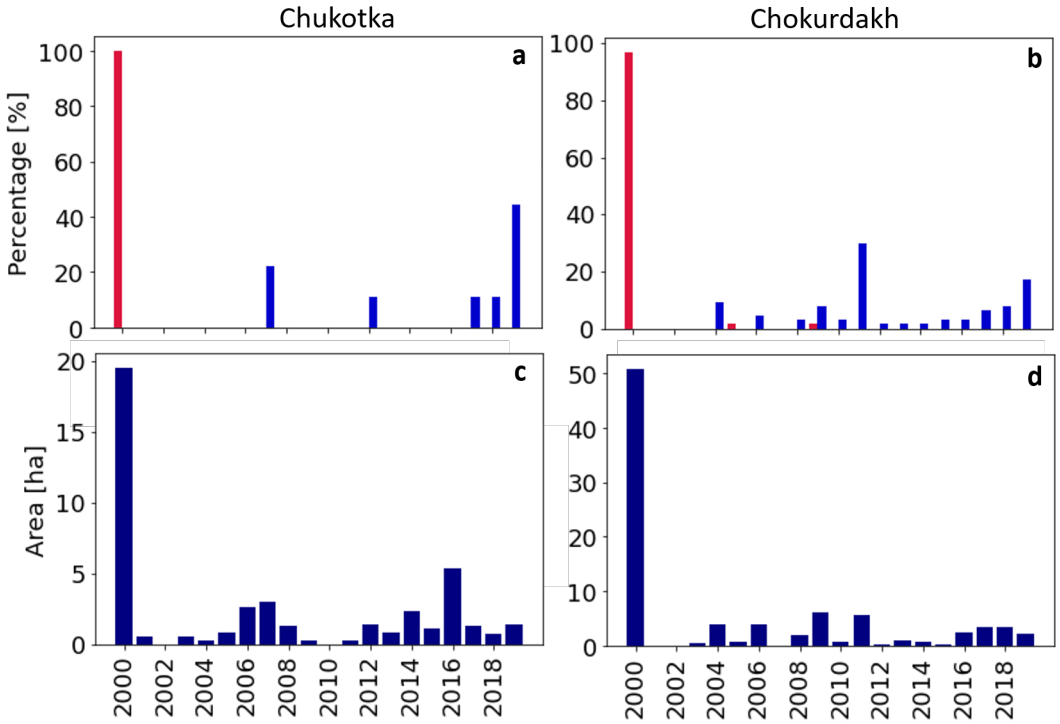

Figure 4.12: Specific results of RTS dynamics for the focus sites Iultinsky, Lower Lena, and West Taymyr.

5

Synthesis and Discussion

The main objective of this dissertation thesis was to develop automated high spatial and temporal resolution remote sensing methods that advance our knowledge and understanding on the spatial extent and temporal dynamics of abrupt permafrost disturbances on the regional to continental-scale with remote sensing.

While permafrost thaw and its contribution to the carbon cycle are increasingly recognised as relevant components for Earth System Models, there is still a lack of consistent observation products with spatially and temporally continuous and high resolution data on the abundance, distribution, and especially the temporal dynamics of abrupt permafrost thaw disturbances. Of particular interest are retrogressive thaw slumps, which might only be local, small-scale permafrost disturbance features but have a significant relevance for local and regional topographic gradients, hydrological pathways, sediment and nutrient mobilisation into aquatic systems, and permafrost carbon mobilisation as they deeply and rapidly erode ice-rich and organic-rich permafrost soils. However, key research gaps so far include the lack of studies on RTS distribution and dynamics beyond the local to small regional scale and the absence of temporally high resolution assessments of their development on decadal scales. The recent development of automatic mapping algorithms for regional to large-scale landscape change assessments as well as the availability of high temporal resolution remote sensing data sets that allow capturing the highly dynamic thaw processes in time series analysis now provides the opportunity to resolve these knowledge gaps.

Therefore, this thesis presented new methods to enhance and expand the remote sensing database for abrupt permafrost disturbances by combining images from two sensors systems for temporally dense time series studies in northern high latitudes. It further demonstrated the adaptation of an automated mapping and disturbance assessment algorithm that captures high temporal change dynamics. Lastly, it introduced a large-scale RTS disturbance assessment, from consistent multi-spectral time series analysis, which highlighted spatio-temporal variability of RTS thaw dynamics at high temporal resolution. The following synthesis discusses the main findings of this research as they relate to the objectives outlined in section 1.2.

5.1 Google Earth Engine

This dissertation has highly profited from cloud-based processing and computing facilities, available to the general public at no cost. I conducted all my analyses on Google Earth Engine (GEE), which hosts a multi-petabyte remote sensing data archive, ranging from image repositories (multi-spectral, active), climate reanalysis data, prepared data products, such as forest or water change data sets, and thematic geospatial data.

Being able to access and process analysis-ready data instantly, allowed me to explore new assessment options easily. I considered this to be very helpful not only while designing the project but also in the course of the research to double check results, compare differing workflows and algorithm performances as well as consult additional data sets for further and more informed interpretation. The open-code policy and active GEE-developer community helps to quickly seek out help and support in case of code errors or when further explanation concerning a data set or algorithm is necessary. The fast reply times of GEE-developers is monumental.

There are unequivocal many and diverse advantages of cloud-based computing and big data earth observation approaches that they enable, which the scientific community will benefit greatly from. However, there are also a number of limitations as discussed by Sudmanns et al. (2020) and grouped according to technology, data processing, data access, and applications and users. In the line of this, I would like to address a limitation I encountered. While GEE accesses and displays a huge amount of images instantly, creates best-pixel mosaics or performs supervised machine-learning algorithms in no time, in-depth assessments which go beyond these standard operations, such as robust statistical result analysis are still limited, impractical, especially for large-scale assessments in GEE. Especially, after performing several adaptation and transformation steps, as required when combining Landsat and Sentinel-2 for large regions I ran into memory-issues when attempting to perform further assessments. Reason for this is that GEE main image processing options run on the back-end, however further project-defined adaptations are performed ultimately in the front-end, which is restricted in computing and processing performance and therefore limits the possibilities and algorithm applications related to verifying output, image processing performance, statistical comparisons or such greatly. This is a big disadvantage for scientific applications, as they require more vigorous validation. While the non-expert user group grows exponentially, it is important to ensure also scientific verification options. Hence, the continuous development to improve statistical analysis and validation algorithms for user-defined projects is essential and fundamental for GEE to maintain a strong remote sensing expert user group. I still think that the advantages outweigh this and other disadvantages but for future development efforts should address this as it would increase the opportunities for the scientific community vastly and avoid having to perform initial processing and analysis in GEE and then continue and finish in a different analysis environment, such as Python or R, as I had to.

5.2 Landsat and Sentinel-2

Several environmental factors highly restrict optical remote sensing applications in northern high latitudes. The biggest limitations are low illumination angles, polar night during winter, short summer periods and frequent cloud cover, which deteriorate the image quality and acquisition coverage. In contrast to this, Synthetic Aperture Radar (SAR) sensors are not restricted by weather and these environmental factors as their active sensing systems penetrate cloud cover and operate independent of illumination conditions (Wang et al. 2018). Therefore, a SAR system delivers images reliably and throughout the whole year, which in terms of temporal coverage is much superior to optical remote sensing (Jorgenson and Grosse 2016). Thus, SAR methods have been developed frequently in recent years and also been adapted

for permafrost landscape changes, fostering crucial advances in permafrost landscape change detection and monitoring with more assessment progress to be anticipated in the coming years (Bartsch et al. 2016; Short et al. 2014; Strozzi et al. 2018). However, the biggest disadvantage to this day, is the mostly short and irregular acquisition time period of individual SAR missions so far, which do not allow for consistent multi-decade time series analyses yet (Torres et al. 2012). Thus, optical remote sensing systems provide the longest continuous database for time series analysis currently, despite their acquisition limitations in the northern high latitudes.

In this dissertation, I conducted a spectral comparison between Landsat and Sentinel-2 multi-spectral images for a combined use in temporally dense time series analysis. The major benefit of a combined use of Landsat and Sentinel-2 is their improved data acquisition scheme with a combined revisit time of less than 2.9 days globally, which is further increased in the northern high latitudes (Li and Roy 2017). This high image acquisition rate increases the likelihood of obtaining good quality, cloud-free images during the short summer period greatly. The absolute number of acquired images increased drastically with the addition of Sentinel-2 in 2016, since two Sentinel-2 sensors operate simultaneously, with a combined revisit time of 5 days at the equator. This is also reflected in an increased number of available cloud-free pixels (Chapter 2 and 3). Therefore, a temporally dense image database can be obtained from combining spatially high resolution Landsat and Sentinel-2 imagery in northern high latitudes, which cannot be achieved from other sensor systems, such as MODIS, AVHRR, Worldview, SPOT, or others, at a comparable temporal and spatial coverage, or at a similar high spatial resolution, which is required to detect and monitor local-scale changes.

Detecting environmental land surface change and shifts in ecosystems based on multi-spectral assessments is sensitive to and can be impacted by spectral and radiometric deviations and artefacts. Therefore, spectral continuity and high agreement between spectral properties of different sensors is required, to avoid sensor-based biases in a combined assessment. While same-day Landsat-8 and Sentinel-2 images for three study sites across the Arctic-Boreal permafrost region showed a general good concurrence between the two sensors' spectral bands, I conducted a detailed spectral band comparison and derived bandpass adjustment coefficients. The pixel-based assessment of overlapping same-day images, showed small differing responses between the corresponding band-pairs, which would lead to irregularities in multi-spectral assessment such as interpretations derived from multi-spectral indices, e.g. normalized difference vegetation index, to address ecosystem properties like greening and browning. The spectral band adjustment of Sentinel-2 to Landsat-8 established a very close fit between the two sensors, which reduces the sensor-bias. Overall this assessment proved to be suitable for the visible, near-infrared and short-infrared band-pairs alike. The results indicate the possibility to achieve a strong spectral agreement between Landsat-8 and Sentinel-2 after spectral bandpass adjustment in North Siberia and therefore suggest a seamless application of Landsat and Sentinel-2 images in a combined time series study. The derived bandpass coefficients facilitate the possibilities for new combined Landsat and Sentinel-2 assessments at high northern latitudes which can rely on a strengthened combined database from Landsat and Sentinel-2 together.

This enhancement has also been indicated by other local and regionally-focused Landsat and Sentinel-2 studies (Mandanici and Bitelli 2016; Vuolo et al. 2016; Gorroño et al. 2017; Li et al. 2017; Flood 2017) and furthermore also by a globally available harmonized Landsat and Sentinel-2 data product (Claverie et al. 2018). While the application of a globally available product would show consistency beyond individual studies, the assessment in chapter 2 also points out the shortcomings of such a product for a regional-specific application. The regionally-derived bandpass adjustment coefficients outperformed the globally harmonised product and generated a better fit between Landsat-8 and Sentinel-2 data in North Siberia. Assessments with a global focus might neglect this discrepancy and accept small regional

deviations for the benefit of a globally-consistent analysis. However, in this case, I am concentrating on an assessment for a specific region that is geographically restricted to the northern high latitudes. Thus, the regionally-fitted bandpass adjustment coefficients address the region-specific challenges better as presented in chapter 2 and provide an enhanced database for future analyses in North Siberia.

My research demonstrates the general comparability and compatibility of Landsat-8 and Sentinel-2 for North Siberia but most importantly delivers bandpass adjustment coefficients for a transformation of Sentinel-2 spectral reflectance values. This ensures spectral data continuity between Landsat and Sentinel-2, which is highly important to reliably assess ecosystem changes at high spatial resolution and further advances our knowledge on climate-induced and disturbance-related changes. While the Landsat archive has been used extensively to determine spatio-temporal ecosystem change in Arctic regions, a common limitation is the differing spatial coverage of Landsat images for large-scale assessments (Pastick et al. 2019; Sulla-Menashe, Woodcock, and Friedl 2018; Nitze and Grosse 2016; Lara et al. 2018). Being able to combine Landsat and Sentinel-2, with a high spectral comparability, reduces the imbalance in spatial coverage, while maintaining a high spatial resolution to determine spatio-temporal variability of landscape dynamics.

As Sentinel-2 images are only available since 2016 for Siberia, the increase in data availability only accounts for the last 5.5 years, which is a short time period compared to Landsat's image archive. However, since the publication of the first study of this dissertation in 2019, already data of another year can be added to the time series and this will continue as both NASA and USGS, as well as ESA have committed to their Earth observation programs in the future. Hence, the relevance of spectral adjustment between Sentinel-2 and Landsat will increase with the continuous image acquisitions of both sensor systems.

5.3 Image mosaics and disturbance detection algorithm

While expanding the remote sensing database for assessments in northern high latitudes was a central step towards high temporal resolution assessments of abrupt permafrost disturbances, a second crucial step was the adaptation of an automatic mapping and assessment algorithm. The restriction of previous RTS studies to a low temporal resolution and local assessment extent was not only due to lack of data but also the absence of a scalable automatic assessment method. Manual digitisation of RTS extents or visual interpretation is very time and labour intensive and therefore neither feasible for high temporal time series nor suitable for continental-scale assessments. Therefore, this dissertation focused on adapting an automatic high temporal disturbance detection algorithm.

LandTrendr (LT), the algorithm for Landsat-based detection of trends in disturbance and recovery, captures gradual and abrupt disturbances in high temporal time series. LT seemed to be fitting for abrupt permafrost disturbances for two reasons. Firstly, LT comprises an annual temporal assessment resolution, which is a suitable temporal resolution for RTS, as their disturbance dynamics highly rely on the annual thaw and freeze cycle in the Arctic. Secondly, LT requires annual mosaics as input, which is comparatively little input for high temporal resolution output in contrast to other change detection algorithms, which demand more frequent input, such as CCDC (Zhu and Woodcock 2014) or BFAST Monitor (Verbesselt, Zeileis, and Herold 2012). While we expanded the input database greatly by combining Landsat and Sentinel-2, an intra-annual full spatial and temporal coverage would still be challenging. LT strikes the right balance between high temporal resolution assessment and

input data frequency, which can be attained from Landsat and Sentinel-2 in northern high latitudes.

A critical step for a successful LT adaptation and application to abrupt permafrost disturbances is to ensure good-quality input data. Therefore, chapter 3 concentrated on the modified mosaicking approach to combine both Landsat and Sentinel-2 for the annual input mosaics of LT. The evaluation showed the drastic increase of images and cloud-free pixels available for the mosaicking approach with Landsat and Sentinel-2 together, as also pointed out in chapter 2. The foundation of the mosaicking algorithm is the image input collection, which was extended to include Landsat and Sentinel-2 top-of-atmosphere data and comprised the spectral adjustment of Sentinel-2 with the spectral bandpass coefficients (chapter 2). Combining images from both sensors in a medoid mosaic led to an improved coverage for Landsat+Sentinel-2 mosaics, especially at far northern, coastal sites affected by frequent clouds, which could not be achieved by Landsat-only mosaics. In years with increased cloud coverage, Landsat-only mosaics would contain data gaps and decolorisation from bad quality input, whereas Landsat+Sentinel-2 mosaics achieved full spatial mosaic coverage. Lastly, a spectral band comparison between input images and Landsat+Sentinel-2 mosaics showed a close spectral correlation, which testified that the mosaic results are representative, reliable, and of good spectral quality from Landsat and Sentinel-2 images together. This further validates the effectiveness of the spectral bandpass adjustment between Sentinel-2 and Landsat. Consequently, my research emphasises the comparability of Landsat and Sentinel-2 data and their combined strength to facilitate good quality mosaics that achieve both improved spatial and temporal coverage of northern high latitudes in high temporal resolution time series, which is essential for disturbance assessments in Arctic regions.

This Landsat+Sentinel-2 mosaicking approach now allows to create landscape-scale mosaics for spatially consistent high temporal time series assessments in North Siberia. For the first time a spatial and temporal consistent database is available for continental-scale assessments. This is crucial to further our understanding on permafrost disturbance occurrence, frequency, duration, magnitude, and spatio-temporal variability in permafrost regions and advance our knowledge on their main drivers (Kasischke et al. 2013). Increasing the temporal resolution to annual assessments will allow to analyse inter-annual thermokarst lake change and drainage (Jones et al. 2020; Nitze et al. 2020; Olthof, Fraser, and Schmitt 2015), fire occurrence, frequency, distribution, and recovery (Frazier et al. 2018), as well as permafrost landscape erosion such as coastal erosion (Irrgang et al. 2018; Jones et al. 2018), active layer detachment slides (Lewkowicz 2007), and RTS (Brooker et al. 2014; Balser, Jones, and Gens 2014; Kokelj et al. 2015a) with greater temporal detail. In principal, this workflow also allows for intra-annual image mosaicking, which would be required for certain ecosystem and biophysical dynamics such as shifts in vegetation phenology (Beamish et al. 2020; Zeng, Jia, and Epstein 2011) or snow timing (Jan and Painter 2020). However, a detailed image availability assessment for intra-annual time series for these applications would be required, as both vegetation phenology and snow timing necessitate data in spring and autumn, which is more challenging with optical remote sensing.

Being able to combine Landsat and Sentinel-2 data, ensuring spectral continuity across sensors and time periods, as well as an improved data coverage for high temporal resolution analysis completes the foundation of the first RTS high temporal resolution continental-scale assessment. Based on the enhanced image database and the good quality mosaics the application of an automatic change detection and disturbance analysis algorithm is possible for abrupt permafrost disturbances.

5.4 Mapping RTS and their annual temporal dynamics

The enhanced image database and the adapted mosaicking workflow provided the means for high temporal time series permafrost disturbance assessments. In order to include permafrost disturbances in Earth System Models, consistent regional to continental-scale disturbance products are required to take the feedback between climate change and permafrost disturbances into account. Key requirements for large-scale abrupt permafrost thaw disturbance detection is to apply an automated mapping and analysis algorithm at high temporal scale.

The continental-scale assessment of RTS requires a robust parametrisation of LT, to reliably capture and depict the disturbance dynamics of RTS in the time series. In this case we differentiate between the original LT algorithm and LT incorporating the adjusted Landsat+Sentinel-2 mosaics (LT-LS2). LT-LS2 applies a pixel-based temporal segmentation of the spectral trajectory and spectral filtering of the result to confine the assessment to the disturbance feature, which is the foundation of the LT-LS2 assessment. The validation of the RTS LT-LS2 temporal segmentation with GT data, showed a good representation of the successive progression of RTS dynamics on an annual scale by LT-LS2. A comparison of identified disturbance year between LT-LS2 and GT showed a deviation from -4.4 to +3 years with an average +/-2 years. This discrepancy between LT-LS2 and GT has to be taken into account when analysing the annual dynamics of RTS disturbances. While this displays an uncertainty in disturbance year detection, it also signifies that LT-LS2 is able to capture progressive RS dynamics at a high temporal resolution and is able to depict periods of increased and decreased thaw slump development. Validation data from very high-resolution RapidEye and PlanetScope images for known RTS clusters showed that LT-LS2 nicely identifies and maps RTS spatially. However, the separation of RTS to other disturbances and land cover changes in the time series is challenging, both on local and continental-scale, as multiple land surface and ecosystem changes occur simultaneously. Therefore, extensive spatial and spectral filtering, and finally a binary machine-learning classification was required to reduce the LT-LS2 disturbance data set and confine the assessment to only RTS disturbances. This demonstrated that automatically mapping RTS disturbances, especially on regional to continental-scale, is challenging and validation of the results crucial. This applies not only for RTS mapping but also other abrupt permafrost disturbances, such as wildfires, thermokarst lake change and drainage or thermo-erosional gullies and vallies. However, it is especially critical for RTS as they are small-sale, local disturbances and if not well distinguished from other disturbances or errors, the RTS-affected area will be overestimated out of proportion. It is therefore important to keep the ratio between RTS disturbance area and study area in a reasonable range, which is achieved by the additional spatial filtering and classification step in the workflow and hence, improved the automated RTS mapping result at continental-scale greatly.

We mapped and identified RTS across North Siberia. The spatial resolution of LT-LS2 (30m) allowed to detected RTS disturbances as small as four pixels and up to 15ha, which comprises the commonly reported RTS sizes (Lacelle et al. 2015; Segal et al. 2016). The RTS distribution and abundance closely correlates to ice-rich permafrost regions, either with thick syngenetic permafrost in Yedoma deposits (Strauss, Laboor, Fedorov, et al. 2016; Strauss et al. 2013) or in formerly glaciated areas with remaining buried glacial ice in moraines from the Last Glacial Maximum (LGM) or pre-LGM moraine complexes (Barr and Clark 2012; Kokelj et al. 2017). At focus sites most identified RTS were located along lakes, leading to the rapid erosion of lake shores, which alters the lake structure and increases the risk of lake drainage (Nitze et al. 2020) and also changes lake water chemistry with the increased intake of sediment and organic matter, which is indicated by high turbidity of the lakes (Lara, Chipman, and Hu 2019). The RTS density shows a clear relation to ice-rich permafrost regions and underlines their high vulnerability to permafrost thaw and disturbances. As RTS are defined by slope

erosion after ice-rich permafrost thaw, this is not a new insight. However, this is the first continental-scale assessment of RTS for North Siberia. The previous assessments with bigger spatial extents so far only covered regional extents in Russia (Western and Eastern Siberia), Alaska (Nitze et al. 2018), and Canada, including the High Arctic (Lewkowicz and Way 2019; Ward Jones, Pollard, and Jones 2019), Northwest Canada (Kokelj et al. 2017), Eastern Canada (Nitze et al. 2018). The majority of RTS studies are local, small-scale studies in Alaska (Balser, Jones, and Gens 2014), Canada (Brooker et al. 2014; Segal et al. 2016; Lantuit and Pollard 2005) and the Tibet-Plateau (Luo et al. 2019; Mu et al. 2020). However, the close correlation between ice-rich permafrost and RTS disturbances has never been depicted for such a large area (8.1 10^6 km^2) or for North Siberia in general. While a couple of RTS clusters in Siberia are known to scientist, such as Lower Lena, Batagay, Taymyr Peninsula and Bykovsky, only few studies are published (Günther et al. 2015; Séjourné et al. 2015; Nitze et al. 2018), leaving North Siberia predominantly unstudied. The RTS mapping and density assessment points out RTS hotspots, namely central Yakutia, West of the Verkhoyanks mountain range, and West Taymyr, which help to localise areas with increased permafrost thaw vulnerability and target further RTS assessments with very high-resolution imagery.

The RTS-affected area in North Siberia increased steadily from 2001-2019. Overall, the detected RTS area increased by 331 % from 2000 to the end of the time series, which is a substantial increase in this short time period. The majority of identified RTS were active from the beginning of the observation period, 2000 and 2001, and in contrast to that only a small proportion of new RTS were detected during the observation period. Since the number of identified RTS does not increase significantly, we can imply that the increase in RTS-affected area is caused by enlarging RTS and not newly initiated RTS. However, this observation is restricted by the spatial resolution and the minimum mapping unit applied, which prevents the detection of small-scale disturbances, such as RTS initiation. We therefore most like underestimate the number of RTS and the affected area in North Siberia alike. The focus sites depicted strong annual variability of RTS-affected area. Within the 19-year period distinct periods of increased and decreased thaw slump activity were determined. This annual variability and the peak slump years for each focus site varied, hence, indicating not only temporal but also spatial variability of RTS thaw dynamics in North Siberia. This emphasises the strong connection between RTS and thaw slumping drivers, which may vary from external climatic drivers and anthropogenic pressures to ground ice contents and local topography (Lewkowicz 2007; Ward Jones, Pollard, and Jones 2019; Kokelj et al. 2017). In the scope of this dissertation, I did not investigate thaw drivers thoroughly yet, however, the annual thaw slump dynamics derived here present the foundation of such a study. With the help of climate reanalysis data or, if available, ground measurements we would be able to identify local and regional drivers across North Siberia.

Combining the results from the focus sites and North Siberia, we can conclude that the steady increase in RTS-affected area in North Siberia is driven from spatio-temporal variability of RTS thaw dynamics at local to regional scale. This emphasises the increased impact of abrupt permafrost disturbances at the continental-scale and further highlights the importance of local to regional assessments for infrastructure planning or other site-specific analyses. The close correlation between high RTS density and ice-rich permafrost does not only signify the intensified vulnerability of permafrost to thaw, but also the increased impact on the carbon cycle, as most ice-rich regions are also often very organic-rich, which results in heightened carbon release (Turetsky et al. 2020). This continental-scale assessment comprises varying climatic, geologic, gemorphologic, and vegetational conditions that are characteristic for the heterogeneous permafrost regions, which makes the results representative across the pan-arctic. As increasing permafrost thaw due to climate change and strong Arctic warming is projected by models, we presume that the observed trend will continue.

5.5 Limitations and technical considerations

Despite the advantages of remote sensing-based assessments and the workflow described in this dissertation, certain limitations and technical considerations remain. The general restrictions of optical remote sensing in the northern high latitudes remain and even the combined use of two sensors might result in data-gaps in years with very frequent cloud cover and bad weather conditions, when even the combined Landsat and Sentinel-2 image database is not sufficient. Likewise, coastal, far northern high latitudes remain particularly challenging and large-scale mosaics may contain data-gaps.

The methods described in this dissertation do not fully address lack of data in the years prior to the launch of Sentinel-2 or even before 1999. Although the Landsat program already operates since 1973 and we have consistent and continuous images since mid-1980s for North America, the recorded acquisitions for Siberia were too sporadic for consistent spatial and temporal coverage before 1999. Therefore, the advances described and achieved in this study are mainly relevant for the period since Sentinel-2 is operational (5.5 years) and for future assessments. However, a correlation analysis between RTS annual results and clear-pixel availability testified reliable disturbance detection from the time series with only Landsat images as well. Hence, 1999 is a reasonable starting point of the time series

Currently, the workflow is based on top-of-atmosphere data as Sentinel-2 surface reflectance data is not yet available for the full image repository. While top-of-athmosphere data depicts abrupt spectral change well, more subtle, gradual change and trend analysis, e.g. detecting changes in phenology, is more sensitive to spectral change and rather requires atmospherically corrected surface reflectance data. Therefore, it will be necessary to change the input database to the surface reflectance products of Landsat and Sentinel-2, once the whole Sentinel-2 archive is available. Depending on the landscape or ecosystem change under assessment, one has to decide with image product is suitable.

Overall, we require more calibration and validation data to improve the mapping results of RTS at continental-scale. Obtaining more very high-resolution images and identifying RTS across more sights in North Siberia would improve the RTS classification accuracy and hence, the succeeding analysis and result interpretation. Furthermore, the lack of very high-resolution images prior 2013 is a disadvantage, as the LT-LS2 parametrisation for this time period was solely based on Landsat images themselves and not independent data.

5.6 Key findings

The research presented in this dissertation shows a framework for continental-scale assessments of abrupt permafrost disturbances at high temporal resolution. This work emphasises the advantages of combining Landsat and Sentinel-2 images and shows the improvements of a combined time series analyses in northern high latitudes, which enables the assessment of high temporal disturbances and changes at continental-scale. The thesis focuses on RTS but the framework similarly allows to assess wildfire disturbances, steep permafrost bluff erosion, thermokarst lake processes, anthropogenic infrastructure development and similar abrupt permafrost disturbances, which cause a change in spectral signature. The following are key findings of this dissertation:

- Landsat and Sentinel-2 are spectrally comparable in Arctic-Boreal regions
- Spectral bandpass adjustment coefficients for Arctic-Boreal regions, which lead to a close spectral agreement of Landsat 8 and Sentinel-2 and enable combined assessments of landscape and ecosystem changes

- Landsat+Sentinel-2 mosaics, which provide high spatial and temporal coverage input for time series algorithms, enabling high temporal and high resolution assessments in northern high latitudes
- The adaptation and parametrisation of LandTrendr to capture abrupt permafrost disturbances that allows for the first automatically derived assessment of RTS distribution and temporal dynamics at continental scale
- RTS-affected area increased steadily across North Siberia from 1999 to 2020
- Annual RTS thaw dynamics show local to regional spatio-temporal variability

5.7 Outlook

High temporal remote sensing-based disturbance detection and analysis at continental to global-scale will be increasingly important, to increase our understanding on their spatio-temporal variability and their overall disturbance dynamics. Furthermore, they are required for parametrisation of Earth System Models for an improved representation of permafrost thaw. Conducting large-scale assessments of other abrupt permafrost disturbances, such as wildfires, thermokarst lake change and drainage, and thermo-erosional gullies and vallies, will also be important in the future to include the full range of permafrost disturbances in Earth System Models. This is supported by the ever-increasing and improved data availability and enhanced data storage, processing and computing capabilities of Earth observation data. New Earth observation products, sensor systems and mission designs further increase data availability and enable to enhance the research scope. The following highlights opportunities for future research to increase our understanding of abrupt permafrost disturbances:

1. Very high-resolution multi-spectral data: a higher spatial resolution enhances the correct detection of local disturbances such as RTS or thermo-erosional features. An increased spatial resolution strengthens the reliable identification of permafrost disturbances in the landscape, while also enabling the detection of thaw processes at an earlier stage, such as its initiation. This is restricted in high to medium resolution images due to mixed pixels. We would be able to obtain a disturbance estimation which reduces the underestimation of small-scale disturbances. Moreover, a stronger spectral and spatial connection and correlation between very-high and high resolution images (for permafrost disturbances) should be established. Linking spectral signatures of high resolution images to very-high resolution and establishing disturbance relationships would enhance our overall permafrost disturbance assessment with high resolution data. We could achieve an improved applicability of Landsat images to disturbance detection, which would especially enhance change detection at the beginning of the 21st century, when little very high-resolution data is available.

2. Intra-annual dynamics: abrupt permafrost disturbances are closely driven by external factors, which intensify with climate change. Intra-annual time series analysis would allow to detect abrupt disturbances closer to the day of the disturbance event. This will improve the identification of prominent thaw drivers and increase our understanding of the high temporal thaw dynamics. PlanetScopes satellite constellation covers the whole Earth daily, which creates a dense time series at very high-resolution. Being able to differentiate between spring, early summer, late summer and autumn will improve our understanding of permafrost thaw dynamics greatly and help to identify distinct thaw drivers. Narrowing primary thaw disturbances to a season will also increase our understanding on their effect on soil organic carbon release as microbial processes vary depending on climate and surrounding conditions.

3. Near real-time monitoring: Permafrost thaw and disturbances create a particular risk to infrastructure and human beings in the Arctic. Detecting permafrost disturbances early would enable to close affected roads, airports or evacuate buildings and villages in time. This requires automated mapping and detection systems with a pipeline adding the most recent satellite images and automatically deriving disturbance products. PlanetScope data (VHR) or Sentinel-2 data could be very useful for such an application and enable early detection and warning for areas experiencing abrupter permafrost thaw.

References

A, Moez (July 2020). *PyCaret: An open source, low-code machine learning library in Python.* PyCaret version 2.3.

AMAP (2017). "Snow, Water, Ice and Permafrost in the Arctic (SWIPA); Summary for Policy-makers". In:

Antonova, S, H Sudhaus, T Strozzi, S Zwieback, A Kääb, B Heim, M Langer, N Bornemann, and J Boike (2018). "Thaw subsidence of a yedoma landscape in northern Siberia, measured in situ and estimated from TerraSAR-X interferometry". In: *Remote Sensing* 10.4, p. 494.

Ardelean, F, Au Onaca, M-A Chețan, A Dornik, G Georgievski, S Hagemann, F Timofte, and O Berzescu (2020). "Assessment of Spatio-Temporal Landscape Changes from VHR Images in Three Different Permafrost Areas in the Western Russian Arctic". In: *Remote Sensing* 12.23, p. 3999.

Are, FE (1988). "Thermal abrasion of sea coast". In: *Polar Geogr. and Geol* 12, pp. 1–157.

Ashastina, K, L Schirrmeister, M Fuchs, and F Kienast (2017). "Palaeoclimate characteristics in interior Siberia of MIS 6–2: first insights from the Batagay permafrost mega-thaw slump in the Yana Highlands". In: *Climate of the Past* 13, pp. 795–818.

Balser, AW, JB Jones, and R Gens (2014). "Timing of retrogressive thaw slump initiation in the Noatak Basin, northwest Alaska, USA". In: *Journal of Geophysical Research: Earth Surface* 119.5, pp. 1106–1120.

Bannari, A, D Morin, F Bonn, and AR Huete (1995). "A review of vegetation indices". In: *Remote sensing reviews* 13.1-2, pp. 95–120.

Barnes, WL and VV Salomonson (1992). "MODIS: A global imaging spectroradiometer for the Earth Observing System". In: *Optical Technologies for Aerospace Sensing: A Critical Review*. Vol. 10269. International Society for Optics and Photonics, 102690G.

Barr, ID and CD Clark (2012). "An updated moraine map of Far NE Russia". In: *Journal of Maps* 8.4, pp. 431–436.

Bartlett, JS, AM Ciotti, RF Davis, and JJ Cullen (1998). "The spectral effects of clouds on solar irradiance". In: *Journal of Geophysical Research: Oceans* 103.C13, pp. 31017–31031.

Bartsch, A, A Höfler, C Kroisleitner, and A Trofaier (2016). "Land cover mapping in northern high latitude permafrost regions with satellite data: Achievements and remaining challenges". In: *Remote Sensing* 8.12, p. 979.

Beamish, A, MK Raynolds, H Epstein, GV Frost, MJ Macander, H Bergstedt, A Bartsch, S Kruse, V Miles, CM Tanis, et al. (2020). "Recent trends and remaining challenges for optical remote sensing of Arctic tundra vegetation: A review and outlook". In: *Remote Sensing of Environment* 246, p. 111872.

Beck, I, RP Ludwig, M Bernier, T Strozzi, and J Boike (2015). "Vertical movements of frost mounds in subarctic permafrost regions analyzed using geodetic survey and satellite interferometry." In: *Earth Surface Dynamics* 3.3, pp. 409–421.

Biskaborn, BK, SL Smith, J Noetzli, H Matthes, G Vieira, DA Streletskiy, P Schoeneich, VE Romanovsky, AG Lewkowicz, A Abramov, et al. (2019). "Permafrost is warming at a global scale". In: *Nature communications* 10.1, p. 264.

Boike, J, T Grau, B Heim, F Günther, M Langer, S Muster, I Gouttevin, and S Lange (2016). "Satellite-derived changes in the permafrost landscape of central Yakutia, 2000–2011: Wetting, drying, and fires". In: *Global and planetary change* 139, pp. 116–127.

Boike, J, B Kattenstroth, E Abramova, N Bornemann, A Chetverova, I Fedorova, K Fröb, M Grigoriev, M Grüber, L Kutzbach, et al. (2013). "Baseline characteristics of climate, permafrost and land cover from a new permafrost observatory in the Lena River Delta, Siberia (1998-2011)". In: *Biogeosciences (BG)* 10.3, pp. 2105–2128.

Box, JE, WT Colgan, TR Christensen, NM Schmidt, M Lund, F-JW Parmentier, R Brown, US Bhatt, ES Euskirchen, VE Romanovsky, et al. (2019). "Key indicators of Arctic climate change: 1971–2017". In: *Environmental Research Letters* 14.4, p. 045010.

Brooker, A, RH Fraser, I Olthof, SV Kokelj, and D Lacelle (2014). "Mapping the activity and evolution of retrogressive thaw slumps by tasselled cap trend analysis of a Landsat satellite image stack". In: *Permafrost and Periglacial Processes* 25.4, pp. 243–256.

Brown, J, OJ Ferrians Jr, JA Heginbottom, and ES Melnikov (1997). *Circum-Arctic map of permafrost and ground-ice conditions*. US Geological Survey Reston, VA.

Burn, CR and AG Lewkowicz (1990). "Canadian landform examples-17 retrogressive thaw slumps". In: *Canadian Geographer/Le Géographe canadien* 34.3, pp. 273–276.

Carrasco, L, AW ONeil, RD Morton, and CS Rowland (2019). "Evaluating combinations of temporally aggregated Sentinel-1, Sentinel-2 and Landsat 8 for land cover mapping with Google Earth Engine". In: *Remote Sensing* 11.3, p. 288.

Cassidy, AE, A Christen, and GHR Henry (2017). "Impacts of active retrogressive thaw slumps on vegetation, soil, and net ecosystem exchange of carbon dioxide in the Canadian High Arctic". In: *Arctic Science* 3.2, pp. 179–202.

Chadburn, SE, EJ Burke, PM Cox, P Friedlingstein, G Hugelius, and S Westermann (2017). "An observation-based constraint on permafrost loss as a function of global warming". In: *Nature Climate Change* 7.5, p. 340.

Chander, G, BL Markham, and DL Helder (2009). "Summary of current radiometric calibration coefficients for Landsat MSS, TM, ETM+, and EO-1 ALI sensors". In: *Remote sensing of environment* 113.5, pp. 893–903.

Chastain, R, I Housman, J Goldstein, M Finco, and K Tenneson (2019). "Empirical cross sensor comparison of Sentinel-2A and 2B MSI, Landsat-8 OLI, and Landsat-7 ETM+ top of atmosphere spectral characteristics over the conterminous United States". In: *Remote sensing of environment* 221, pp. 274–285.

Chawla, NV, KW Bowyer, LO Hall, and WP Kegelmeyer (2002). "SMOTE: synthetic minority over-sampling technique". In: *Journal of artificial intelligence research* 16, pp. 321–357.

Claverie, M, J Ju, JG Masek, JL Dungan, EF Vermote, J-C Roger, SV Skakun, and C Justice (2018). "The Harmonized Landsat and Sentinel-2 surface reflectance data set". In: *Remote Sensing of Environment* 219, pp. 145–161.

Cohen, WB, Z Yang, and R Kennedy (2010). "Detecting trends in forest disturbance and recovery using yearly Landsat time series: 2. TimeSync—Tools for calibration and validation". In: *Remote Sensing of Environment* 114.12, pp. 2911–2924.

Collins, SL, SM Swinton, CW Anderson, TL Gragson, NB Grimm, M Grove, AK Knapp, G Kofinas, J Magnuson, B McDowell, et al. (2007). "Integrated science for society and the environment: a strategic research initiative". In: *Albuquerque, Long-Term Ecological Research Network, Publication* 23.

Coluzzi, R, V Imbrenda, M Lanfredi, and T Simoniello (2018). "A first assessment of the Sentinel-2 Level 1-C cloud mask product to support informed surface analyses". In: *Remote sensing of environment* 217, pp. 426–443.

Copernicus Climate Change Service (2017). "ERA5: Fifth generation of ECMWF atmospheric reanalyses of the global climate. Copernicus Climate Change Service Climate Data Store (CDS)". In: *Accessed March 2021.*

Cowan, G (1998). *Statistical data analysis*. Oxford university press.

Dara, A, M Baumann, T Kuemmerle, D Pflugmacher, A Rabe, P Griffiths, N Hölzel, J Kamp, M Freitag, and P Hostert (2018). "Mapping the timing of cropland abandonment and

recultivation in northern Kazakhstan using annual Landsat time series". In: *Remote Sensing of Environment* 213, pp. 49–60.

Donchyts, G (July 2017). *Implementation of Basic cloud shadow shift*. Google Earth Engine code. URL: %5Curl % 7Bhttps : / / code . earthengine . google . com / 120d7d9ccc3c7c6c90b335d48be53636%7D.

Drusch, M, U Del Bello, S Carlier, O Colin, V Fernandez, F Gascon, B Hoersch, C Isola, P Laberinti, P Martimort, et al. (2012). "Sentinel-2: ESA's optical high-resolution mission for GMES operational services". In: *Remote sensing of Environment* 120, pp. 25–36.

Earth, Natural (2008). *Rivers + lake centrelines*. https://www.naturalearthdata.com/downloads/10m-physical-vectors/10m-rivers-lake-centerlines/. [Online; accessed 28-01-2021].

Egorov, AV, DP Roy, HK Zhang, Z Li, and H Yan Land Huang (2019). "Landsat 4, 5 and 7 (1982 to 2017) Analysis Ready Data (ARD) observation coverage over the conterminous United States and implications for terrestrial monitoring". In: *Remote Sensing* 11.4, p. 447.

Ehlers, J and PL Gibbard (2003). "Extent and chronology of glaciations". In: *Quaternary Science Reviews* 22.15-17, pp. 1561–1568.

ESA (2015). "Sentinel-2 User Handbook". In: *ESA* 1.

— (2020). *Cloud Masks*. https://sentinel.esa.int/web/sentinel/technical-guides/sentinel-2-msi/level-1c/cloud-masks. [Online; accessed 24-March-2020].

ESRI (2017). *ESRI Satellite [basemap]*. 29-June-2017. Accessed 15-February-2021.

Etzelmüller, B, M Guglielmin, C Hauck, C Hilbich, M Hoelzle, K Isaksen, J Noetzli, M Oliva, and M Ramos (2020). "Twenty years of European mountain permafrost dynamics—the PACE legacy". In: *Environmental Research Letters* 15.10, p. 104070.

Farquharson, LM, VE Romanovsky, WL Cable, DA Walker, SV Kokelj, and D Nicolsky (2019). "Climate change drives widespread and rapid thermokarst development in very cold permafrost in the Canadian High Arctic". In: *Geophysical Research Letters* 46.12, pp. 6681–6689.

Fedorov, AN, PP Gavriliev, PY Konstantinov, T Hiyama, Y Iijima, and G Iwahana (2014). "Estimating the water balance of a thermokarst lake in the middle of the Lena River basin, eastern Siberia". In: *Ecohydrology* 7.2, pp. 188–196.

Fedorov, AN, G Iwahana, PY Konstantinov, T Machimura, RN Argunov, PV Efremov, LMC Lopez, and F Takakai (2017). "Variability of permafrost and landscape conditions following clear cutting of larch forest in central Yakutia". In: *Permafrost and Periglacial Processes* 28.1, pp. 331–338.

Flood, N (2013). “Seasonal composite Landsat TM/ETM+ images using the medoid (a multi-dimensional median)”. In: *Remote Sensing* 5.12, pp. 6481–6500.

— (2014). “Continuity of reflectance data between Landsat-7 ETM+ and Landsat-8 OLI, for both top-of-atmosphere and surface reflectance: a study in the Australian landscape”. In: *Remote Sensing* 6.9, pp. 7952–7970.

— (2017). “Comparing Sentinel-2A and Landsat 7 and 8 using surface reflectance over Australia”. In: *Remote Sensing* 9.7, p. 659.

Foga, S, PL Scaramuzza, S Guo, Z Zhu, RD Dilley Jr, T Beckmann, GL Schmidt, JL Dwyer, MJ Hughes, and B Laue (2017). “Cloud detection algorithm comparison and validation for operational Landsat data products”. In: *Remote sensing of environment* 194, pp. 379–390.

Francis, JA, DM White, JJ Cassano, WJ Gutowski, LD Hinzman, MM Holland, MA Steele, and CJ Vörösmarty (2009). “An arctic hydrologic system in transition: Feedbacks and impacts on terrestrial, marine, and human life”. In: *Journal of Geophysical Research: Biogeosciences* 114.G4.

Frantz, D (2019). “FORCEâ€”Landsat+ Sentinel-2 analysis ready data and beyond”. In: *Remote Sensing* 11.9, p. 1124.

Frazier, RJ, NC Coops, MA Wulder, T Hermosilla, and JC White (2018). “Analyzing spatial and temporal variability in short-term rates of post-fire vegetation return from Landsat time series”. In: *Remote Sensing of Environment* 205, pp. 32–45.

French, HM and P Williams (2007). *The periglacial environment*. Vol. 458. Wiley Online Library.

Gomes, VCF, GR Queiroz, and KR Ferreira (2020). “An overview of platforms for big earth observation data management and analysis”. In: *Remote Sensing* 12.8, p. 1253.

Gómez, C, JC White, and MA Wulder (2016). “Optical remotely sensed time series data for land cover classification: A review”. In: *ISPRS Journal of Photogrammetry and Remote Sensing* 116, pp. 55–72.

Gómez-Chova, L, G Camps-Valls, J Calpe-Maravilla, L Guanter, and J Moreno (2007). “Cloud-screening algorithm for ENVISAT/MERIS multispectral images”. In: *IEEE Transactions on Geoscience and Remote Sensing* 45.12, pp. 4105–4118.

Google Developers (2020a). *Landsat Algorithms*. `https://developers.google.com/earth-engine/landsat#landsat-collection-structure`. [Online; accessed 15-July-2020].

— (2020b). *Sentinel-2 MSI: MultiSpectral Instrument, Level-2A*. `https://developers.google.com/earth-engine/datasets/catalog/COPERNICUS_S2_SR`. [Online; accessed 13-July-2020].

Google Developers (2021). *Google Earth Engine*. `https://developers.google.com/earth-engine`. [Online; accessed 19-Januay-2021].

Gorelick, N, M Hancher, M Dixon, S Ilyushchenko, D Thau, and R Moore (2017). "Google Earth Engine: Planetary-scale geospatial analysis for everyone". In: *Remote Sensing of Environment* 202, pp. 18–27.

Gorroño, J, AC Banks, NP Fox, and C Underwood (2017). "Radiometric inter-sensor cross-calibration uncertainty using a traceable high accuracy reference hyperspectral imager". In: *ISPRS Journal of Photogrammetry and Remote Sensing* 130, pp. 393–417.

Griffiths, P, C Nendel, and P Hostert (2019). "Intra-annual reflectance composites from Sentinel-2 and Landsat for national-scale crop and land cover mapping". In: *Remote sensing of environment* 220, pp. 135–151.

Grosse, G, S Goetz, AD McGuire, VE Romanovsky, and EAG Schuur (2016). "Changing permafrost in a warming world and feedbacks to the Earth system". In: *Environmental Research Letters* 11.4, p. 040201.

Grosse, G, J Harden, M Turetsky, AD McGuire, P Camill, C Tarnocai, S Frolking, EAG Schuur, T Jorgenson, S Marchenko, et al. (2011a). "Vulnerability of high-latitude soil organic carbon in North America to disturbance". In: *Journal of Geophysical Research: Biogeosciences* 116.G4.

Grosse, G, J Harden, M Turetsky, AD McGuire, P Camill, C Tarnocai, S Frolking, EAG Schuur, T Jorgenson, S Marchenko, V Romanovsky, KP Wickland, N French, M Waldrop, L Bourgeau-Chavez, and RG Striegl (2011b). "Vulnerability of high-latitude soil organic carbon in North America to disturbance". In: *Journal of Geophysical Research: Biogeosciences* 116.G4. DOI: `10.1029/2010JG001507`.

Grosse, G, V Romanovsky, T Jorgenson, K Walter Anthony, J Brown, and PP Overduin (2011c). "Vulnerability and feedbacks of permafrost to climate change". In: *Eos, Transactions American Geophysical Union* 92.9, pp. 73–74.

Grosse, G, L Schirrmeister, C Siegert, VV Kunitsky, EA Slagoda, AA Andreev, and AY Dereviagyn (2007). "Geological and geomorphological evolution of a sedimentary periglacial landscape in Northeast Siberia during the Late Quaternary". In: *Geomorphology* 86.1-2, pp. 25–51.

Grosse, Gu, BM Jones, and CD Arp (2013). "Thermokarst lakes, drainage, and drained basins". In:

Guglielmin, M and G Vieira (2014). *Permafrost and periglacial research in Antarctica: New results and perspectives*.

Günther, F, G Grosse, BM Jones, L Schirrmeister, VE Romanovsky, and V Kunitsky (2016). "Unprecedented permafrost thaw dynamics on a decadal time scale: Batagay mega thaw slump development, Yana Uplands, Yakutia, Russia". In: *AGU Fall Meeting Abstracts*.

Günther, F, G Grosse, S Wetterich, BM Jones, VV Kunitsky, F Kienast, and L Schirrmeister (2015). "The Batagay mega thaw slump, Yana Uplands, Yakutia, Russia: permafrost thaw dynamics on decadal time scale". In: TERRA NOSTRA-Schriften der GeoUnion Alfred-Wegener-Stiftung.

Günther, F, PP Overduin, AV Sandakov, G Grosse, and MN Grigoriev (2013). "Short-and long-term thermo-erosion of ice-rich permafrost coasts in the Laptev Sea region". In: *Biogeosciences* 10.6, pp. 4297–4318.

Hansen, MC, PV Potapov, R Moore, M Hancher, SA Turubanova, A Tyukavina, SV Thau Dand Stehman, SJ Goetz, TR Loveland, et al. (2013). "High-resolution global maps of 21st-century forest cover change". In: *science* 342.6160, pp. 850–853.

Hicks Pries, CE, RSP Van Logtestijn, EAG Schuur, SM Natali, JHC Cornelissen, R Aerts, and E Dorrepaal (2015). "Decadal warming causes a consistent and persistent shift from heterotrophic to autotrophic respiration in contrasting permafrost ecosystems". In: *Global change biology* 21.12, pp. 4508–4519.

Hinkel, KM, BM Jones, WR Eisner, CJ Cuomo, RA Beck, and R Frohn (2007). "Methods to assess natural and anthropogenic thaw lake drainage on the western Arctic coastal plain of northern Alaska". In: *Journal of Geophysical Research: Earth Surface* 112.F2.

Hjort, J, O Karjalainen, J Aalto, S Westermann, VE Romanovsky, FE Nelson, B Etzelmüller, and M Luoto (2018). "Degrading permafrost puts Arctic infrastructure at risk by mid-century". In: *Nature communications* 9.1, p. 5147.

Hoersch, B (2015). "Sentinel-2 User Handbook". In: *ESA Standard Document*.

Hollstein, A, K Segl, L Guanter, M Brell, and M Enesco (2016). "Ready-to-use methods for the detection of clouds, cirrus, snow, shadow, water and clear sky pixels in Sentinel-2 MSI images". In: *Remote Sensing* 8.8, p. 666.

Hope, AS and DA Stow (1996). "Shortwave reflectance properties of arctic tundra landscapes". In: *Landscape Function and Disturbance in Arctic Tundra*. Springer, pp. 155–164.

Huang, C, SN Goward, JG Masek, Na Thomas, Z Zhu, and JE Vogelmann (2010). "An automated approach for reconstructing recent forest disturbance history using dense Landsat time series stacks". In: *Remote Sensing of Environment* 114.1, pp. 183–198.

Huang, C, B Wylie, L Yang, C Homer, and G Zylstra (2002). "Derivation of a tasselled cap transformation based on Landsat 7 at-satellite reflectance". In: *International journal of remote sensing* 23.8, pp. 1741–1748.

Huang, L, J Luo, Z Lin, F Niu, and L Liu (2020). "Using deep learning to map retrogressive thaw slumps in the Beiluhe region (Tibetan Plateau) from CubeSat images". In: *Remote Sensing of Environment* 237, p. 111534.

Hubberten, HW, A Andreev, VI Astakhov, I Demidov, JA Dowdeswell, M Henriksen, C Hjort, M Houmark-Nielsen, M Jakobsson, S Kuzmina, et al. (2004). "The periglacial climate and environment in northern Eurasia during the Last Glaciation". In: *Quaternary Science Reviews* 23.11-13, pp. 1333–1357.

Hugelius, G, J Strauss, S Zubrzycki, JW Harden, EAG Schuur, C-L Ping, L Schirrmeister, G Grosse, GJ Michaelson, CD Koven, et al. (2014). "Estimated stocks of circumpolar permafrost carbon with quantified uncertainty ranges and identified data gaps". In: *Biogeosciences (Online)* 11.23.

IPCC (2014). *Climate change 2014: synthesis report. Contribution of Working Groups I, II and III to the fifth assessment report of the Intergovernmental Panel on Climate Change*. Ed. by IPCC, RK Pachauri, MR Allen, VR Barros, J Broome, W Cramer, R Christ, JA Church, L Clarke, Q Dahe, P Dasgupta, et al. Ipcc.

Irons, JR, JL Dwyer, and JA Barsi (2012). "The next Landsat satellite: The Landsat data continuity mission". In: *Remote Sensing of Environment* 122, pp. 11–21.

Irrgang, AM, H Lantuit, GK Manson, F Günther, G Grosse, and PP Overduin (2018). "Variability in rates of coastal change along the Yukon coast, 1951 to 2015". In: *Journal of Geophysical Research: Earth Surface* 123.4, pp. 779–800.

Ivanova, RN (2003). "Seasonal thawing of soils in the Yana River valley, northern Yakutia". In: *Permafrost, Proceedings of the Eighth International Conference on Permafrost*, pp. 21–25.

J, Braaten (2020). *LandTrendr Time Series Animator*. Snazzy-EE-TS-GIF.

Jan, A and SL Painter (2020). "Permafrost thermal conditions are sensitive to shifts in snow timing". In: *Environmental Research Letters* 15.8, p. 084026.

Jones, BM, CD Arp, G Grosse, I Nitze, MJ Lara, MS Whitman, LM Farquharson, M Kanevskiy, AD Parsekian, AL Breen, et al. (2020). "Identifying historical and future potential lake drainage events on the western Arctic coastal plain of Alaska". In: *Permafrost and Periglacial Processes* 31.1, pp. 110–127.

Jones, BM, LM Farquharson, CA Baughman, RM Buzard, CD Arp, G Grosse, DL Bull, F Günther, I Nitze, F Urban, et al. (2018). "A decade of remotely sensed observations highlight complex processes linked to coastal permafrost bluff erosion in the Arctic". In: *Environmental Research Letters* 13.11, p. 115001.

Jorgenson, MT and G Grosse (2016). "Remote sensing of landscape change in permafrost regions". In: *Permafrost and Periglacial Processes* 27.4, pp. 324–338.

Jorgenson, MT, G Grosse, B Jones, C Arp, NF Glasser, KA Cherkauer, LC Bowling, B Naz, and TRH Davies (2013). "Treatise on Geomorphology". In: Elsevier. Chap. 8.20 Thermokarst Terrains.

Jorgenson, MT, V Romanovsky, J Harden, Y Shur, J O'Donnell, EAG Schuur, M Kanevskiy, and S Marchenko (2010). "Resilience and vulnerability of permafrost to climate change". In: *Canadian Journal of Forest Research* 40.7, pp. 1219–1236.

Ju, J and DP Roy (2008). "The availability of cloud-free Landsat ETM+ data over the conterminous United States and globally". In: *Remote Sensing of Environment* 112.3, pp. 1196–1211.

Kääb, A (2008). "Remote sensing of permafrost-related problems and hazards". In: *Permafrost and periglacial processes* 19.2, pp. 107–136.

Kääb, A, M Chiarle, B Raup, and C Schneider (2007). "Climate change impacts on mountain glaciers and permafrost". In: *GPC* 56.1-2, pp. vii–ix.

Kanevskiy, M, Y Shur, D Fortier, MT Jorgenson, and E Stephani (2011). "Cryostratigraphy of late Pleistocene syngenetic permafrost (yedoma) in northern Alaska, Itkillik River exposure". In: *Quaternary research* 75.3, pp. 584–596.

Kaplan, JO and M New (2006). "Arctic climate change with a 2 C global warming: Timing, climate patterns and vegetation change". In: *Climatic change* 79.3-4, pp. 213–241.

Kasischke, ES, BD Amiro, NN Barger, NHF French, SJ Goetz, G Grosse, ME Harmon, JA Hicke, S Liu, and JG Masek (2013). "Impacts of disturbance on the terrestrial carbon budget of North America". In: *Journal of Geophysical Research: Biogeosciences* 118.1, pp. 303–316.

Ke, G, Q Meng, T Finley, T Wang, W Chen, W Ma, Q Ye, and T-Y Liu (2017). "LightGBM: A Highly Efficient Gradient Boosting Decision Tree". In: *Advances in Neural Information Processing Systems*. Ed. by I. Guyon, U. V. Luxburg, S. Bengio, H. Wallach, R. Fergus, S. Vishwanathan, and R. Garnett. Vol. 30. Curran Associates, Inc.

Kennedy, RE, Z Yang, and WB Cohen (2010). "Detecting trends in forest disturbance and recovery using yearly Landsat time series: 1. LandTrendr—Temporal segmentation algorithms". In: *Remote Sensing of Environment* 114.12, pp. 2897–2910.

Kennedy, RE, Z Yang, N Gorelick, J Braaten, L Cavalcante, WB Cohen, and S Healey (2018). "Implementation of the LandTrendr algorithm on google earth engine". In: *Remote Sensing* 10.5, p. 691.

Key, CH and NC Benson (2005). "Landscape assessment: remote sensing of severity, the normalized burn ratio and ground measure of severity, the composite burn index". In:

FIREMON: Fire effects monitoring and inventory system Ogden, Utah: USDA Forest Service, Rocky Mountain Res. Station.

Kokelj, SV, RE Jenkins, D Milburn, CR Burn, and N Snow (2005). "The influence of thermokarst disturbance on the water quality of small upland lakes, Mackenzie Delta region, Northwest Territories, Canada". In: *Permafrost and Periglacial Processes* 16.4, pp. 343–353.

Kokelj, SV and MT Jorgenson (2013). "Advances in thermokarst research". In: *Permafrost and Periglacial Processes* 24.2, pp. 108–119.

Kokelj, SV, D Lacelle, TC Lantz, J Tunnicliffe, L Malone, ID Clark, and KS Chin (2013). "Thawing of massive ground ice in mega slumps drives increases in stream sediment and solute flux across a range of watershed scales". In: *Journal of Geophysical Research: Earth Surface* 118.2, pp. 681–692.

Kokelj, SV, TC Lantz, J Kanigan, SL Smith, and R Coutts (2009). "Origin and polycyclic behaviour of tundra thaw slumps, Mackenzie Delta region, Northwest Territories, Canada". In: *Permafrost and Periglacial Processes* 20.2, pp. 173–184.

Kokelj, SV, TC Lantz, J Tunnicliffe, R Segal, and D Lacelle (2017). "Climate-driven thaw of permafrost preserved glacial landscapes, northwestern Canada". In: *Geology* 45.4, pp. 371–374.

Kokelj, SV, J Tunnicliffe, D Lacelle, TC Lantz, KS Chin, and R Fraser (2015a). "Increased precipitation drives mega slump development and destabilization of ice-rich permafrost terrain, northwestern Canada". In: *Global and Planetary Change* 129, pp. 56–68.

Kokelj, SV, J Tunnicliffe, D Lacelle, TC Lantz, and RH Fraser (2015b). "Retrogressive thaw slumps: From slope process to the landscape sensitivity of northwestern Canada". In: *Proceedings of the 68th Canadian geotechnical conference, GeoQuébec.*

Korhonen, L, P Packalen, M Rautiainen, et al. (2017). "Comparison of Sentinel-2 and Landsat 8 in the estimation of boreal forest canopy cover and leaf area index". In: *Remote sensing of environment* 195, pp. 259–274.

Koven, CD, B Ringeval, P Friedlingstein, P Ciais, P Cadule, D Khvorostyanov, G Krinner, and C Tarnocai (2011). "Permafrost carbon-climate feedbacks accelerate global warming". In: *Proceedings of the National Academy of Sciences* 108.36, pp. 14769–14774.

Krischke, M, W Niemeyer, and S Scherer (2000). "RapidEye satellite based geo-information system". In: *Acta Astronautica* 46.2-6, pp. 307–312.

Kuenzer, C, S Dech, and W Wagner (2015). "Remote sensing time series revealing land surface dynamics: Status quo and the pathway ahead". In: *Remote Sensing Time Series*. Springer, pp. 1–24.

Kunitsky, VV, I Syromyatnikov, L Schirrmeister, YB Skachov, G Grosse, S Wetterich, and MN Grigoriev (2013). "Ice-rich permafrost and thermal denudation in the Batagay area (Yana Upland, East Siberia)". In: *Earth Cryosphere (Kriosfera Zemli)* 17.1, pp. 56–58.

Lacelle, D, A Brooker, RH Fraser, and SV Kokelj (2015). "Distribution and growth of thaw slumps in the Richardson Mountains–Peel Plateau region, northwestern Canada". In: *Geomorphology* 235, pp. 40–51.

Lantuit, H and WH Pollard (2005). "Temporal stereophotogrammetric analysis of retrogressive thaw slumps on Herschel Island, Yukon Territory". In:

— (2008). "Fifty years of coastal erosion and retrogressive thaw slump activity on Herschel Island, southern Beaufort Sea, Yukon Territory, Canada". In: *Geomorphology* 95.1-2, pp. 84–102.

Lantz, TC and SV Kokelj (2008). "Increasing rates of retrogressive thaw slump activity in the Mackenzie Delta region, NWT, Canada". In: *Geophysical Research Letters* 35.6.

Lara, MJ, ML Chipman, and FS Hu (2019). "Automated detection of thermoerosion in permafrost ecosystems using temporally dense Landsat image stacks". In: *Remote Sensing of Environment* 221, pp. 462–473.

Lara, MJ, I Nitze, G Grosse, P Martin, and AD McGuire (2018). "Reduced arctic tundra productivity linked with landform and climate change interactions". In: *Scientific Reports* 8.1, pp. 1–10.

Lenton, TM (2012). "Arctic climate tipping points". In: *Ambio* 41.1, pp. 10–22.

Lenton, TM, J Rockström, O Gaffney, S Rahmstorf, K Richardson, W Steffen, and HJ Schellnhuber (2019). *Climate tipping points—too risky to bet against.*

Lewkowicz, AG (2007). "Dynamics of active-layer detachment failures, Fosheim peninsula, Ellesmere Island, Nunavut, Canada". In: *Permafrost and Periglacial Processes* 18.1, pp. 89–103.

Lewkowicz, AG and RG Way (2019). "Extremes of summer climate trigger thousands of thermokarst landslides in a High Arctic environment". In: *Nature communications* 10.1, pp. 1–11.

Li, J and D Roy (2017). "A global analysis of Sentinel-2A, Sentinel-2B and Landsat-8 data revisit intervals and implications for terrestrial monitoring". In: *Remote Sensing* 9.9, p. 902.

Li, S, S Ganguly, JL Dungan, W Wang, and RR Nemani (2017). "Sentinel-2 MSI radiometric characterization and cross-calibration with Landsat-8 OLI". In: *Advances in Remote Sensing* 6.02, p. 147.

Liljedahl, AK, J Boike, RP Daanen, AN Fedorov, GV Frost, G Grosse, LD Hinzman, Y Iijma, JC Jorgenson, N Matveyeva, et al. (2016). "Pan-Arctic ice-wedge degradation in warming permafrost and its influence on tundra hydrology". In: *Nature Geoscience* 9.4, pp. 312–318.

Louis, J, V Debaecker, B Pflug, M Main-Knorn, J Bieniarz, U Mueller-Wilm, E Cadau, and F Gascon (2016). "Sentinel-2 Sen2Cor: L2A processor for users". In: *Proceedings of the Living Planet Symposium, Prague, Czech Republic*, pp. 9–13.

Luo, J, F Niu, Z Lin, M Liu, and G Yin (2019). "Recent acceleration of thaw slumping in permafrost terrain of Qinghai-Tibet Plateau: An example from the Beiluhe Region". In: *Geomorphology* 341, pp. 79–85.

Lydolph, PE, D Temple, and D Temple (1985). *The climate of the earth*. Government Institutes.

Main-Knorn, M, B Pflug, J Louis, and V Debaecker (2015). "Calibration and validation plan for the L2A processor and products of the Sentinel-2 mission". In: *Proceedings of International Symposium on Remote Sensing of Environment (ISRSE) 2015*. Vol. 40. W3. Copernicus Publications, pp. 1249–1255.

Mandanici, E and G Bitelli (2016). "Preliminary comparison of sentinel-2 and landsat 8 imagery for a combined use". In: *Remote Sensing* 8.12, p. 1014.

Masek, JG, EF Vermote, NE Saleous, R Wolfe, FG Hall, KF Huemmrich, F Gao, J Kutler, and T-K Lim (2006). "A Landsat surface reflectance dataset for North America, 1990-2000". In: *IEEE Geoscience and Remote Sensing Letters* 3.1, pp. 68–72.

Meredith, M, M Sommerkorn, S Cassotta, C Derksen, A Ekaykin, A Hollowed, G Kofinas, A Mackintosh, J Melbourne-Thomas, MMC Muelbert, et al. (2019). "Polar Regions. Chapter 3, IPCC Special Report on the Ocean and Cryosphere in a Changing Climate". In:

Militino, AF, MD Ugarte, and U Pérez-Goya (2018). "An introduction to the spatio-temporal analysis of satellite remote sensing data for geostatisticians". In: *Handbook of Mathematical Geosciences*. Springer, Cham, pp. 239–253.

Mishra, N, MD Haque, L Leigh, D Aaron, D Helder, and B Markham (2014). "Radiometric cross calibration of Landsat 8 operational land imager (OLI) and Landsat 7 enhanced thematic mapper plus (ETM+)". In: *Remote sensing* 6.12, pp. 12619–12638.

Morgenstern, A, G Grosse, F Günther, I Fedorova, and L Schirrmeister (2011). "Spatial analyses of thermokarst lakes and basins in Yedoma landscapes of the Lena Delta". In: *The Cryosphere Discussions* 5, pp. 1495–1545.

Morgenstern, A, PP Overduin, F Günther, S Stettner, J Ramage, L Schirrmeister, MN Grigoriev, and G Grosse (2021). "Thermo-erosional valleys in Siberian ice-rich permafrost". In: *Permafrost and Periglacial Processes* 32.1, pp. 59–75. DOI: 10.1002/ppp.2087.

Mu, C, J Shang, T Zhang, C Fan, S Wang, X Peng, W Zhong, F Zhang, M Mu, and L Jia (2020). "Acceleration of thaw slump during 1997–2017 in the Qilian Mountains of the northern Qinghai-Tibetan plateau". In: *Landslides* 17.5, pp. 1051–1062.

Müller-Wilm, U, O Devignot, and L Pessiot (2016). "Sen2Cor Configuration and User Manual". In: *Telespazio VEGA Deutschland GmbH: Darmstadt, Germany.*

Nitzbon, J, S Westermann, M Langer, LCP Martin, J Strauss, S Laboor, and J Boike (2020). "Fast response of cold ice-rich permafrost in northeast Siberia to a warming climate". In: *Nature communications* 11.1, pp. 1–11.

Nitze, I, SW Cooley, CR Duguay, BM Jones, and G Grosse (2020). "The catastrophic thermokarst lake drainage events of 2018 in northwestern Alaska: Fast-forward into the future". In: *The Cryosphere* 14.12, pp. 4279–4297.

Nitze, I and G Grosse (2016). "Detection of landscape dynamics in the Arctic Lena Delta with temporally dense Landsat time-series stacks". In: *Remote Sensing of Environment* 181, pp. 27–41.

Nitze, I, G Grosse, BM Jones, CD Arp, M Ulrich, A Fedorov, and A Veremeeva (2017). "Landsat-based trend analysis of lake dynamics across northern permafrost regions". In: *Remote Sensing* 9.7, p. 640.

Nitze, I, G Grosse, BM Jones, VE Romanovsky, and J Boike (2018). "Remote sensing quantifies widespread abundance of permafrost region disturbances across the Arctic and Subarctic". In: *Nature Communications* 9.1, p. 5423.

Obu, J, S Westermann, A Bartsch, N Berdnikov, HH Christiansen, A Dashtseren, R Delaloye, B Elberling, B Etzelmüller, A Kholodov, et al. (2019). "Northern Hemisphere permafrost map based on TTOP modelling for 2000–2016 at 1 km2 scale". In: *Earth-Science Reviews.*

Olefeldt, D, S Goswami, G Grosse, D Hayes, G Hugelius, P Kuhry, AD McGuire, VE Romanovsky, ABK Sannel, EAG Schuur, et al. (2016). "Circumpolar distribution and carbon storage of thermokarst landscapes". In: *Nature communications* 7.1, pp. 1–11.

Olson, DM, E Dinerstein, ED Wikramanayake, ND Burgess, GVN Powell, EC Underwood, JA D'amico, I Itoua, HE Strand, JC Morrison, et al. (2001). "Terrestrial Ecoregions of the World: A New Map of Life on EarthA new global map of terrestrial ecoregions provides an innovative tool for conserving biodiversity". In: *BioScience* 51.11, pp. 933–938.

Olthof, I, RH Fraser, and C Schmitt (2015). "Landsat-based mapping of thermokarst lake dynamics on the Tuktoyaktuk Coastal Plain, Northwest Territories, Canada since 1985". In: *Remote Sensing of Environment* 168, pp. 194–204.

Opel, T, JB Murton, S Wetterich, H Meyer, K Ashastina, F Günther, H Grotheer, G Mollenhauer, PP Danilov, V Boeskorov, GN Savvinov, and L Schirrmeister (2018). "Middle

and Late Pleistocene climate and continentality inferred from ice wedges at Batagay megaslump in the Northern Hemisphere's most continental region, Yana Highlands, interior Yakutia". In: *Climate of the Past Discussions* 2018, pp. 1–32. DOI: 10.5194/cp-2018-142.

Overduin, PP, T Schneider von Deimling, F Miesner, MN Grigoriev, C Ruppel, A Vasiliev, H Lantuit, B Juhls, and S Westermann (2019). "Submarine Permafrost Map in the Arctic Modeled Using 1-D Transient Heat Flux (SuPerMAP)". In: *Journal of Geophysical Research: Oceans* 124.6, pp. 3490–3507.

Park, H, Y Kim, and JS Kimball (2016). "Widespread permafrost vulnerability and soil active layer increases over the high northern latitudes inferred from satellite remote sensing and process model assessments". In: *Remote Sensing of Environment* 175, pp. 349–358.

Pastick, NJ, MT Jorgenson, SJ Goetz, BM Jones, BK Wylie, BJ Minsley, H Genet, JF Knight, DK Swanson, and JC Jorgenson (2019). "Spatiotemporal remote sensing of ecosystem change and causation across Alaska". In: *Global change biology* 25.3, pp. 1171–1189.

Pekel, J-F, A Cottam, N Gorelick, and AS Belward (2016). "High-resolution mapping of global surface water and its long-term changes". In: *Nature* 540.7633, pp. 418–422.

Planet Team (2017). "Planet application program interface: In space for life on Earth". In: *San Francisco, CA* 2017, p. 40.

Porter, C, P Morin, I Howat, M-J Noh, B Bates, K Peterman, S Keesey, M Schlenk, J Gardiner, K Tomko, M Willis, C Kelleher, M Cloutier, E Husby, S Foga, H Nakamura, M Platson, Jr. Wethington M, C Williamson, G Bauer, J Enos, G Arnold, W Kramer, P Becker, A Doshi, C D'Souza, P Cummens, F Laurier, and M Bojesen (2021). *ArcticDEM*. Harvard Dataverse. Accessed 08-February-2021.

Potapov, P, S Turubanova, and MC Hansen (2011). "Regional-scale boreal forest cover and change mapping using Landsat data composites for European Russia". In: *Remote Sensing of Environment* 115.2, pp. 548–561.

Quintero, N, O Viedma, IR Urbieta, and JM Moreno (2019). "Assessing landscape fire hazard by multitemporal automatic classification of Landsat Time Series using the Google Earth Engine in West-Central Spain". In: *Forests* 10.6, p. 518.

Ramage, JL, AM Irrgang, U Herzschuh, A Morgenstern, N Couture, and H Lantuit (2017). "Terrain controls on the occurrence of coastal retrogressive thaw slumps along the Yukon Coast, Canada". In: *Journal of Geophysical Research: Earth Surface* 122.9, pp. 1619–1634.

Romanovsky, VE, SL Smith, and HH Christiansen (2010). "Permafrost thermal state in the polar Northern Hemisphere during the international polar year 2007–2009: a synthesis". In: *Permafrost and Periglacial processes* 21.2, pp. 106–116.

Rouse, JW, RH Haas, JA Schell, DW Deering, et al. (1974). "Monitoring vegetation systems in the Great Plains with ERTS". In: *NASA special publication* 351.1974, p. 309.

Roy, D, Z Li, and H Zhang (2017). "Adjustment of Sentinel-2 multi-spectral instrument (MSI) Red-Edge band reflectance to Nadir BRDF adjusted reflectance (NBAR) and quantification of red-edge band BRDF effects". In: *Remote Sensing* 9.12, p. 1325.

Roy, DP, J Ju, K Kline, PL Scaramuzza, V Kovalskyy, M Hansen, TR Loveland, E Vermote, and C Zhang (2010). "Web-enabled Landsat Data (WELD): Landsat ETM+ composited mosaics of the conterminous United States". In: *Remote Sensing of Environment* 114.1, pp. 35–49.

Roy, DP, V Kovalskyy, HK Zhang, EF Vermote, L Yan, SS Kumar, and A Egorov (2016a). "Characterization of Landsat-7 to Landsat-8 reflective wavelength and normalized difference vegetation index continuity". In: *Remote sensing of Environment* 185, pp. 57–70.

Roy, DP, J Li, HK Zhang, L Yan, H Huang, and Z Li (2017). "Examination of Sentinel-2A multi-spectral instrument (MSI) reflectance anisotropy and the suitability of a general method to normalize MSI reflectance to nadir BRDF adjusted reflectance". In: *Remote Sensing of Environment* 199, pp. 25–38.

Roy, DP, HK Zhang, J Ju, JL Gomez-Dans, PE Lewis, CB Schaaf, Q Sun, J Li, H Huang, and V Kovalskyy (2016b). "A general method to normalize Landsat reflectance data to nadir BRDF adjusted reflectance". In: *Remote Sensing of Environment* 176, pp. 255–271.

Runge, A and G Grosse (2019). "Comparing Spectral Characteristics of Landsat-8 and Sentinel-2 Same-Day Data for Arctic-Boreal Regions". In: *Remote Sensing* 11.14, p. 1730.

— (2020). "Mosaicking Landsat and Sentinel-2 Data to Enhance LandTrendr Time Series Analysis in Northern High Latitude Permafrost Regions". In: *Remote Sensing* 12.15, p. 2471.

Rykhus, RP and Z Lu (2008). "InSAR detects possible thaw settlement in the Alaskan Arctic Coastal Plain". In: *Canadian Journal of Remote Sensing* 34.2, pp. 100–112.

Saunier, S, J Louis, V Debaecker, T Beaton, EG Cadau, V Boccia, and F Gascon (2019). "Sen2like, A Tool To Generate Sentinel-2 Harmonised Surface Reflectance Products-First Results with Landsat-8". In: *IGARSS 2019-2019 IEEE International Geoscience and Remote Sensing Symposium*. IEEE, pp. 5650–5653.

Sayre, R, D Karagulle, C Frye, T Boucher, NH Wolff, S Breyer, D Wright, M Martin, K Butler, K Van Graafeiland, et al. (2020). "An assessment of the representation of ecosystems in global protected areas using new maps of World Climate Regions and World Ecosystems". In: *Global Ecology and Conservation* 21, e00860.

Schmidt, GL, C Jenkerson, JG Masek, E Vermote, and F Gao (2013). "Landsat ecosystem disturbance adaptive processing system (LEDAPS) algorithm description". In:

Schneider, J, G Grosse, and D Wagner (2009). "Land cover classification of tundra environments in the Arctic Lena Delta based on Landsat 7 ETM+ data and its application for upscaling of methane emissions". In: *Remote Sensing of Environment* 113.2, pp. 380–391.

Schneider von Deimling, T, M Meinshausen, A Levermann, V Huber, K Frieler, DM Lawrence, and V Brovkin (2012). "Estimating the near-surface permafrost-carbon feedback on global warming". In: *Biogeosciences* 9, pp. 649–665.

Schuur, EAG and B Abbott (2011). "High risk of permafrost thaw". In: *Nature* 480.7375, pp. 32–33.

Schuur, EAG and MC Mack (2018). "Ecological response to permafrost thaw and consequences for local and global ecosystem services". In: *Annual Review of Ecology, Evolution, and Systematics* 49, pp. 279–301.

Schuur, EAG, AD McGuire, C Schädel, G Grosse, JW Harden, DJ Hayes, G Hugelius, CD Koven, P Kuhry, DM Lawrence, et al. (2015). "Climate change and the permafrost carbon feedback". In: *Nature* 520.7546, pp. 171–179.

Segal, RA, SV Kokelj, TC Lantz, KL Pierce, K Durkee, S Gervais, E Mahon, M Snijders, J Buysse, and S Schwarz (2016). "Mapping of terrain affected by retrogressive thaw slumping in Northwestern Canada". In: *Open Report* 23.

Séjourné, A, F Costard, A Fedorov, J Gargani, J Skorve, M Massé, and D Mège (2015). "Evolution of the banks of thermokarst lakes in Central Yakutia (Central Siberia) due to retrogressive thaw slump activity controlled by insolation". In: *Geomorphology* 241, pp. 31–40.

Serreze, MC and RG Barry (2011). "Processes and impacts of Arctic amplification: A research synthesis". In: *Global and planetary change* 77.1-2, pp. 85–96.

Shang, R and Z Zhu (2019). "Harmonizing Landsat 8 and Sentinel-2: A time-series-based reflectance adjustment approach". In: *Remote Sensing of Environment* 235, p. 111439.

Short, N, A-M LeBlanc, W Sladen, G Oldenborger, V Mathon-Dufour, and B Brisco (2014). "RADARSAT-2 D-InSAR for ground displacement in permafrost terrain, validation from Iqaluit Airport, Baffin Island, Canada". In: *Remote Sensing of Environment* 141, pp. 40–51.

Stolbovoi, V and I McCallum (2002). "Land Resources of Russia, International Institute for Applied Systems Analysis and the Russian Academy of Science". In:

Storey, J, M Choate, and K Lee (2014). "Landsat 8 Operational Land Imager on-orbit geometric calibration and performance". In: *Remote sensing* 6.11, pp. 11127–11152.

Storey, J, DP Roy, J Masek, F Gascon, J Dwyer, and M Choate (2016). "A note on the temporary misregistration of Landsat-8 Operational Land Imager (OLI) and Sentinel-

2 Multi Spectral Instrument (MSI) imagery". In: *Remote Sensing of Environment* 186, pp. 121–122.

Stow, DA, A Hope, D McGuire, D Verbyla, J Gamon, F Huemmrich, S Houston, C Racine, M Sturm, K Tape, et al. (2004). "Remote sensing of vegetation and land-cover change in Arctic Tundra Ecosystems". In: *Remote sensing of environment* 89.3, pp. 281–308.

Strauss, J, S Laboor, AN Fedorov, et al. (2016). "Database of ice-rich Yedoma permafrost (IRYP)". In: *PANGAEA*.

Strauss, J, L Schirrmeister, G Grosse, D Fortier, G Hugelius, C Knoblauch, V Romanovsky, C Schädel, T Schneider von Deimling, EAG Schuur, et al. (2017a). "Deep Yedoma permafrost: A synthesis of depositional characteristics and carbon vulnerability". In: *Earth-Science Reviews* 172, pp. 75–86.

Strauss, J, L Schirrmeister, G Grosse, D Fortier, G Hugelius, C Knoblauch, V Romanovsky, C Schädel, T Schneider von Deimling, EAG Schuur, D Shmelev, M Ulrich, and A Veremeeva (2017b). "Deep Yedoma permafrost: A synthesis of depositional characteristics and carbon vulnerability". In: *Earth-Science Reviews* 172, pp. 75–86. DOI: 10.1016/j.earscirev.2017.07.007.

Strauss, J, L Schirrmeister, G Grosse, S Wetterich, M Ulrich, U Herzschuh, and H-W Hubberten (2013). "The deep permafrost carbon pool of the Yedoma region in Siberia and Alaska". In: *Geophysical Research Letters* 40.23, pp. 6165–6170.

Strozzi, T, S Antonova, F Günther, E Mätzler, G Vieira, U Wegmüller, S Westermann, and A Bartsch (2018). "Sentinel-1 SAR interferometry for surface deformation monitoring in low-land permafrost areas". In: *Remote Sensing* 10.9, p. 1360.

Sudmanns, M, D Tiede, S Lang, H Bergstedt, G Trost, H Augustin, A Baraldi, and T Blaschke (2020). "Big Earth data: disruptive changes in Earth observation data management and analysis?" In: *International Journal of Digital Earth* 13.7, pp. 832–850.

Sulla-Menashe, D, RE Kennedy, Z Yang, J Braaten, ON Krankina, and MA Friedl (2014). "Detecting forest disturbance in the Pacific Northwest from MODIS time series using temporal segmentation". In: *Remote Sensing of Environment* 151, pp. 114–123.

Sulla-Menashe, D, CE Woodcock, and MA Friedl (2018). "Canadian boreal forest greening and browning trends: an analysis of biogeographic patterns and the relative roles of disturbance versus climate drivers". In: *Environmental Research Letters* 13.1, p. 014007.

Tatem, AJ, SJ Goetz, and SI Hay (2008). "Fifty years of earth observation satellites: Views from above have lead to countless advances on the ground in both scientific knowledge and daily life". In: *American Scientist* 96.5, p. 390.

Teillet, PM, JL Barker, BL Markham, RR Irish, G Fedosejevs, and JC Storey (2001). "Radiometric cross-calibration of the Landsat-7 ETM+ and Landsat-5 TM sensors based on tandem data sets". In: *Remote sensing of Environment* 78.1-2, pp. 39–54.

Teillet, PM, BL Markham, and Richard R Irish (2006). "Landsat cross-calibration based on near simultaneous imaging of common ground targets". In: *Remote sensing of environment* 102.3-4, pp. 264–270.

Torres, R, P Snoeij, D Geudtner, D Bibby, M Davidson, E Attema, P Potin, B Rommen, N Floury, M Brown, et al. (2012). "GMES Sentinel-1 mission". In: *Remote Sensing of Environment* 120, pp. 9–24.

Trofaier, AM, S Westermann, and A Bartsch (2017). "Progress in space-borne studies of permafrost for climate science: Towards a multi-ECV approach". In: *Remote Sensing of Environment* 203. Earth Observation of Essential Climate Variables, pp. 55–70. ISSN: 0034-4257. DOI: 10.1016/j.rse.2017.05.021.

Turetsky, MR, BW Abbott, MC Jones, K Walter Anthony, D Olefeldt, EAG Schuur, C Koven, AD McGuire, G Grosse, P Kuhry, et al. (2019). *Permafrost collapse is accelerating carbon release*.

Turetsky, MR, BW Abbott, MC Jones, K Walter Anthony, EAG Olefeldt Dand Schuur, G Grosse, P Kuhry, G Hugelius, C Koven, et al. (2020). "Carbon release through abrupt permafrost thaw". In: *Nature Geoscience* 13.2, pp. 138–143.

Ullmann, T, A Schmitt, A Roth, J Duffe, S Dech, H-W Hubberten, and R Baumhauer (2014). "Land cover characterization and classification of arctic tundra environments by means of polarized synthetic aperture X-and C-Band Radar (PolSAR) and Landsat 8 multispectral imagery—Richards Island, Canada". In: *Remote Sensing* 6.9, pp. 8565–8593.

Ulrich, M, H Matthes, L Schirrmeister, J Schütze, H Park, Y Iijima, and AN Fedorov (2017). "Differences in behavior and distribution of permafrost-related lakes in C entral Y akutia and their response to climatic drivers". In: *Water Resources Research* 53.2, pp. 1167–1188.

USGS (2015). "Landsat 8 (L8) data users handbook". In: *USGS* 1.

— (2016). "Landsat 8 (L8) data users handbook". In: *Department of the Interior US Geological Survey, LSDS-1574*.

— (2018). *Landsat Processing Details*. https://landsat.usgs.gov/landsat-processing-details. [Online; accessed 05-March-2018].

— (2020). *Landsat Collection 1 Level-1 Quality Assessment Band*. https://www.usgs.gov/land-resources/nli/landsat/landsat-collection-1-level-1-quality-assessment-band. [Online; accessed 24-March-2020].

USGS Product Guide (2018). "Landsat 4–7 Surface Reflectance LEDAPS Product". In: *Department of the Interior US Geological Survey: Reston, VG, USA*.

Van Everdingen, RO et al. (1998). *Multi-language glossary of permafrost and related ground-ice terms in chinese, english, french, german...* Arctic Inst. of North America University of Calgary.

Vasiliev, AA, DS Drozdov, AG Gravis, GV Malkova, KE Nyland, and DA Streletskiy (2020). "Permafrost degradation in the western Russian arctic". In: *Environmental Research Letters* 15.4, p. 045001.

Verbesselt, J, A Zeileis, and M Herold (2012). "Near real-time disturbance detection using satellite image time series". In: *Remote Sensing of Environment* 123, pp. 98–108.

Vuolo, F, M Żółtak, C Pipitone, L Zappa, H Wenng, M Immitzer, M Weiss, F Baret, and C Atzberger (2016). "Data service platform for Sentinel-2 surface reflectance and value-added products: System use and examples". In: *Remote Sensing* 8.11, p. 938.

Walter Anthony, K, T Schneider von Deimling, I Nitze, S Frolking, A Emond, R Daanen, P Anthony, P Lindgren, BM Jones, and G Grosse (2018). "21st-century modeled permafrost carbon emissions accelerated by abrupt thaw beneath lakes". In: *Nature communications* 9.1, p. 3262.

Wang, L, P Marzahn, M Bernier, and R Ludwig (2018). "Mapping permafrost landscape features using object-based image classification of multi-temporal SAR images". In: *ISPRS Journal of Photogrammetry and Remote Sensing* 141, pp. 10–29.

Wang, Q, GA Blackburn, AO Onojeghuo, J Dash, L Zhou, Y Zhang, and PM Atkinson (2017). "Fusion of Landsat 8 OLI and Sentinel-2 MSI data". In: *IEEE Transactions on Geoscience and Remote Sensing* 55.7, pp. 3885–3899.

Ward Jones, MK, WH Pollard, and BM Jones (2019). "Rapid initialization of retrogressive thaw slumps in the Canadian high Arctic and their response to climate and terrain factors". In: *Environmental Research Letters* 14.5, p. 055006.

Westermann, S, CR Duguay, G Grosse, and A Kääb (2015a). "13 Remote sensing of permafrost and frozen ground". In:

— (Jan. 2015b). *Remote Sensing of Permafrost and Frozen Ground*. Ed. by Marco Tedesco. Hoboken, NJ. DOI: 10.1002/9781118368909.ch13.

White, JC, MA Wulder, GW Hobart, JE Luther, T Hermosilla, P Griffiths, NC Coops, RJ Hall, P Hostert, A Dyk, et al. (2014). "Pixel-based image compositing for large-area dense time series applications and science". In: *Canadian Journal of Remote Sensing* 40.3, pp. 192–212.

Wilson, EH and SA Sader (2002). "Detection of forest harvest type using multiple dates of Landsat TM imagery". In: *Remote Sensing of Environment* 80.3, pp. 385–396.

Woo, M-K, DL Kane, SK Carey, and D Yang (2008). "Progress in permafrost hydrology in the new millennium". In: *Permafrost and Periglacial Processes* 19.2, pp. 237–254.

Woodcock, CE, R Allen, M Anderson, A Belward, R Bindschadler, W Cohen, F Gao, SN Goward, D Helder, E Helmer, et al. (2008). "Free access to Landsat imagery". In: *Science* 320.5879, pp. 1011–1011.

Wulder, MA, T Hilker, JC White, NC Coops, JG Masek, D Pflugmacher, and Y Crevier (2015). "Virtual constellations for global terrestrial monitoring". In: *Remote Sensing of Environment* 170, pp. 62–76.

Wulder, MA, TR Loveland, DP Roy, CJ Crawford, JG Masek, CE Woodcock, RG Allen, MC Anderson, AS Belward, WB Cohen, et al. (2019). "Current status of Landsat program, science, and applications". In: *Remote sensing of environment* 225, pp. 127–147.

Wulder, MA, JG Masek, WB Cohen, TR Loveland, and CE Woodcock (2012). "Opening the archive: How free data has enabled the science and monitoring promise of Landsat". In: *Remote Sensing of Environment* 122, pp. 2–10.

Xiong, J, PS Thenkabail, JC Tilton, MK Gumma, P Teluguntla, A Oliphant, RG Congalton, K Yadav, and N Gorelick (2017). "Nominal 30-m cropland extent map of continental Africa by integrating pixel-based and object-based algorithms using Sentinel-2 and Landsat-8 data on Google Earth Engine". In: *Remote Sensing* 9.10, p. 1065.

Yang, Y, PD Erskine, AM Lechner, D Mulligan, S Zhang, and Z Wang (2018). "Detecting the dynamics of vegetation disturbance and recovery in surface mining area via Landsat imagery and LandTrendr algorithm". In: *Journal of Cleaner Production* 178, pp. 353–362.

Zeng, H, G Jia, and H Epstein (2011). "Recent changes in phenology over the northern high latitudes detected from multi-satellite data". In: *Environmental Research Letters* 6.4, p. 045508.

Zhang, HK, DP Roy, L Yan, Z Li, H Huang, E Vermote, S Skakun, and J-C Roger (2018). "Characterization of Sentinel-2A and Landsat-8 top of atmosphere, surface, and nadir BRDF adjusted reflectance and NDVI differences". In: *Remote sensing of environment* 215, pp. 482–494.

Zhang, T, RG Barry, K Knowles, JA Heginbottom, and J Brown (2008). "Statistics and characteristics of permafrost and ground-ice distribution in the Northern Hemisphere". In: *Polar Geography* 31.1-2, pp. 47–68.

Zhu, Z (2017). "Change detection using landsat time series: A review of frequencies, preprocessing, algorithms, and applications". In: *ISPRS Journal of Photogrammetry and Remote Sensing* 130, pp. 370–384.

Zhu, Z, S Wang, and CE Woodcock (2015). "Improvement and expansion of the Fmask algorithm: Cloud, cloud shadow, and snow detection for Landsats 4–7, 8, and Sentinel 2 images". In: *Remote Sensing of Environment* 159, pp. 269–277.

Zhu, Z and CE Woodcock (2014). "Continuous change detection and classification of land cover using all available Landsat data". In: *Remote sensing of Environment* 144, pp. 152–171.

Zhu, Z, MA Wulder, DP Roy, CE Woodcock, MC Hansen, VC Radeloff, SP Healey, C Schaaf, P Hostert, P Strobl, et al. (2019). "Benefits of the free and open Landsat data policy". In: *Remote Sensing of Environment* 224, pp. 382–385.

****

Acknowledgements

I owe gratitude to many people for the completion of this thesis.

First and foremost, I would like to thank Guido Grosse. Allowing me to work on this dissertation and getting to know the world of permafrost has enriched my last 3 years immensely. I will take this with me, beyond AWI, Potsdam and science. I am very grateful for your support throughout the project time, supporting my ideas, constant scientific exchange, giving advice where needed, allowing me to explore different areas and always enabling me to come to an informed decision. Thank you.

Furthermore, I would also like to thank Ulrike Herzschuh and Birgit Heim for accompanying my project and always bringing new insights and possible research directions to my attention. I wish we could have had more in-person TAC meetings with coffee and cake.

Birgit, thank you also for guiding me through my first Arctic expedition. I think back to those days on Samoylov with fond memories. Also, thank you Matthias (Fuchs), for being such a great expedition buddy, introducing me to the SIPRE drill and helping me figure out endless error messages from the spectrometer.

When I joined AWI, I was warmly welcomed into the former PETA-Carb team. The lovely group dynamic, daily lunch meetings and coffee breaks made me feel instantly welcome and part of the group. I love that everyone always brings cake. Thank you to Josefine Lenz, Jens Strauss, Matthias Fuchs, Anne Morgenstern, Juliane Wolter, Torben Windirsch and Frank Günther. This warm welcome was extended beyond the PETA-Carb team. Thank you to Konstantin Klein, Anna Irrgang, Michael Fritz, Hugues Lantuit, Paul Overduin and Lutz Schirrmeister for all the lunch and coffee chats. Beyond this, AWI has become a true enrichment for me. Thanks to Sonya Antonova, Niko Bornemann, Bennet Juhls and Antje Eulenberg for all the lovely chats, it is always great to see a friendly face.

Ingmar Nitze and Sebastian Laboor, you were my first office mates and are now part of the hallway-crew. Thank you for creating such a welcoming atmosphere, providing endless amounts of tea, sharing sweets and always having an open ear. And yes, there was also lots of scientific exchange and technical help, I highly appreciated it.

Furthermore, I would like to thank the remaining floor-crew. Rebecca Rolph, thanks for all the Cafe Freundlich breaks, it definitely helped my caffeine addiction. Lona van Delden and Clair Treat, I am happy you joined our hallway, bringing laughter, good conversation and more recently helping out with the plants.

On a more personal note, I would like to express my biggest gratitude to Loeka Jongejans, Lydia Stolpmann, Tabea Rettelbach and Michael Angelopolous. I feel our friendship goes beyond a work relationship and being Doctoral Researchers together. You have all helped

making me feel at home at AWI and in Potsdam. Lydia, thank you for all the chats, on work and non-work topics, for all the crafting (birthdays or hats) and being there until the end. Loeka, you have accompanied my Doctoral Research time the most, with attending PhD days and participating in the JTP program together. It has been a treat doing all of this together. Thank you for being a constant pillar, thank you for being a friend. Tabea, you have made long office hours less frustrating and made our office a safe place for conversation, laughter and plants. I wish we could have spent more time together in the office but I am grateful we have kept a couple of office traditions. Thanks for the plants and all the cake. Mike, you introduced me to Rückholz and Wednesday night meet-ups, I hope there will be more soon. Thank you for being an absolute supporter and cheerleader, constantly reminding me that I can do anything. I am very grateful for this.

Thank you to Claudia Hanfland and Claudia Sprengel for such a good job with Polmar. Thank you for all the great scientific and soft skill courses, as well as the constant guidance of us Doctoral Researchers. The Polmar program is an absolute asset to the DR experience at AWI!

My dissertation was funded by a couple of projects and funding agencies. Thank you to the European Research Council (PETA-CARB), to Bundesministerium für Bildung und Forschung (KoPf) and the European Space Agency (ESA GlobPermafrost). Furthermore, I was able to attend a number of conferences and summer schools because of funding I received from Geo.X, European Commission, and Deutscher Akademischer Austausch Dienst.

Liebe GS-WG, danke für die Aufnahme und dafür, dass Potsdam so schnell zu meinem neuen Zuhause wurde. Ohne euch wäre Potsdam nur halb so schön! Mein herzlichstes Dankeschön für die Unterstützung in einer meiner stressigsten Zeit. Danke für Putzen, Kuchen, Kochen und Bier, liebe Klara, Karo und Lascha! Auch noch ein Dank an Aglaja und Stefan, für 2 wunderschöne Jahre mit Tatort, Radtouren, Spieleabende und mehr.

Ob nah oder fern, ich konnte immer auf die Unterstützung meiner Freunde zählen. Auch wenn häufig nur ein Telefonat möglich war, hatte ich zu jeder Zeit immer mehrere Anlaufstellen. Danke für die Grußkarten, Nachrichten, Aufmunterungen und Anrufe zu jeder Zeit. Ich freue mich euch alle bald wiederzusehen. Besonders bedanken möchte ich mich bei Doro und Lena. Ihr seid schon lange meine Wegbegleiter und Teil meiner erweiterten Familie. Danke für eure Aufmunterungen, Besuche, Ratschläge und einfach das ihr da seid. Danke für eure Freundschaft.

Als letztes möchte ich mich bei meiner Familie bedanken. Mama und Papa, ihr habt mich von klein auf unterstützt und immer meinen Weg gehen lassen, egal ob es mich in die weite Ferne oder in die nahe Ferne verschlagen hat, egal ob ich studieren oder eine Auszeit nehmen wollte. Mein Dank hierfür ist unermesslich und es ist schön immer wieder nach Hause kommen zu können. Wenn auch manchmal ein eher stiller Begleiter, ist mein Bruder Niklas immer ein stetiger Begleiter. Ich möchte dich nicht missen und auch nicht deine Aufmunterungsfloskeln, an die du selbst nicht glaubst.

Eidesstaatliche Erklärung

Hiermit versichere ich, dass ich die vorliegende Arbeit selbstständig verfasst und keine anderen als die angegebenen Quellen und Hilfsmittel verwendet habe. Ich habe diese kumulative Dissertation am Alfred-Wegener-Institut Helmholtz Zent- rum für Polar und Meeresforschung in Potsdam erarbeitet und in englischer Sprache angefertigt. Diese Dissertation wird erstmalig und ausschließlich an der Universität Potsdam eingereicht. Die dem Promotionsverfahren zugrundeliegende Promotionsordnung vom 18.09.2013 ist mir bekannt.

Potsdam, den 18.03.2021 Alexandra Runge

****